Models of Protein Organisation

Matthew W. Cotton

University College
University of Oxford

A thesis submitted for the degree of
Doctor of Philosophy

Trinity 2024

Abstract

The organisation of atoms and small molecules gives the familiar structures of gases, solids, and other states of matter. The organisation of proteins drives the essential processes of life. This thesis explores three different molecular mechanisms that act to organise proteins by constructing minimal models that can predict or explain phenomena of protein organisation. Firstly, we study the effective interactions that can arise between proteins that catalyse reactions, called enzymes. We develop a thermodynamically consistent model describing the dynamics of a multicomponent mixture where one enzyme component catalyses a reaction between other components. We find that the catalytic activity alone can induce phase separation for sufficiently active systems and large enzymes, without any equilibrium interactions between components. We label this catalysis-induced phase separation and show that it generates a feedback mechanism that can act to autoregulate the enzymatic activity, giving this simple mechanism complex design opportunities in the natural world or engineered systems. Secondly, we explore how proteins that induce curvature in membranes can interact via membrane mediated elastic forces. We derive an interaction energy for many, well-separated, small inclusions in a flat membrane with tension and find that in this limit the interaction energy between many inclusions is the sum of the two-body interactions. This interaction fundamentally changes when the curvature-inducing inclusions are not radially symmetric by the emergence of a well defined equilibrium separation. However, in addition to altering the direction of the force, the anisotropy affects the formation of aggregates of many inclusions, as inclusions experience a geometric frustration that can oppose the equilibrium of the pairwise interaction. As such, the equilibrium arrangements of groups of inclusions are rings, lines and polygonal lattices. Thirdly, we extend existing models of aggregating proteins in living systems, by including a finite rate for aggregate removal mechanisms. The accumulation of protein aggregates is associated with many diseases and a bounded clearance rate can explain observed phenomena such as seeding, recovery of mice following monomer reducing therapies, and the disease incidence. This model is the first theoretical framework to capture all of these behaviours and this key behaviour is robust to changes in exact molecular kinetics. This framework can be used to understand the role of current therapies and for the rational design of future therapies.

Models of Protein Organisation

Matthew W. Cotton

University College

University of Oxford

A thesis submitted for the degree of

Doctor of Philosophy

Trinity 2024

Acknowledgements

The research presented in this thesis would not have been possible without the guidance and expertise of an exceptional group of scientists and mathematicians. I am deeply grateful to Prof. Alain Goriely, Prof. Ramin Golestanian, Prof. Jon Chapman, Dr. Jaime Agudo-Canalejo, and Dr. Georg Meisl for their mentorship and support. I am particularly appreciative of your willingness to entertain my many questions, and I am always in awe of the clarity and insight in your answers.

Beyond my supervisory team, I have learnt so much from my peers, postdocs, and permanent employees within the Oxford Centre for Industrial and Applied Mathematics and the Department of Living Matter Physics at MPIDS. I am thankful for the time you gave me discussing various aspects of your work, my work, and why my ideas won't work.

I am grateful to friends in Oxford, particularly Jorin and Samvida for your vision. I gratefully acknowledge financial support from the Oxford Interdisciplinary Bioscience DTP and University College, which has supported me during the pursuit of this degree and enabled my travel to conferences and meetings.

I am forever indebted to my family for your unwavering support and the vanilla slices.

Abstract

The organisation of atoms and small molecules gives the familiar structures of gases, solids, and other states of matter. The organisation of proteins drives the essential processes of life. This thesis explores three different molecular mechanisms that act to organise proteins by constructing minimal models that can predict or explain phenomena of protein organisation. Firstly, we study the effective interactions that can arise between proteins that catalyse reactions, called enzymes. We develop a thermodynamically consistent model describing the dynamics of a multicomponent mixture where one enzyme component catalyses a reaction between other components. We find that the catalytic activity alone can induce phase separation for sufficiently active systems and large enzymes, without any equilibrium interactions between components. We label this catalysis-induced phase separation and show that it generates a feedback mechanism that can act to autoregulate the enzymatic activity, giving this simple mechanism complex design opportunities in the natural world or engineered systems. Secondly, we explore how proteins that induce curvature in membranes can interact via membrane mediated elastic forces. We derive an interaction energy for many, well-separated, small inclusions in a flat membrane with tension and find that in this limit the interaction energy between many inclusions is the sum of the two-body interactions. This interaction fundamentally changes when the curvature-inducing inclusions are not radially symmetric by the emergence of a well defined equilibrium separation. However, in addition to altering the direction of the force, the anisotropy affects the formation of aggregates of many inclusions, as inclusions experience a geometric frustration that can oppose the equilibrium of the pairwise interaction. As such, the equilibrium arrangements of groups of inclusions are rings, lines and polygonal lattices. Thirdly, we extend existing models of aggregating proteins in living systems, by including a finite rate for aggregate removal mechanisms. The accumulation of protein aggregates is associated with many diseases and a bounded clearance rate can explain observed phenomena such as seeding, recovery of mice following monomer reducing therapies, and the disease incidence. This model is the first theoretical framework to capture all of these behaviours and this key behaviour is robust to changes in exact molecular kinetics. This framework can be used to understand the role of current therapies and for the rational design of future therapies.

Contents

1 Introduction **1**

1.1 What is a protein? . . . 2

1.1.1 The Hierarchy of Protein Interactions . . . 3

1.2 Proteins in Health and Disease . . . 4

1.3 Engineering Proteins . . . 5

1.4 Thesis Scope and Structure . . . 6

2 Active Phase Separation of Dense Mixtures **8**

2.1 Introduction . . . 9

2.2 Equilibrium Phase Separation . . . 10

2.2.1 Thermodynamics of Fluid Mixtures . . . 10

2.2.2 Regular Solution Model . . . 13

2.3 Dynamics of Multi-Component Mixtures . . . 18

2.3.1 Conserved Dynamics . . . 18

2.3.2 Non-Conserved Dynamics . . . 20

2.4 Minimal Model of an Active Mixture . . . 22

2.5 Catalysis-Induced Phase Separation . . . 24

2.5.1 Stability of the Homogeneous Steady State . . . 24

2.5.2 Numerical Simulation . . . 27

2.5.3 Effective Free Energy and Binodal . . . 29

2.5.4 Stability of a Four-Component System . . . 32

2.5.5 Enzymatic Autoregulation . . . 34

2.6 Discussion . . . 35

3 Membrane Mediated Elastic Interactions **39**

3.1 Introduction . . . 40

3.2 Background . . . 43

3.2.1 Helfrich Hamiltonian . . . 43

3.2.2 Monge Parameterisation . . . 45

3.3 One Inclusion in an Elastic Membrane . . . 47

3.3.1 Monopole and Quadrupole Modes . . . 49

3.3.2 Dipole Mode . . . 51

3.4 Multiple Inclusions in an Elastic Membrane . . . 53
3.4.1 Calculating the Membrane Shape . . . 54
3.4.2 Matching . . . 56
3.4.3 Membrane Interaction Energy . . . 62
3.4.4 Identical Inclusions . . . 63
3.4.5 Features of the Two-Body Interaction Potential . . . 63
3.5 Systems of Interacting Inclusions . . . 65
3.6 Rings, Lines and Lattices . . . 66
3.6.1 Rings . . . 66
3.6.2 Lines . . . 71
3.6.3 General Configurations . . . 75
3.6.4 Configurations of Multiple Inclusions . . . 79
3.7 Multi-Scale Model for Configurations . . . 81
3.8 Biological Regimes . . . 86
3.9 Discussion . . . 88

4 Protein Aggregation in Disease **91**
4.1 Introduction . . . 92
4.2 Background . . . 92
4.2.1 Aggregating Neurodegenerative Disease . . . 93
4.3 Aggregation Kinetics in vitro . . . 93
4.3.1 Failure to Describe Features of Disease . . . 98
4.4 Aggregation Kinetics in vivo . . . 101
4.4.1 Unbounded Clearance . . . 102
4.4.2 Bounded Clearance . . . 106
4.4.3 Reduced Models of in vivo Aggregation . . . 109
4.5 Generalising the Dynamics . . . 113
4.5.1 Generalised Models of Clearance . . . 113
4.5.2 Exponential Growth is Unphysical . . . 115
4.5.3 Non-Conserved Monomer . . . 117
4.5.4 Length Dependent Seeding . . . 118
4.5.5 Length Dependent Clearance . . . 119
4.6 Transitions to Disease and Therapeutic Scenarios . . . 121
4.6.1 Ageing reduces Clearance . . . 122
4.6.2 Explaining Genetic Susceptibility . . . 123
4.6.3 Rational Therapeutic Design . . . 124
4.7 Summary and Conclusions . . . 127

5 Concluding Remarks **128**
5.1 The Investigated Protein Organisation 129
5.1.1 Active Phase Separation of Dense Mixtures 129
5.1.2 Membrane Mediated Elastic Interactions 130
5.1.3 Protein Aggregation in Disease 131
5.2 The Interplay of Protein Organisation 132
5.2.1 Membranes and Condensates in Aggregation 132
5.2.2 Phase-Separated Curved Domains 134
5.3 The Importance of Protein Organisation 135

References **137**

1 Introduction

Contents

1.1 What is a protein? 2
1.1.1 The Hierarchy of Protein Interactions 3
1.2 Proteins in Health and Disease 4
1.3 Engineering Proteins 5
1.4 Thesis Scope and Structure 6

Proteins are the molecular building blocks of all living systems. The emergence of life from these fundamental components depends on how proteins are organised in both space and time, and across a multitude of scales. Understanding the forces governing this organisation not only elucidates how matter comes alive, but knowing how and why these processes go wrong can help us to design effective therapeutics for disease or even hijack and engineer these processes to harness the power of proteins.

In this thesis I explore three different mechanisms for protein organisation. I will develop mathematical models that capture the main features of physical interactions between proteins and study the structure and consequences of these equations, comparing with experimental studies where relevant. Each mechanism has broadly been studied before but I will detail how to capture key features of the interaction that can lead to a fundamentally different route for protein organisation.

1.1 What is a protein?

Biochemically, proteins are a class of molecules that are long unbranched chains of individual units, called amino acids [1]. Each amino acid has the same basic structure that polymerises to form a protein backbone held together by peptide bonds, a type of covalent bond. The distinct amino acids have distinct side chains that are attached to the polymerising unit and it is this side chain that defines the different amino acids. The primary structure of a protein is the specific sequence of amino acids that makes up each protein and this recipe is stored in the genetic information of every organism [2]. Various cellular machinery read this genetic information and manufacture polypeptide chains with the coded sequence of amino acids. An array of non-covalent bonds, such as hydrogen bonds, electrostatic attractions and van der Waals forces, then *fold* the chain to determine the exact location of each atom in 3D space, although this can be disrupted by thermal fluctuations. The protein's shape is called its ternary structure and is crucial in determining many of the protein's functions. For example, enzymes are proteins that catalyse biological reactions by binding to a molecule to form a complex and this binding requires that the enzyme and molecule have exactly complimentary shapes, like a lock and key [3].

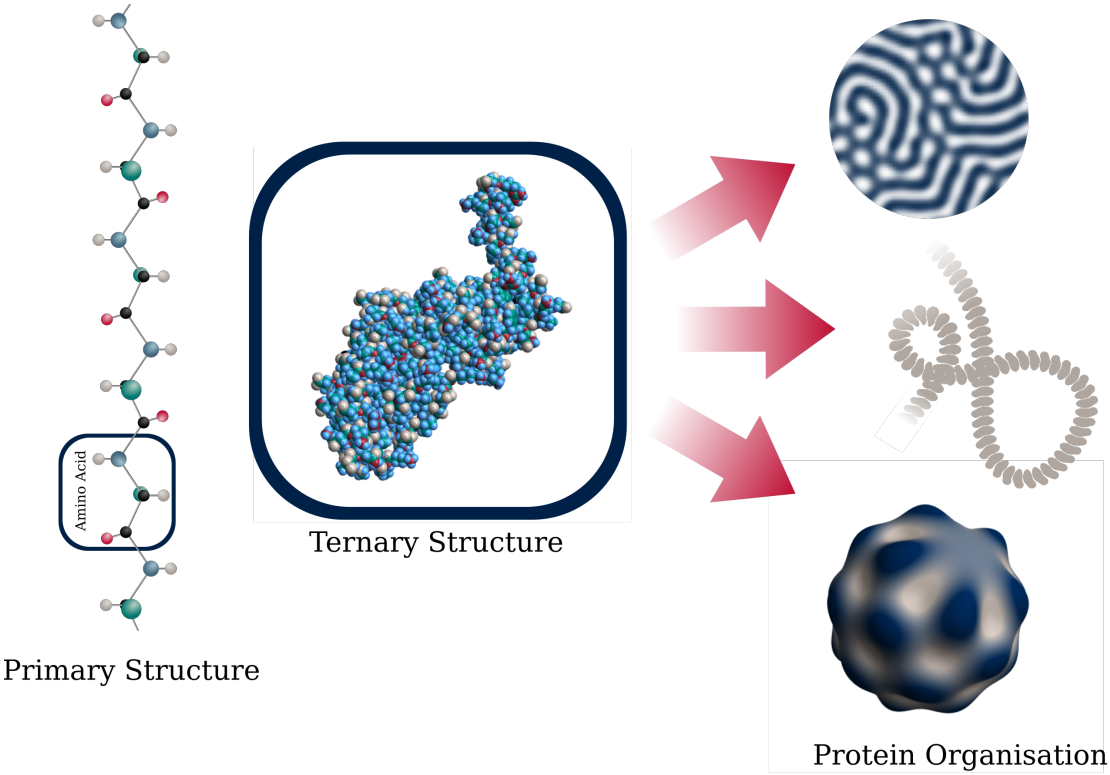

Figure 1.1: The hierarchy of protein structure. Amino acids make proteins that then interact to form structures and patterns. The graphics show examples of protein organisation inspired by (top to bottom) reaction diffusion systems [4], fibrils and filaments [5], and curvature induced membrane patterning [6]. The structure of the protein shown is generated from coordinates in the protein database, structure 1EZB [7].

1.1.1 The Hierarchy of Protein Interactions

During my research for this thesis, the development and release of AlphaFold changed the conversation around protein structure. AlphaFold is a neural network designed to solve the problem of protein folding: learning the map from amino acid sequence (primary structure) to an atomistic description of the 3D shape (ternary structure). In 2021, AlphaFold became the first computational method to achieve accuracy on par with experimental structure determination [8]. Since then, it has become an invaluable tool in the arsenal of scientists trying to understand a variety of biological processes. Structure prediction can help to understand why, for example, a genetic modification might stop a molecule binding to a protein, elucidating unknown binding mechanisms, and engineering mutations to enhance binding affinity and catalytic rates. This model also represented a paradigm shift

from mechanistic physics informed modelling to solve the folding problem to a deep learning approach. This was possible due to the extensive database of experimentally determined structures in the Protein Data Bank and the abundance of sequencing data from advanced sequencing technologies.

In this thesis, I have explored an alternative approach to protein engineering and I have explored interactions at a different scale. Rather than considering changing the individual protein structure, I have studied mechanisms by which proteins can conspire to form structures that affect function as outlined in Figure 1.1. This collective organisation often relates to protein structure, however, my research demonstrates that the protein environment also plays a crucial role in tuning emergent phenomena. Varying monomer concentration in systems of aggregating proteins, adding solvent to a dense active mixture, or increasing the tension in a membrane filled with proteins are all examples of the rich parameter space that can be explored when we begin to understand larger scale protein dynamics.

1.2 Proteins in Health and Disease

Proteins are the work horses of cellular and subcellular machinery. If anything happens on the subcelluar scale, there is normally a protein making it happen. Enzymes are proteins that catalyse reactions, making processes feasible on relevant molecular timescales [2]. Kinesin and other motor proteins drag cargo and provide essential active transport functionality [9] alongside proteins such as ion channels that can span physical barriers within the cell and allow passive transport to occur [3]. This arsenal of transport processes determines how the distribution of biomolecules can be kept from equilibrium, or how efficiently a system can relax to some steady state, helping to control cell signalling and the flow of information.

Another function of proteins is as building blocks for subcellular structures, such as microtubules, or viral capsids [10]. In recent years, liquid-liquid phase separation has also emerged as a key feature of intracellular organisation [11], [12]. These are liquid droplets that have a different composition to the surrounding environment, typically with an enriched protein concentration. The droplets, or condensates,

can act as reaction crucibles, can promote signalling or sequester molecules in the cell and prevent off target effects [11]. The formation and maturation of liquid condensates are governed by protein interactions.

The importance of proteins in so many biological processes means that they can have devastating effects when they fail to function correctly. For example, cystic fibrosis is a disease caused by the misfolding of a transmembrane protein and its subsequent inability to function [13]. In addition to this lack of function mechanism, the gain of toxic function can also cause disease [14]. A whole class of diseases stems from proteins interacting and forming toxic aggregates [15], [16]. Understanding how essential, functional protein-protein interactions may go awry, or how toxic interactions emerge, is essential to understanding and preventing many human diseases.

1.3 Engineering Proteins

Alongside essential roles in all of cellular biology, proteins serve as the foundation for many engineered biomaterials. One particular example is keratin, a naturally occurring fibrous protein found in hair, nails, feathers, and horns [17]. Keratin-based biomaterials have a wide range of biomedical applications, including wound dressings, tissue engineering scaffolds, and drug delivery systems [18]. The protein forms long, cross-linked filaments that can be either hard or soft, depending on the sulphur content of the material. The sulphur, or in some cases other proteins, creates cross-links between keratin filaments, and these interactions determine the strength and structure of the resulting material, giving rise to materials such as fibres, films, sponges, and gels. The utility of keratin-based biomaterials lies in their ability to self-assemble into 3D structures, a process entirely governed by protein interactions[18]

Multi-component engineered systems also include proteins as key components. Synthetic membranes that act as controllable barriers, rely on protein interactions with the membranes for effective embedding and manufacture [19]. Such membranes can support the development of nanoreactors, artificial organelles or chemically active surfaces. Proteins can also interact with membranes to transport cargo

allowing for spatial organisation with applications to creating synthetic cells and mimicking lifelike function [20]. The whole field of synthetic biology is built around controlling and programming cell-like behaviour and proteins are a necessary tool in this pursuit [21].

1.4 Thesis Scope and Structure

Each chapter in this thesis explores a different physical mechanism to drive protein organisation. I will introduce the background necessary to understand each mechanism and highlight specific aspects of these protein-protein interactions that have been previously understudied. Using a range of techniques, I will build mathematical models that incorporate important features of the interactions and study the effects on the resulting protein organisation, ultimately exploring how this can affect function or pathology. Below I provide a brief summary of each system studied:

1. **Catalysis-Induced Phase Separation** Liquid-liquid phase separation can form droplets in mixtures of proteins and other components. The formation of these regions can be driven by equilibrium interactions between the components, but in this chapter we demonstrate that modelling chemically active components can give rise to fundamentally new phenomena. An enzymatic component can drive liquid-liquid phase separation without the equilibrium interactions and this can subsequently affect overall reaction rates in the system.

2. **Anisotropic Membrane Mediated Interactions** Proteins that bind to and bend biological membranes can generate elastic forces that act on other proteins in the membrane. These forces can generate structures and remodel the membrane. However, many of the curvature-inducing inclusions that bind in this way break radial symmetry and this changes their interactions, introducing an equilibrium separation and forming lattices of inclusions that can be controlled via the protein curvature or membrane stiffness.

3. **Bounded Clearance in Neurodegenerative Disease** A plethora of neurodegenerative diseases are associated with aggregated proteins that are produced and removed in the brain. However, existing models ignore physical constraints that limit and bound the rates at which these aggregated proteins can be removed. Including this key constraint when modelling the aggregation kinetics can present a fundamentally new mechanism for the onset of disease which is consistent with recent experiments and can help design rational therapeutics.

2

Active Phase Separation of Dense Mixtures

Contents

2.1 Introduction 9
2.2 Equilibrium Phase Separation 10
2.2.1 Thermodynamics of Fluid Mixtures 10
2.2.2 Regular Solution Model 13
2.3 Dynamics of Multi-Component Mixtures 18
2.3.1 Conserved Dynamics 18
2.3.2 Non-Conserved Dynamics 20
2.4 Minimal Model of an Active Mixture 22
2.5 Catalysis-Induced Phase Separation 24
2.5.1 Stability of the Homogeneous Steady State 24
2.5.2 Numerical Simulation 27
2.5.3 Effective Free Energy and Binodal 29
2.5.4 Stability of a Four-Component System 32
2.5.5 Enzymatic Autoregulation 34
2.6 Discussion 35

2.1 Introduction

At the cellular and sub-cellular level, biomolecules can be spatially organised by membrane bound compartments such as organelles. These distinct regions of the cell have distinct biophysical properties and distinct chemical compositions that are specialised to carry out specific functions or to keep molecules from interacting that could disrupt healthy cellular function [2]. Membranes are crucial to separating these regions of the cell, but recently membraneless organelles formed by liquid-liquid phase separation are emerging as alternative structures to spatially organise living matter [22]. Here, liquid droplets form within the cell that have different molecular composition to the surrounding cytoplasm, similar to the formation of droplets of oil in water.

The theory of liquid-liquid phase separation has been well described in polymer systems [23] and, in living cells, the formation of these droplets is driven by weak transient interactions between multivalent proteins - the polymers of life [11]. However, a key recent development in the field has been to add non-equilibrium effects into descriptions of phase transitions, including actively propelled particles [24], phoretic transport effects [25] and changes in chemical composition [26], [27]. Including the effects of chemical reactions into these models is necessary to describe the non-equilibrium environment in vivo. In fact, liquid-liquid phase separation is now recognised as a common tool in the regulation of enzyme activity in cells [28]. This can occur in a few ways, for example by directly affecting reaction kinetics [12] or by supporting the formation of metabolons, when multiple enzymes physically associate and form complexes that can connect sequential steps of a reaction pathway [29]. In order to capture the effects of the enzymatic activity and changes in composition, this chapter develops a minimal model to describe an active mixture containing an enzyme component. We study the stability of a spatially homogeneous mixtures and explain how the activity can lead to the formation of phase-separated regions [30].

2.2 Equilibrium Phase Separation

2.2.1 Thermodynamics of Fluid Mixtures

We begin by reviewing equilibrium phase separation. A good example to explore the theory of phase separating mixtures is to study a fluid made up of two components, say, component A and component B. To make this mixture, we mix N_A molecules of component A and N_B molecules of component B to give a mixture of total volume $V = v_A N_A + v_B N_B$, where v_i is the specific volume of the component, the *size* of each molecule. The volume fraction of a component, ϕ_i, in some region of volume, v, is defined to be $\phi_i = v_i N_i / v$ and for the two component mixture $\phi_A + \phi_B = 1$. To simplify the notation, let $\phi_A = \phi$ and $\phi_B = 1 - \phi$, and the volume fraction ϕ now describes the proportion of the fluid volume that is component A. For an incompressible fluid, the total volume is constant and the relevant free energy is the Helmholtz free energy, $F(N_A, N_B, T)$ where T is the temperature of the fluid. The Helmholtz free energy is an extensive quantity and so for a homogeneous mixture $F(N_A, N_B, T) = V f(\phi, T)$ where $f(\phi, T)$ is the free energy density and this free energy density determines the phase behaviour of the mixture. If a system phase separates into two coexisting phases, then the free energy of two phase system is $V^{\mathrm{I}} f(\phi^{\mathrm{I}}, T) + V^{\mathrm{II}} f(\phi^{\mathrm{II}}, T)$ where the two phases are labelled I and II and the total volume of the system is conserved $V = V^{\mathrm{I}} + V^{\mathrm{II}}$. It is necessary for the two phase free energy to be lower than the free energy of an equivalent homogeneous system in order for the system to phase separate [1].

In addition to lowering the free energy of the system, any phase separating regions of a mixture must also be in mechanical and chemical equilibrium, otherwise they would exchange components or volume to reach two equilibrated phases. Chemical equilibrium is achieved when the chemical potential, μ, of each component in each phase is constant and so moving a particle across the phase boundary will not change the free energy, $\mu_i^{\mathrm{I}} = \mu_i^{\mathrm{II}}$. The chemical potential for component i is

$$\mu_i = \left(\frac{\partial F}{\partial N_i} \right)_{V,T} = v_i \left(\frac{\partial f}{\partial \phi_i} \right)_T . \tag{2.1}$$

The mechanical equilibrium is achieved when the osmotic pressure, Π between the two phases is equal, $\Pi^{\mathrm{I}} = \Pi^{\mathrm{II}}$, where the osmotic pressure is given by

$$\Pi(\phi) = -\left(\frac{\partial F}{\partial V}\right)_{T,N_A} = -f + \phi\left(\frac{\partial f}{\partial \phi}\right)_T . \tag{2.2}$$

since $\phi = N_A v_a/V$ and so $\frac{\partial \phi}{\partial V} = -\phi/V$ [31]. These conditions have a convenient graphical interpretation. The equation for a tangent to the curve $y = f(\phi)$ at $\phi = \tilde{\phi}$ can be written as $y = m\phi + c$. Combining (2.1) and (2.2) give $y = v_A^{-1}\mu_A(\tilde{\phi})\phi - \Pi(\tilde{\phi})$ and as these thermodynamic quantities must be the same for two coexisting phases, we find that two phases can only coexist at values of ϕ such that $y = f(\phi)$ has a *common tangent*! Figure 2.1 highlights the graphical interpretation of these conditions, where plotting $f(\phi)$ can illuminate the phase behaviour of a mixture. A well mixed homogeneous system prepared with volume fraction ϕ^*, will therefore be stable as two phase-separated with regions volume fraction ϕ^{I} and ϕ^{II} ($\phi^{\mathrm{I}} < \phi^{\mathrm{II}}$) given that $\phi^{\mathrm{I}} < \phi^* < \phi^{\mathrm{II}}$ [32]. The conservation of N_A requires $V\phi^* = V^{\mathrm{I}}\phi^{\mathrm{I}} + V^{\mathrm{II}}\phi^{\mathrm{II}}$ and volume conservation gives $V = V^{\mathrm{I}} + V^{\mathrm{II}}$ which determines the volumes of each phase

$$V^{\mathrm{I}} = \frac{\phi^{\mathrm{II}} - \phi^*}{\phi^{\mathrm{II}} - \phi^{\mathrm{I}}} V \quad \text{and} \quad V^{\mathrm{II}} = \frac{\phi^* - \phi^{\mathrm{I}}}{\phi^{\mathrm{II}} - \phi^{\mathrm{I}}} V \tag{2.3}$$

which is known as the lever rule.

Often, the shape of the free energy density can be controlled by varying some external parameter, such as temperature. As the temperature is changed, the volume fractions of the two coexisting phases also change. Plotting these values against the temperature generates the so-called binodal curve, where the two branches meet at some critical value. This is shown graphically in Figure 2.2.

Another important feature of a free energy landscape is the spinodal curve. This curve defines the region where the free energy is not convex, $\partial^2 f/\partial\phi^2 < 0$. As such, a mixture in the spinodal region is unstable to small perturbations and will decay into the phase-separated state spontaneously. There also exists a region in between the spinodal and binodal curves that is metastable: the free energy would be lower in a phase-separated system, but there is an energy barrier preventing the system from transitioning to this state. This energy barrier is a nucleation barrier,

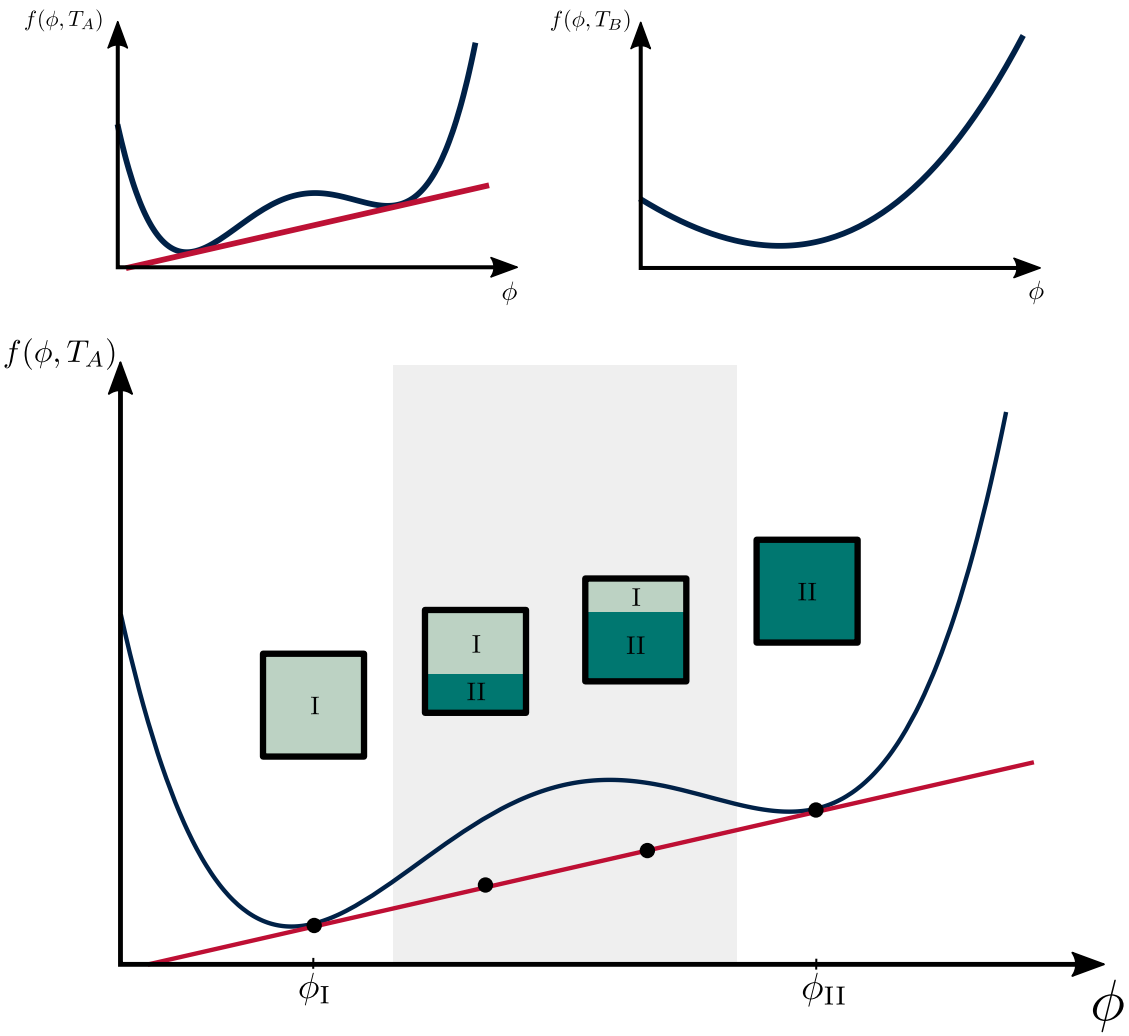

Figure 2.1: Schematic of equilibrium phase separation, showing a system that exhibits coexisting phases at some temperature T_A, but not at another temperature T_B which has a convex free energy. In the lower plot examples of the distribution of the two phases in a system are shown with two examples of a phase-separated system.

where phase-separated regions will only grow when they are above a critical size. A large enough perturbation, for example from temperature fluctuations, could overcome this nucleation barrier, but often in real systems imperfections, or external structures, can act as nucleation sites and cause the transition. This region is also shown in figures 2.1 and 2.2, where the shaded region is the unstable spinodal region and the boundary defines the spinodal curve [1].

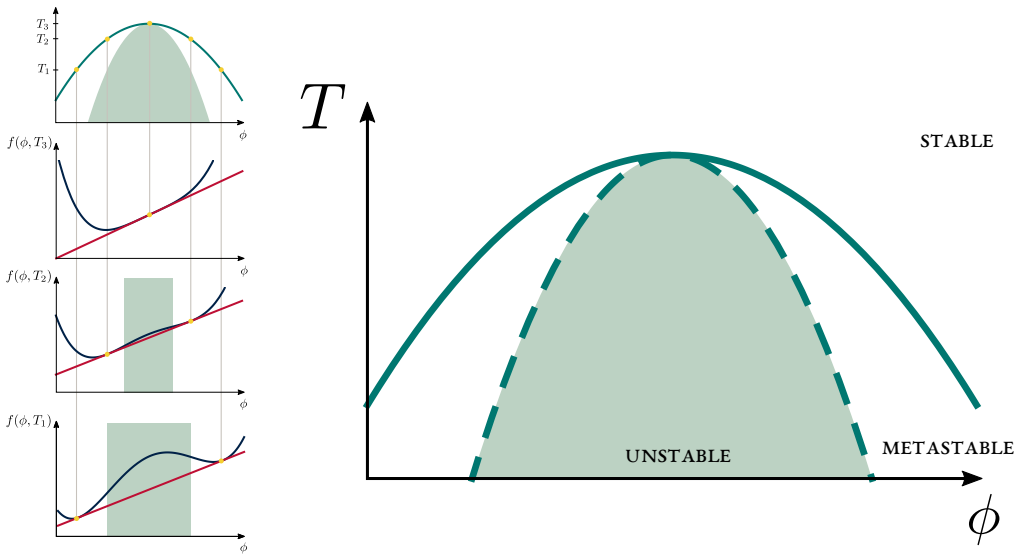

Figure 2.2: Graphical explanation of how the phase diagram for an equilibrium system is calculated. The solid, binodal line is the boundary between the stable and metastable state and the dashed spinodal line is the boundary between the unstable and metastable states. The two lines meet at the critical point.

2.2.2 Regular Solution Model

Mean field models of mixtures can describe the free energy density and predict features of the phase behaviour. Coarse grained order parameters, such as volume fractions provide a useful description of the system, where the volume fraction describes the local composition, but may not be homogeneous in the system. These order parameters describe the dynamics of an intermediate scale, much larger than the individual lattice sites and much smaller than the overall system size. The free energy density can be calculated from the Hamiltonian of a system and, again, the $A - B$ binary mixture is a useful place to start. Consider a lattice where each lattice site is occupied by either a molecule of A or a molecule of B where v_A and v_B (the size of each molecule) are the same and are equal to one lattice site. The total number of sites in the lattice is $N_{lat} = N_A + N_B$. The different molecules can be configured in many different ways on the lattice however the different configurations will have different energies due to interactions between the molecules. The lattice model can include these interactions by having different contributions to the energy for different pairs of molecules on neighbouring lattice sites. In general longer range interactions could also be considered, however here

we only consider nearest neighbour interactions. For example, two molecules of A on neighbouring sites will contribute ϵ_{AA} to the energy of a configuration, two molecules of B contribute ϵ_{BB} and a molecule of A on a neighbouring lattice site to a molecule of B will contribute ϵ_{AB}. The total energy of a configuration c is then the sum of the interaction energy contribution over all neighbouring lattice sites

$$E_c = N_c^{AA}\epsilon_{AA} + N_c^{AB}\epsilon_{AB} + N_c^{BB}\epsilon_{BB} \tag{2.4}$$

where N_c^{ij} is the number of unique neighbouring lattice site pairs, occupied by a molecule of i and molecule of j in the configuration. The free energy density can be calculated from the partition function, Z, as

$$f(\phi, T) = -\frac{k_\mathrm{B}T}{V}\ln Z \tag{2.5}$$

where k_B is the Boltzmann constant [33]. The partition function is directly calculated for a canonical ensemble via

$$Z = \sum_c \exp\left(-\beta E_c\right). \tag{2.6}$$

where $\beta = 1/k_\mathrm{B}T$ and the sum is over all configurations. In the thermodynamic limit of large N_{lat} the sum can be well approximated by a mean field approximation. That is, the probability distribution in configuration space becomes highly peaked around configurations with the average energy. The sum can therefore be approximated by replacing the energy of each configuration with the average energy, $\bar{E}$, so that (2.6) now becomes

$$Z \approx \sum_c \exp(-\beta\bar{E}) = \Omega\exp(-\beta\bar{E}) \tag{2.7}$$

where Ω is the number of unique configurations of molecules on the lattice and is given by

$$\Omega = \frac{N_{lat}!}{N_A!N_B!}. \tag{2.8}$$

The free energy density in the mean field model is now, with (2.5), $f = -\frac{K_BT}{V}(\ln\Omega + \bar{E})$.

The mean energy $\bar{E}$ can be calculated in the mean field model. The coordination number, z, describes the number of nearest neighbours of each lattice site, for example $z = 4$ in a square lattice. On average $z\phi_i$ of the neighbouring lattice sites will be occupied by a molecule of i. For $i \neq j$ the average number of ij neighbour pairs, $\bar{N}^{ij}$, is the number of sites occupied by a molecule of i multiplied by the average the number of neighbouring lattice sites occupied by a molecule of j: $\bar{N}^{ij} = N_{lat}\phi_i \times z\phi_j$. When $i = j$ each pair will be double counted (each lattice site occupied by a molecule of i will be considered as both the 'main' and 'neighbour' site) and so there is an additional factor of 1/2 to prevent double counting [31]. The average energy is therefore

$$\begin{aligned}\bar{E} &= \bar{N}^{AA}\epsilon_{AA} + \bar{N}^{AB}\epsilon_{AB} + \bar{N}^{BB}\epsilon_{BB} \\ &= \frac{1}{2}zN_{lat}\phi^2\epsilon_{AA} + zN_{lat}(1-\phi)\phi\epsilon_{AB} + \frac{1}{2}zN_{lat}(1-\phi)^2\epsilon_{BB}.\end{aligned} \tag{2.9}$$

Using (2.5) the free energy density is

$$f(\phi, T) = -\frac{k_\mathrm{B}T}{V}\left(\ln\left(\frac{N_{lat}!}{N_A!N_B!}\right) - \frac{zN_{lat}}{2}\left(\phi^2\epsilon_{AA} + 2(1-\phi)\phi\epsilon_{AB} + (1-\phi)^2\epsilon_{BB}\right)\right). \tag{2.10}$$

The first term is simplified using Stirling's formula, $\ln N! = N\ln N - N$ for large N to give $\ln\Omega = -N_{lat}(\phi\ln(\phi) + (1-\phi)\ln(1-\phi))$. The average energy term can be simplified as the phase behaviour is independent of the exact value of f, or $\partial f/\partial\phi$ and so the physics of the system is invariant under a transform $f \to f + k_1 + k_2\phi$. Specifically, choosing $k_1 = z\epsilon_{BB}/2$ and $k_2 = z(\epsilon_{BB} - \epsilon_{AA})/2$ the free energy now becomes

$$\frac{f(\phi, T)}{k_\mathrm{B}T} = \phi\ln(\phi) + (1-\phi)\ln(1-\phi) + \chi(1-\phi)\phi \tag{2.11}$$

where we have set the volume of each lattice site as 1, so that $V = N_{lat}$. Additionally, we have defined the Flory-Huggins interaction parameter $\chi = -\frac{z}{2k_BT}(\epsilon_{AA} + \epsilon_{BB} - 2\epsilon_{AB})$, which is the energy change when a molecule of A is taken from an environment of pure A and put into an environment of pure B. When $\chi < 0$ it is energetically favourable for the components to mix and when $\chi > 0$ it is favourable for the components to remain separate [31]. The spinodal region can be found by directly

calculating $\partial^2 f/\partial\phi^2$ and shows the existence of a critical point at $\phi_{\text{crit}} = 0.5$ and $\chi_{\text{crit}} = 2$. The system cannot phase separate when $\chi < 2$. The critical point must occur at $\phi_{\text{crit}} = 0.5$ as the system is symmetric under exchange of $A, B \to B, A$, however the homogeneous system can be stable for all ϕ even when mixed interactions are unfavourable $\chi > 0$. This is because when $0 < \chi < 2$, the entropic terms in the free energy contribute more than the cost of the interactions and so the system remains stable. In equilibrium theories of phase separation it is the interactions that drive the phase behaviour [1].

Generalisations of the Regular Solution Free Energy

The Flory-Huggins theory gives the free energy of a binary mixture in (2.11), however a similar form of the free energy can be extended to describe a broader class of mixtures. Consider a system of N components, where the mixture is made up of volume fraction ϕ_i of component i (i runs from 1 to N). In a system with non-conserved particle number (such as an active system discussed later) the free energy will have additional enthalpic terms. This is intrinsic energy from chemical bonds in a molecule of each species and is proportional to the number of molecules of that component, so that the enthalpic contribution to the free energy density is

$$f_{\text{enth}} = \sum_i \varepsilon_i \frac{\phi_i}{v_i} \tag{2.12}$$

where ε_i is the enthalpy per molecule of component i. If different components in the system have molecules that occupy more than one lattice site, then the previous calculation of Ω, the number of microstates, is overestimated, as nearby sites will necessarily be occupied by the same molecule. This modifies the entropic contribution to the free energy and the Flory-Huggins theory gives the entropic contribution as

$$f_{\text{entr}} = \sum_i k_{\text{B}} T \frac{\phi_i}{v_i} \ln \phi_i \tag{2.13}$$

as if a molecule is larger, then there are fewer molecules per volume and therefore fewer microstates [31]. Volume effects will also appear in the calculation of

the chemical potential, due to the conversion between volume fraction and the number of molecules

$$\mu_i = \frac{\partial F}{\partial N_i} = v_i \frac{\partial f}{\partial \phi_i}. \tag{2.14}$$

For a mixture of N components the full theory will describe interactions between all components so that the contribution to the free energy from interactions becomes

$$f_{\text{int}} = \sum_{i,j} \frac{\chi_{ij}}{2} \phi_i \phi_j. \tag{2.15}$$

where the sum denotes the double sum running from 1 to N for both indices, the factor of $1/2$ means each interaction is only counted once and the scalar interaction parameter, χ, has now become a matrix of interaction parameters, χ_{ij} [34]. It is convenient to use a symmetric form of the interaction matrix, so that $\chi_{ij} = \chi_{ji}$. The matrix can also be made to have a vanishing diagonal as follows. Noting incompressibility, $\sum_i \phi_i = 1$, gives

$$\begin{aligned} f_{\text{int}} &= \sum_{i,j} \frac{\chi_{ij}}{2} \phi_i \phi_j = \sum_i \left(c_i \phi_i - \left(\sum_j c_i \phi_i \phi_j \right) \right) + \sum_{i,j} \frac{\chi_{ij}}{2} \phi_i \phi_j \\ &= \sum_i c_i \phi_i + \sum_{i,j} \left(\frac{\chi_{ij}}{2} - c_i \right) \phi_i \phi_j, \end{aligned} \tag{2.16}$$

where the c_is are a set of N arbitrary constants. Defining $\tilde{\chi}_{ij} = \chi_{ij} - 2c_i$ and choosing $c_i = \chi_{ii}/2$ eliminates the diagonal term so that $\tilde{\chi}_{ii} = 0$ for all i. The $c_i \phi_i$ contribution can be contained into a modified enthalpic term which includes the intrinsic enthalpy and self interactions $\tilde{\varepsilon}_i \to \varepsilon_i + \chi_{ii/2}$. Since the free energy can be written in terms of these modified enthalpic terms and interaction terms, it is convenient to immediately drop the tildes and write the free energy using an interaction parameter with zeros on the diagonal.

The final contribution considered here describes an energy of interfaces and is related to the surface tensions between domains of different compositions. Similarly to the interaction term, in the case of an N component matrix, the interface contribution to the free energy will be composed of couplings between the gradients of the volume fractions of each component to give

$$f_{\text{surf}} = \sum_{i,j} \frac{\kappa_{ij}}{2} (\nabla \phi_i) \cdot (\nabla \phi_j) \tag{2.17}$$

where κ is an $N \times N$ matrix that recovers the surface tension in the system. Another consequence of incompressibility is $\sum_i \nabla\phi_i = 0$ and so

$$\begin{aligned} f_{\text{surf}} &= \sum_{i,j} \frac{\kappa_{ij}}{2} (\nabla\phi_i) \cdot (\nabla\phi_j) = \sum_{i,j} \frac{\kappa_{ij}}{2} (\nabla\phi_i) \cdot (\nabla\phi_j) - \sum_i \nabla\phi_i \cdot \left(\sum_j b_i \nabla\phi_j \right) \\ &= \sum_{i,j} \left(\frac{\kappa_{ij}}{2} - b_i \right) (\nabla\phi_i) \cdot (\nabla\phi_j) \end{aligned} \tag{2.18}$$

where setting $2b_i = \kappa_{ij}$ shows that the gauge of the system can be chosen such that $\kappa_{ii} = 0$. Additional terms that go like higher power gradient terms, or external potentials can be added to the free energy, however these ingredients capture all features of the classical theories of phase separation and the resulting dynamics.

The overall Flory Huggins free energy density, f_{FH}, is therefore

$$f_{\text{FH}} = \sum_{i=1}^{N} \left[\frac{\phi_i}{v_i} (k_{\text{B}} T \ln \phi_i + \varepsilon_i) + \sum_{j=1, j\neq i}^{N} \frac{\chi_{ij}}{2} \phi_i \phi_j + \sum_{j=1, j\neq i}^{N} \frac{\kappa_{ij}}{2} (\nabla\phi_i) \cdot (\nabla\phi_j) \right]. \tag{2.19}$$

2.3 Dynamics of Multi-Component Mixtures

2.3.1 Conserved Dynamics

Model B Dynamics

The static lattice picture can describe the free energy of a system, but, alone, does not describe associated dynamics. The lattice model can be extended to include the evolution of a system through configuration space by considering exchange of molecules of neighbouring lattice sites. In this picture (and also physically), the number of molecules of each species does not change and so the behaviour of the volume fraction for each component must obey a continuity equation, namely

$$\dot{\phi}_i = -\nabla \cdot \mathbf{J}_i \tag{2.20}$$

where i labels each component, and $\mathbf{J}_i$ is the volume fraction flux [27]. Assuming near equilibrium linear response [35], changes to the distribution of a component will be driven by changes in the free energy and will be proportional to the associated

thermodynamic force, specifically the chemical potential. The canonical Model B dynamics capture this chemical pressure and give the volume fraction flux as

$$\mathbf{J}_i = -\sum_j M_{ij} \nabla \mu_j + \mathbf{J}^N \tag{2.21}$$

where μ_i is the chemical potential of the i^{th} component, M_{ij} is a set of generalised mobilities and the sum runs over all components in the system [27], [36]. The $\mathbf{J}^N$ term describes the noise and must obey the appropriate fluctuation dissipation theorems. In the thermodynamic limit of a noise free model considered here the $\mathbf{J}^N$ contribution vanishes. The chemical potential for each component, μ_i, is given by

$$\mu_i = v_i \frac{\delta f}{\delta \phi_i}, \tag{2.22}$$

where the functional derivative is used since ϕ_i depends on position.

Mobilities for Incompressible Models

The model B dynamics introduce a set of transport coefficients, or mobilities M_{ij}, which describe how the volume fraction of the i^{th} component responds to the chemical potential of the j^{th} component. This is a general form of the linear transport relationship found near equilibrium in thermodynamic systems where the spatial fluxes, J_i are proportional to a set of generalised conjugate thermodynamic forces, X_j, so that $J_i = \sum_j L_{ij} X_j$. The phenomenological coefficients are L_{ij} and define a matrix that must be positive semidefinite to ensure a non-negative entropy production rate. Considering the fluxes of each component, as in (2.21), we similarly find that the matrix defined by M_{ij} must be positive semidefinite. Additionally, from the Onsager reciprocal relations, the transport coefficients of the particle fluxes must be symmetric under exchange of $i, j \to j, i$. Here however, the flux describes the transport of volume fraction rather than particle number and so the forces and displacements are not conjugate [35]. As such the reciprocity is broken and $M_{ij} \neq M_{ji}$, however again using the size of individual molecules to convert between volume fraction and number density gives

$$M_{ij} = \frac{v_i}{v_j} M_{ji}. \tag{2.23}$$

In this work, we assume that the mixture is incompressible. This simplifies calculating the non-conserved dynamics (see Section 2.3.2) and is consistent with biologically relevant aqueous solutions. An incompressible model requires $\sum_i \phi_i = 1$ and so $\sum_i \dot{\phi}_i = 0$. Substituting in the Model B dynamics, (2.20) and (2.21) give

$$\sum_i \dot{\phi}_i = \sum_i \nabla \cdot \left(\sum_j M_{ij} \nabla \mu_j \right) = \sum_j \nabla \cdot \left(\left(\sum_i M_{ij} \right) \nabla \mu_j \right) = 0. \tag{2.24}$$

In order for this to be true in general, for non-uniform systems, i.e. $\nabla \mu_j \neq 0$, it is necessary for the mobilities to satisfy

$$\sum_i M_{ij} = 0 \tag{2.25}$$

which constrains the mobilities and enforces that the fluid remains incompressible [37]. An N-component mixture, has a total of $N \times N$ mobilities. The reciprocity-like constraint in (2.23) reduces the number of free parameters to $N(N+1)/2$ and the incompressibility condition adds a further N constraints to give $N(N-1)/2$ free mobility parameters.

2.3.2 Non-Conserved Dynamics

Reaction Rates

In addition to spatial fluxes of component from the Model B dynamics, chemically active mixtures will also permit fluxes in chemical space, i.e. the conversion of a molecule of i to a molecule of j. Putting these dynamics into the binary mixture, we allow the reaction $A \rightleftharpoons B$, and an immediate consequence of incompressibility is that the reaction must conserve volume, so here $v_A = v_B$. In general the volume of the reactants must equal the volume of the products which is simple for this 1:1 stoichiometry but could be more complex for non-conserved molecule number. The change in the free energy due to the reaction is $dF = \mu_A dN_A + \mu_B dN_B = (\mu_A - \mu_B) dN_A$ where $dN_A = -dN_B$ by conservation of total molecule number. There is therefore no net conversion between molecules of A and B when $\mu_A = \mu_B$.

Considering detailed balance [32] for the system constrains the relationship between the forward and backward reaction rates

$$\frac{r_{A\to B}}{r_{B\to A}} = \exp\left(\frac{\mu_A - \mu_B}{k_B T}\right) \tag{2.26}$$

which allows us to identify the net transfer from $A \to B$ as

$$r_{A\to B} - r_{B\to A} = K\left(\exp\left(\frac{\mu_A - \mu_B}{k_B T}\right) - 1\right) \tag{2.27}$$

where the prefactor K is to be determined, but constrained to be positive. This makes sense as if $\mu_A > \mu_B$ then we have net $A \to B$, when $\mu_B > \mu_A$ then we have net $B \to A$ and as expected there is no net flux for $\mu_A = \mu_B$ [32]. The rate still depends on K, which could be constant, or a function of system parameters. Typically we choose K to recover mass action kinetics.

Enzymatic Activity

Enzymes act as catalysts in biological reactions and increase the rate of a reaction, for example by lowering the activation energy. The increase in rate can effectively toggle a reaction so that it can only happen in the presence of this *enzyme* component. We consider a reaction that converts A to B where there are additional *Fuel* reactants and additional *Waste* products,

$$\text{Enzyme} + \text{Fuel} + A \leftrightharpoons \text{Enzyme} + \text{Waste} + B. \tag{2.28}$$

We assume that the system is in contact with a Fuel and Waste reservoir that maintains constant chemical potentials, μ_{Fuel} and μ_{Waste}, and define $\Delta\mu \equiv \mu_{Fuel} - \mu_{Waste}$ which is also constant and drives the reaction. Alternatively, $\Delta\mu$ could represent the energy transferred by a photon in a light-activated catalytic reaction. Using (2.26) the rate of $A \to B$ of this reaction in the presence of the enzyme can be written as

$$r_{A\to B,E} - r_{B\to A,E} = K'\rho_{\mathrm{E}}\left(\exp\left(\frac{\mu_A - \mu_B + \Delta\mu}{k_B T}\right) - 1\right) \tag{2.29}$$

where the reaction rate is proportional to the local concentration of the enzyme component, ρ_{E}, and K' is a modified rate prefactor. Reaction kinetics of enzymes

are often described using Michaelis–Menten kinetics with $r_{A\to B} \sim \rho_{\mathrm{E}}\rho_{\mathrm{A}}/(K_M + \rho_{\mathrm{A}})$ where K_M is the Michaelis constant and ρ_{A} is the concentration of the substrate, A [38]. In both descriptions of the kinetics, the rate increases linearly with ρ_{E} and K' could be modified to include the Michaelis–Menten kinetics in the substrate concentration. The description given by (2.29) is more complete and can capture the effect of interactions on the rate of conversion.

2.4 Minimal Model of an Active Mixture

The simplest model that will encapsulate all of these effects requires at least two components for a chemical reaction to occur, e.g. $S \rightleftharpoons P$ (substrate to product) and a third enzyme component (E), that permits the driven, catalytic reaction described in (2.29). At every point in space and time the system is parameterised by three volume fractions; $\phi_{\mathrm{s}}(\boldsymbol{r}, t)$, $\phi_{\mathrm{p}}(\boldsymbol{r}, t)$ and $\phi_{\mathrm{e}}(\boldsymbol{r}, t)$, corresponding to individual molecules of volume v_{s}, v_{p} and v_{e} respectively. The mixture is incompressible and so $\phi_{\mathrm{s}} + \phi_{\mathrm{p}} + \phi_{\mathrm{e}} = 1$ everywhere and consequently the reaction requires, $v_{\mathrm{s}} = v_{\mathrm{p}}$. In living systems, enzymes have much more complex structures than reactants and so we expect the size of this component to be much larger $v_{\mathrm{e}} > v_{\mathrm{s}}, v_{\mathrm{p}}$ [3]. This increased size is also expected to result in increased viscous drag and reduced mobility for an enzyme compared to the other components. The Flory-Huggins theory of suspensions gives the free energy of the system as $F = \int \mathrm{d}\boldsymbol{r}\, f_{\mathrm{FH}}$, with the free energy density

$$f_{\mathrm{FH}}(\{\phi_i\}) = \sum_{i=1}^{N} \frac{1}{v_i}\Big[\varepsilon_i\phi_i + k_{\mathrm{B}}T\phi_i \log\phi_i\Big], \tag{2.30}$$

where ε_i is the enthalpy of component i. Importantly, we do not include any interaction terms in the free energy, in particular f_{FH} does not contain terms of the usual form $\chi_{ij}\phi_i\phi_j$. This implies that phase separation in this system would be impossible at equilibrium. The chemical potential of a component is given by

$$\mu_i = \varepsilon_i + k_{\mathrm{B}}T\log\phi_i + 1 \quad \text{and so} \quad \nabla\mu_i = k_{\mathrm{B}}T\frac{1}{\phi_i}\nabla\phi_i \tag{2.31}$$

which drives the conserved dynamics of Model B. For the mobilities we assume the common form where

$$M_{ij} = -\beta D_{ij}\phi_i\phi_j \quad \text{for } i \neq j \tag{2.32}$$

and $\beta \equiv (k_{\mathrm{B}}T)^{-1}$ [39]. The mobility constraints imply $M_{jj} = -\sum_{i\neq j} M_{ij}$ and $v_j D_{ij} = v_i D_{ji}$ [37], [40], [41]. The transport coefficients D_{ij} determine the rate at which the components respond to local effective concentration gradients and exchange positions, and as such are inherently related to the phenomena of diffusiophoresis, cross-diffusion and Maxwell-Stefan diffusion.

We make the model active by allowing non-equilibrium (fuelled) conversion between two components, substrate (S) and product (P), catalysed by an enzyme (E). This can be described by the reaction E+S+F $\rightleftharpoons$ E+P+W, where F and W represent fuel and waste molecules, respectively (as discussed in Section 2.3.2). We do not model the dynamics of the fuel and waste here, but assume $\Delta\mu \equiv \mu_{\mathrm{f}} - \mu_{\mathrm{w}}$ is constant. The catalysed reaction converts substrate to product with rate r_{cat} and we also model the spontaneous reaction (that does not require enzyme) which converts substrate to product at rate r_{spo} (note that these contributions might be negative as this flux is always expressed in the direction $S \to P$). Evaluating (2.27) and (2.29) with the chemical potential from (2.31) gives

$$r_{\mathrm{spo}} = r_{\mathrm{spo}}^{\mathrm{S}\to\mathrm{P}} - r_{\mathrm{spo}}^{\mathrm{P}\to\mathrm{S}} = k_{\mathrm{spo}}[e^{\beta\Delta\varepsilon}\phi_{\mathrm{s}} - \phi_{\mathrm{p}}], \tag{2.33}$$

$$r_{\mathrm{cat}} = r_{\mathrm{cat}}^{\mathrm{S}\to\mathrm{P}} - r_{\mathrm{cat}}^{\mathrm{P}\to\mathrm{S}} = k_{\mathrm{cat}}\phi_{\mathrm{e}}[\phi_{\mathrm{s}} - \phi_{\mathrm{p}}e^{-\beta(\Delta\varepsilon+\Delta\mu)}], \tag{2.34}$$

where $\Delta\varepsilon = \varepsilon_S - \varepsilon_P$. The rate constants here have been scaled to better disentangle the effects of the various parameters; $k_{spo} = K_{spo}/\phi_P$ and $k_{cat} = K_{cat}e^{-(\Delta\varepsilon+\Delta\mu)}/(v_{\mathrm{e}}\phi_P)$. We will typically take $\Delta\varepsilon < 0$ and $\Delta\varepsilon + \Delta\mu > 0$, so that the spontaneous and catalysed reactions run preferentially in the P$\to$S and S$\to$P directions, respectively.

Combining the conserved and non-conserved dynamics and defining $R \equiv r_{\mathrm{spo}} +$

r_{cat} results in the evolution equations for the three-component system

$$\dot{\phi_{\mathrm{e}}} = \boldsymbol{\nabla} \cdot \Big(M_{\mathrm{ee}} \boldsymbol{\nabla} \mu_{\mathrm{e}} + M_{\mathrm{es}} \boldsymbol{\nabla} \mu_{\mathrm{s}} + M_{\mathrm{ep}} \boldsymbol{\nabla} \mu_{\mathrm{p}} \Big), \tag{2.35}$$

$$\dot{\phi_{\mathrm{s}}} = \boldsymbol{\nabla} \cdot \Big(M_{\mathrm{se}} \boldsymbol{\nabla} \mu_{\mathrm{e}} + M_{\mathrm{ss}} \boldsymbol{\nabla} \mu_{\mathrm{s}} + M_{\mathrm{sp}} \boldsymbol{\nabla} \mu_{\mathrm{p}} \Big) - R, \tag{2.36}$$

$$\dot{\phi_{\mathrm{p}}} = \boldsymbol{\nabla} \cdot \Big(M_{\mathrm{pe}} \boldsymbol{\nabla} \mu_{\mathrm{e}} + M_{\mathrm{ps}} \boldsymbol{\nabla} \mu_{\mathrm{s}} + M_{\mathrm{pp}} \boldsymbol{\nabla} \mu_{\mathrm{p}} \Big) + R. \tag{2.37}$$

2.5 Catalysis-Induced Phase Separation

2.5.1 Stability of the Homogeneous Steady State

The minimal model in (2.35)–(2.37) has a homogeneous steady-state solution when $R = 0$. Since the enzyme component is conserved in the system we can define ϕ_{e}^* as the average enzyme volume fraction in the initialisation of a system, such that the total volume of enzyme component in the system is $V\phi_{\mathrm{e}}^*$. Given a ϕ_{e}^*, solving $R = 0$ gives steady state volume fraction for the substrate and product components

$$\phi_{\mathrm{s}}^* = \phi_{\mathrm{s+p}}^* \frac{k_{\mathrm{spo}} + k_{\mathrm{cat}} \phi_{\mathrm{e}}^* e^{-\beta(\Delta\varepsilon + \Delta\mu)}}{k_{\mathrm{spo}} + k_{\mathrm{cat}} \phi_{\mathrm{e}}^* e^{-\beta(\Delta\varepsilon + \Delta\mu)} + k_{\mathrm{spo}} e^{\beta\Delta\varepsilon} + k_{\mathrm{cat}} \phi_{\mathrm{e}}^*} \tag{2.38}$$

$$\phi_{\mathrm{p}}^* = \phi_{\mathrm{s+p}}^* \frac{k_{\mathrm{spo}} e^{\beta\Delta\varepsilon} + k_{\mathrm{cat}} \phi_{\mathrm{e}}^*}{k_{\mathrm{spo}} + k_{\mathrm{cat}} \phi_{\mathrm{e}}^* e^{-\beta(\Delta\varepsilon + \Delta\mu)} + k_{\mathrm{spo}} e^{\beta\Delta\varepsilon} + k_{\mathrm{cat}} \phi_{\mathrm{e}}^*} \tag{2.39}$$

with $\phi_{\mathrm{s+p}}^* = 1 - \phi_{\mathrm{e}}^*$, which is the average volume fraction of the substrate and product combined ($\phi_{\mathrm{s+p}}^* = \phi_{\mathrm{s}}^* + \phi_{\mathrm{p}}^*$) and is also conserved.

We can study the linear stability of this homogeneous steady-state by considering a small perturbation $\phi_i(\boldsymbol{r}, t) = \phi_i^* + \delta\phi_i(\boldsymbol{r}, t)$, giving $\mu_i(\boldsymbol{r}, t) = \mu_i^* + \delta\mu_i(\boldsymbol{r}, t)$ and define mobilities at the homogeneous steady state $M_{ij}^* = M_{ij}(\phi_{\mathrm{e}}^*, \phi_{\mathrm{s}}^*, \phi_{\mathrm{p}}^*)$. Setting $\beta = 1$, to first order in the perturbation $\delta\mu(\boldsymbol{r}, t) = \frac{\delta\phi_i(\boldsymbol{r}, t)}{\phi_i^*}$ and thus $\boldsymbol{\nabla}\mu_i(\boldsymbol{r}, t) = \frac{1}{\phi_i^*}\boldsymbol{\nabla}\delta\phi_i(\boldsymbol{r}, t)$. Additionally, define how the reaction rate changes under a small change in ϕ_i to be R_i, such that $R = R_{\mathrm{s}}\delta\phi_{\mathrm{s}} - R_{\mathrm{p}}\delta\phi_{\mathrm{p}} + R_{\mathrm{e}}\delta\phi_{\mathrm{e}}$ where the sign changes for the product component to keep $R_{\mathrm{p}} > 0$. This gives

$$R_{\mathrm{s}} \equiv k_{\mathrm{spo}} e^{\beta\Delta\varepsilon} + k_{\mathrm{cat}} \phi_{\mathrm{e}}^* \tag{2.40}$$

$$R_{\mathrm{p}} \equiv k_{\mathrm{spo}} + k_{\mathrm{cat}} \phi_{\mathrm{e}}^* e^{-\beta(\Delta\varepsilon + \Delta\mu)} \tag{2.41}$$

$$R_{\mathrm{e}} \equiv k_{\mathrm{cat}}[\phi_{\mathrm{s}}^* - \phi_{\mathrm{p}}^* e^{-\beta(\Delta\varepsilon + \Delta\mu)}] = \phi_{\mathrm{s+p}}^* \frac{k_{\mathrm{cat}} k_{\mathrm{spo}} (1 - e^{-\beta\Delta\mu})}{k_{\mathrm{spo}} + k_{\mathrm{cat}} \phi_{\mathrm{e}}^* e^{-\beta(\Delta\varepsilon + \Delta\mu)} + k_{\mathrm{spo}} e^{\beta\Delta\varepsilon} + k_{\mathrm{cat}} \phi_{\mathrm{e}}^*}. \tag{2.42}$$

It is convenient to consider the perturbations in Fourier space as $\delta\phi_i(\boldsymbol{q},t)$ where $\boldsymbol{q}$ is the spatial frequency of a perturbation so that $\delta\phi_i(\boldsymbol{q},t) = |\delta\phi_i(t)| \exp\left(\boldsymbol{q}\cdot\boldsymbol{r}\sqrt{-1}\right)$. The governing equations then become

$$\begin{pmatrix}\dot{\delta\phi_\mathrm{e}}\\ \dot{\delta\phi_\mathrm{s}}\\ \dot{\delta\phi_\mathrm{p}}\end{pmatrix} = \underbrace{\begin{pmatrix}(M^*_{\mathrm{se}}+M^*_{\mathrm{pe}})\frac{\boldsymbol{q}^2}{\phi^*_\mathrm{e}} & -M^*_{\mathrm{se}}\frac{v_\mathrm{e}}{v_\mathrm{s}}\frac{\boldsymbol{q}^2}{\phi^*_\mathrm{s}} & -M^*_{\mathrm{pe}}\frac{v_\mathrm{e}}{v_\mathrm{s}}\frac{\boldsymbol{q}^2}{\phi^*_\mathrm{p}}\\ -M^*_{\mathrm{se}}\frac{\boldsymbol{q}^2}{\phi^*_\mathrm{e}}-R_\mathrm{e} & \left(M^*_{\mathrm{sp}}+M^*_{\mathrm{se}}\frac{v_\mathrm{e}}{v_\mathrm{s}}\right)\frac{\boldsymbol{q}^2}{\phi^*_\mathrm{s}}-R_\mathrm{s} & -M^*_{\mathrm{sp}}\frac{\boldsymbol{q}^2}{\phi^*_\mathrm{p}}+R_\mathrm{p}\\ -M^*_{\mathrm{pe}}\frac{\boldsymbol{q}^2}{\phi^*_\mathrm{e}}+R_\mathrm{e} & -M^*_{\mathrm{sp}}\frac{\boldsymbol{q}^2}{\phi^*_\mathrm{s}}+R_\mathrm{s} & \left(M^*_{\mathrm{pe}}\frac{v_\mathrm{e}}{v_\mathrm{s}}+M^*_{\mathrm{sp}}\right)\frac{\boldsymbol{q}^2}{\phi^*_\mathrm{p}}-R_\mathrm{p}\end{pmatrix}}_{\mathcal{C}}\begin{pmatrix}\delta\phi_\mathrm{e}\\ \delta\phi_\mathrm{s}\\ \delta\phi_\mathrm{p}\end{pmatrix} \tag{2.43}$$

where the dot indicates the time derivative. In this formulation, we can explicitly see the incompressibility being imposed as the columns of $\mathcal{C}$ sum to zero. We now eliminate one of the components, e.g. $\delta\phi_\mathrm{p} = -\delta\phi_\mathrm{e} - \delta\phi_\mathrm{s}$, and define a 2×2 matrix, $\mathcal{K}$, describing the evolution of the remaining components. This is obtained from $\mathcal{C}$ by subtracting the last column from the other two (i.e. $\mathcal{K}_{ij} = \mathcal{C}_{ij} - \mathcal{C}_{i3}$ for $i,j \in 1,2$), giving

$$\begin{pmatrix}\dot{\delta\phi_\mathrm{e}}\\ \dot{\delta\phi_\mathrm{s}}\end{pmatrix} = \underbrace{\begin{pmatrix}(M^*_{\mathrm{se}}+M^*_{\mathrm{pe}})\frac{\boldsymbol{q}^2}{\phi^*_\mathrm{e}}+M^*_{\mathrm{pe}}\frac{v_\mathrm{e}}{v_\mathrm{s}}\frac{\boldsymbol{q}^2}{\phi^*_\mathrm{p}} & -M^*_{\mathrm{se}}\frac{v_\mathrm{e}}{v_\mathrm{s}}\frac{\boldsymbol{q}^2}{\phi^*_\mathrm{s}}+M^*_{\mathrm{pe}}\frac{v_\mathrm{e}}{v_\mathrm{s}}\frac{\boldsymbol{q}^2}{\phi^*_\mathrm{p}}\\ -M^*_{\mathrm{se}}\frac{\boldsymbol{q}^2}{\phi^*_\mathrm{e}}-R_\mathrm{e}+M^*_{\mathrm{sp}}\frac{\boldsymbol{q}^2}{\phi^*_\mathrm{p}}-R_\mathrm{p} & \left(M^*_{\mathrm{sp}}+M^*_{\mathrm{se}}\frac{v_\mathrm{e}}{v_\mathrm{s}}\right)\frac{\boldsymbol{q}^2}{\phi^*_\mathrm{s}}-R_\mathrm{s}+M^*_{\mathrm{sp}}\frac{\boldsymbol{q}^2}{\phi^*_\mathrm{p}}-R_\mathrm{p}\end{pmatrix}}_{\mathcal{K}}\begin{pmatrix}\delta\phi_\mathrm{e}\\ \delta\phi_\mathrm{s}\end{pmatrix}. \tag{2.44}$$

The eigenvalues of $\mathcal{K}$ determine the stability of the steady state. The system is stable if and only if all eigenvalues of $\mathcal{K}$ are negative. The Onsager relations and the non-negativity of R_i mean $\mathcal{K}_{1,1}$ and $\mathcal{K}_{2,2}$ are always negative, so $\mathrm{tr}(\mathcal{K}) < 0$ and there is therefore one positive eigenvalue if $\det(\mathcal{K}) < 0$. The instability condition then becomes

$$\begin{aligned}\left((M^*_{\mathrm{se}}+M^*_{\mathrm{pe}})\frac{\boldsymbol{q}^2}{\phi^*_\mathrm{e}}+M^*_{\mathrm{pe}}\frac{v_\mathrm{e}}{v_\mathrm{s}}\frac{\boldsymbol{q}^2}{\phi^*_\mathrm{p}}\right)&\left(\left(M^*_{\mathrm{sp}}+M^*_{\mathrm{se}}\frac{v_\mathrm{e}}{v_\mathrm{s}}\right)\frac{\boldsymbol{q}^2}{\phi^*_\mathrm{s}}-R_\mathrm{s}+M^*_{\mathrm{sp}}\frac{\boldsymbol{q}^2}{\phi^*_\mathrm{p}}-R_\mathrm{p}\right)\\ &< \left(-M^*_{\mathrm{se}}\frac{v_\mathrm{e}}{v_\mathrm{s}}\frac{\boldsymbol{q}^2}{\phi^*_\mathrm{s}}+M^*_{\mathrm{pe}}\frac{v_\mathrm{e}}{v_\mathrm{s}}\frac{\boldsymbol{q}^2}{\phi^*_\mathrm{p}}\right)\left(-M^*_{\mathrm{se}}\frac{\boldsymbol{q}^2}{\phi^*_\mathrm{e}}-R_\mathrm{e}+M^*_{\mathrm{sp}}\frac{\boldsymbol{q}^2}{\phi^*_\mathrm{p}}-R_\mathrm{p}\right).\end{aligned} \tag{2.45}$$

When $\boldsymbol{q}$ is very large, we expect the system to be stable as in this regime the evolution is dominated by diffusive relaxation. For $\boldsymbol{q} = 0$, the system is at critical stability due to global conservation, as this corresponds to a uniform change in ϕ_i. As such, since it only depends on $\boldsymbol{q}^2$ and $\boldsymbol{q}^4$, the instability condition is

satisfied if and only if it is satisfied for very small $\boldsymbol{q}^2$. With this in mind we take (2.45) to order $\sim \boldsymbol{q}^2$ which gives

$$\frac{1}{v_\mathrm{e}\phi_\mathrm{e}^*} + \frac{1}{v_\mathrm{s}(1-\phi_\mathrm{e}^*)} < \frac{R_\mathrm{e}}{v_\mathrm{s}(1-\phi_\mathrm{e}^*)}\left(\frac{\gamma_\mathrm{p}}{R_\mathrm{s}} - \frac{\gamma_\mathrm{s}}{R_\mathrm{p}}\right) \tag{2.46}$$

where we have defined

$$\gamma_\mathrm{s} \equiv \frac{M_\mathrm{se}^*}{M_\mathrm{se}^* + M_\mathrm{pe}^*} \quad \text{and} \quad \gamma_\mathrm{p} \equiv \frac{M_\mathrm{pe}^*}{M_\mathrm{se}^* + M_\mathrm{pe}^*}. \tag{2.47}$$

This condition can also be written to constrain the relative volumes in the system

$$\frac{v_\mathrm{s}}{v_\mathrm{e}} < \frac{\phi_\mathrm{e}^*}{1-\phi_\mathrm{e}^*}\left[R_\mathrm{e}\left(\frac{\gamma_\mathrm{p}}{R_\mathrm{s}} - \frac{\gamma_\mathrm{s}}{R_\mathrm{p}}\right) - 1\right], \tag{2.48}$$

which shows that the instability is favoured by larger enzymes, the biologically relevant case. With the common choice of mobilities ($M_\mathrm{es} = -\beta D_\mathrm{se}\phi_\mathrm{e}\phi_\mathrm{s}$ and $M_\mathrm{pe} = -\beta D_\mathrm{pe}\phi_\mathrm{e}\phi_\mathrm{p}$) the instability condition becomes

$$\frac{1}{v_\mathrm{e}\phi_\mathrm{e}^*} + \frac{1}{v_\mathrm{s}(1-\phi_\mathrm{e}^*)} < \frac{R_\mathrm{e}}{v_\mathrm{s}(1-\phi_\mathrm{e}^*)}\frac{D_\mathrm{pe} - D_\mathrm{se}}{D_\mathrm{pe}R_\mathrm{s} + D_\mathrm{se}R_\mathrm{p}}. \tag{2.49}$$

A system satisfying this inequality is unstable to small perturbations and as such this defines the spinodal line for the active minimal model. In calculating this condition, we eliminated the product component from the system and determined the stability by considering stability of the remaining two components. Eliminating either of the other components gives the same result. A quick check can be seen by noticing the stability condition is invariant under $S, P \to P, S$ and $R_\mathrm{e} \to -R_\mathrm{e}$. This is equivalent to considering the reaction terms in the opposite direction, or equivalently eliminating the substrate instead. Prior work often imposes incompressibility by eliminating one of the components in the free energy using $\phi_i = 1 - \sum_{j,j\neq i}\phi_j$. This can be useful when eliminating a solvent component, but in dense systems such as this three component mixture, all components need to be kept on an equal footing to see the coupling between responses to gradients as a consequence of the incompressibility.

Since the left hand side of (2.49) is always positive, an instability is possible only if the right hand side is positive as well. The sign of the right hand side is controlled by that of $(1 - e^{-\beta\Delta\mu})(D_\mathrm{pe} - D_\mathrm{se})$, which has several implications. First,

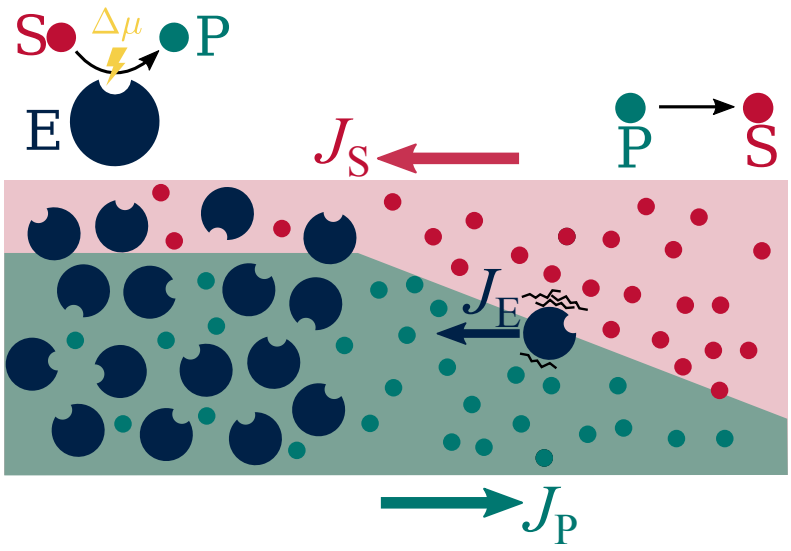

Figure 2.3: Processes leading to catalysis-induced phase separation (CIPS). (a) Enzymes convert substrate into product by a fuelled catalytic reaction, while product turns into substrate spontaneously. (b) The catalysed reaction creates gradients of substrate and product around enzyme-rich regions, which attract more enzymes when the off-diagonal transport coefficients coupling enzyme fluxes to product and substrate thermodynamic forces satisfy $D_{\mathrm{pe}} > D_{\mathrm{se}}$.

an equilibrium system with $\Delta\mu = 0$ is always stable, as expected from equilibrium theory of a multicomponent mixture with no interactions. Second, for a catalytic reaction favouring product formation with $\Delta\mu > 0$, an instability is possible only if $D_{\mathrm{pe}} > D_{\mathrm{se}}$. Third, if $D_{\mathrm{pe}} = D_{\mathrm{se}}$ the system is always stable. Intuitively, the instability arises from an enzyme rich region locally producing a higher concentration of product ($\Delta\mu > 0$) and creating a gradient of the product concentration. Due to the unequal response of the enzyme to gradients of substrate and product when $D_{\mathrm{pe}} > D_{\mathrm{se}}$, the enzyme will preferentially move up the product gradient towards the enzyme rich region, resulting in effective enzyme-enzyme attractive interactions and further aggregation. This process is governed by the activity and we call it *catalysis-induced phase separation* (CIPS). Figure 2.3 summarises this mechanism.

2.5.2 Numerical Simulation

Numerical solution of the evolution equations, (2.35)–(2.37), confirms the existence of this instability. We choose ϕ_{e}^* and solve for the steady state volume fractions of the other two components, ϕ_{s}^* and ϕ_{p}^*, using (2.38) and (2.39). We initialise a 1D

system with 200 grid points and a width of $200\sqrt{D_{\mathrm{se}}/k_{\mathrm{spo}}}$, with volume fraction $\phi_{\mathrm{e}}(x) = \phi_{\mathrm{e}}^* + \delta_\phi(x)$ where at every grid point, $\delta_\phi(x)$ is drawn from a uniform distribution between -0.005 and 0.005, to simulate spatial Gaussian noise. The initial substrate and product concentrations are given by $\phi_i(x) = \phi_i^* - \phi_i^*\delta_\phi(x)/(\phi_S^* + \phi_P^*)$, which enforces constant volume everywhere. We impose no-flux boundary conditions at the edge of the grid.

Figure 2.4 shows the spontaneous formation of regions of high and low enzyme concentrations when the system is unstable. Initially the large wavenumber, short length modes decay due to diffusive fluxes and following this longer wavelength modes are excited. Non-linear effects disrupt the growth of the Fourier modes and the system forms dense regions high in enzyme and dilute regions low in enzyme. These regions coarsen over time, ultimately resulting in two distinct phase-separated domains. Moreover, repeating this simulation with the same parameters but varying the amount of enzyme in the system, ϕ_{e}^*, only changes the relative size of the high and low concentration domains, without affecting the concentration values in the two domains. This observation suggests the existence of a binodal line, as in equilibrium phase separation. This behaviour can be observed for all parameters which we simulated ($k_{\mathrm{cat}}/k_{\mathrm{spo}} \approx$ 1–100, $v_{\mathrm{e}}/v_{\mathrm{s}} \approx$ 2–100, $-\Delta\varepsilon \approx$ 5–30$k_{\mathrm{B}}T$, $\Delta\mu \approx$ 5–50$k_{\mathrm{B}}T$, $D_{\mathrm{pe}}/D_{\mathrm{se}} \approx$ 1–100). The observation of macroscopic phase separation, rather than pattern formation or microphase separation, is further supported by the linear stability analysis showing an instability at the largest wavelengths ($q^2 \to 0$).

The growth rate of an unstable mode is given by the eigenvalues of $\mathcal{K}$ in equation (2.44). The fastest growing spatial frequency can be determined by maximising this eigenvalue. This straightforward maximisation gives a long expression which provides little insight, however, we approximate this mode by minimising the determinant with respect to $\mathbf{q}^2$ (since the trace also depends on $\mathbf{q}^2$ this will not be exact). We call spatial frequencies that minimise the determinant $\mathbf{q}_M$ and we find

$$\mathbf{q}_M^2 = \frac{(\phi_{\mathrm{e}}^* - 1)v_{\mathrm{s}}(\phi_{\mathrm{e}}^* v_{\mathrm{e}}(M_{\mathrm{pe}}R_{\mathrm{p}}(R_{\mathrm{e}} - R_{\mathrm{s}}) - M_{\mathrm{se}}R_{\mathrm{s}}(R_{\mathrm{e}} + R_{\mathrm{p}})) + (\phi_{\mathrm{e}}^* - 1)R_{\mathrm{p}}R_{\mathrm{s}}v_{\mathrm{s}}(M_{\mathrm{pe}} + M_{\mathrm{se}}))}{(R_{\mathrm{p}} + R_{\mathrm{s}})(\phi_{\mathrm{e}}^*(v_{\mathrm{e}} - v_{\mathrm{s}}) + v_{\mathrm{s}})(M_{\mathrm{sp}}v_{\mathrm{s}}(M_{\mathrm{pe}} + M_{\mathrm{se}}) + M_{\mathrm{pe}}M_{\mathrm{se}}v_{\mathrm{e}})}. \tag{2.50}$$

However, there will be a maximum value of $\mathbf{q}^2$ for unstable modes. Solving for

$\det \mathcal{K} = 0$, we find that modes with $\mathbf{q}^2 > 2\mathbf{q}_M^2$ will not be excited as for these frequencies $\mathcal{K}$ has two negative eigenvalues. For the system simulated in Figure 2.4 we find that only wavelengths longer than $15.8\sqrt{D_{\mathrm{se}}/k_{\mathrm{spo}}}$ are excited and the fastest growing mode has wavelength $22.6\sqrt{D_{\mathrm{se}}/k_{\mathrm{spo}}}$ (and is well approximated by (2.50) which gives $22.4\sqrt{D_{\mathrm{se}}/k_{\mathrm{spo}}}$). Additional studies of two-component mass-conserving reaction-diffusion systems have significant parallels to the minimal active model studied here and have shown coarsening leading to macrophase separation at long times [42], [43]. A useful next step therefore is to try to predict the dilute and dense phases theoretically.

2.5.3 Effective Free Energy and Binodal

In the macroscopic limit, we expect the substrate-product equilibrium in the bulk of each phase to be governed by the reaction terms that act locally, rather than by spatial diffusion. This implies that the substrate and product concentrations are enslaved to the enzyme concentration by $\phi_{\mathrm{s}} \approx \phi_{\mathrm{s}}^*(\phi_{\mathrm{e}})$ and $\phi_{\mathrm{p}} \approx \phi_{\mathrm{p}}^*(\phi_{\mathrm{e}})$, with the functions defined in (2.38) and (2.39). The system and its dynamics can now be described entirely as a function of the enzyme volume fraction ϕ_{e}. All volume fractions, chemical potentials and mobilities describing the system are enslaved to ϕ_{e}. As such (2.35) now becomes

$$\dot{\phi_{\mathrm{e}}} = \boldsymbol{\nabla} \cdot \left(\left(M_{\mathrm{ee}} \frac{\mathrm{d}\mu_{\mathrm{e}}}{\mathrm{d}\phi_{\mathrm{e}}} + M_{\mathrm{es}} \frac{\mathrm{d}\mu_{\mathrm{s}}}{\mathrm{d}\phi_{\mathrm{e}}} + M_{\mathrm{ep}} \frac{\mathrm{d}\mu_{\mathrm{p}}}{\mathrm{d}\phi_{\mathrm{e}}} \right) \boldsymbol{\nabla} \phi_{\mathrm{e}} \right). \tag{2.51}$$

We can recast the dynamics of the enzyme as $\dot{\phi_{\mathrm{e}}} \approx \boldsymbol{\nabla} \cdot (M_{\mathrm{ee}} \boldsymbol{\nabla} \mu_{\mathrm{eff}})$ with an effective chemical potential for the enzyme, μ_{eff}. In phase separating systems these reduced dynamics will not be well-behaved as the phase boundary will become infinitely sharp. This can be prevented by including a gradient term in the free energy that penalises sharp interfaces, for example a surface tension. Here, we express the dynamics as above to highlight the comparison to an equilibrium system where the phase behaviour can be determined by the free energy. The effective chemical potential satisfies

$$\boldsymbol{\nabla} \mu_{\mathrm{eff}} = \left(\frac{\mathrm{d}\mu_{\mathrm{e}}}{\mathrm{d}\phi_{\mathrm{e}}} + \frac{M_{\mathrm{es}}}{M_{\mathrm{ee}}} \frac{\mathrm{d}\mu_{\mathrm{s}}}{\mathrm{d}\phi_{\mathrm{e}}} + \frac{M_{\mathrm{ep}}}{M_{\mathrm{ee}}} \frac{\mathrm{d}\mu_{\mathrm{p}}}{\mathrm{d}\phi_{\mathrm{e}}} \right) \boldsymbol{\nabla} \phi_{\mathrm{e}}. \tag{2.52}$$

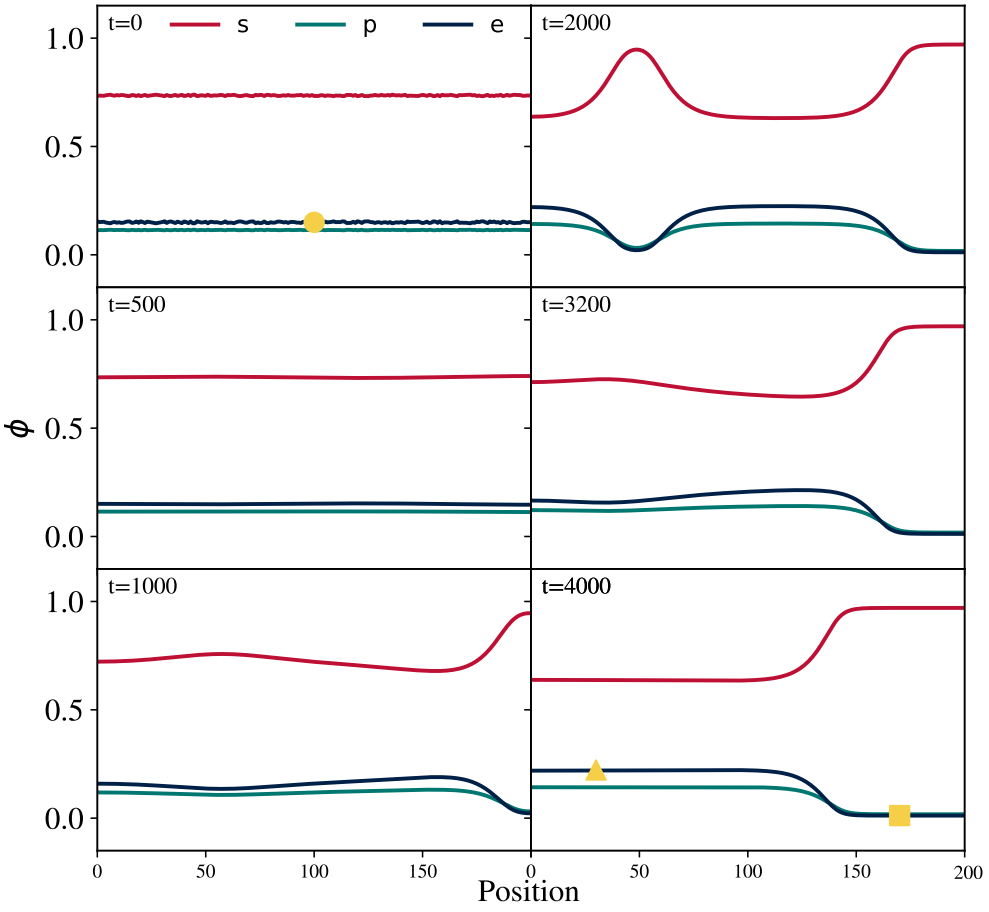

Figure 2.4: Numerical solution of an active mixture undergoing CIPS. The evolution of the system is shown at varying times. The time is non-dimensionalised by $20k_{\mathrm{spo}}$ and the length by $\sqrt{D_{\mathrm{se}}/k_{\mathrm{spo}}}$. The circle, triangle and square identify the homogeneous steady state and the dense and dilute enzyme phases, respectively, for comparison with Figure 2.5. The system is initialised with a uniform steady state of $\phi_{\mathrm{e}} = 0.15$, $\phi_{\mathrm{s}} = 0.736$, and $\phi_{\mathrm{p}} = 0.114$, with $\Delta\mu = 8k_{\mathrm{B}}T$, $k_{\mathrm{cat}}/k_{\mathrm{spo}} = 1$, $\Delta\varepsilon = -5k_{\mathrm{B}}T$, $D_{\mathrm{pe}} = 4D_{\mathrm{se}}$, and $D_{\mathrm{ps}} = 5D_{\mathrm{se}}$.

This means that by direct integration of the term in brackets with respect to ϕ_e we can calculate an effective chemical potential for the limit of fast reactions in the system. For the minimal model used here this integral can be evaluated exactly to give

$$\frac{\mu_{\text{eff}}(\phi_e)}{k_B T} = \log \phi_e - \frac{v_e}{v_s} \log[D_{se}\phi_s^*(\phi_e) + D_{pe}\phi_p^*(\phi_e)]. \tag{2.53}$$

We can also identify an effective free energy density $f_{\text{eff}}(\phi_e)$, such that $\mu_{\text{eff}} = v_e \frac{df_{\text{eff}}}{d\phi_e}$, which can be explicitly calculated by direct integration to give

$$\begin{aligned}\frac{f_{\text{eff}}(\phi_e)}{k_B T} = \frac{1}{v_p}\frac{k_{\text{spo}}}{k_{\text{cat}}}\Bigg(&\frac{1+e^{\beta\Delta\varepsilon}}{1+e^{-\beta(\Delta\varepsilon+\Delta\mu)}} \log\left[\frac{k_{\text{cat}}}{k_{\text{spo}}}\phi_e + e^{\beta(\Delta\varepsilon+\Delta\mu)}(1+e^{\beta\Delta\varepsilon}+\frac{k_{\text{cat}}}{k_{\text{spo}}}\phi_e)\right] \\ &- \frac{D_{se}+D_{pe}e^{\beta\Delta\varepsilon}}{D_{pe}+D_{se}e^{-\beta(\Delta\varepsilon+\Delta\mu)}} \log\left[D_{se}\frac{k_{\text{cat}}}{k_{\text{spo}}}\phi_e + e^{\beta(\Delta\varepsilon+\Delta\mu)}(D_{se}+D_{pe}e^{\beta\Delta\varepsilon}+D_{pe}\frac{k_{\text{cat}}}{k_{\text{spo}}}\phi_e)\right]\Bigg) \\ &+ \left(\frac{1}{v_p}-\frac{1}{v_e}\right)\phi_e + \frac{1}{v_p}\log[1-\phi_e] + \phi_e\left(\frac{1}{v_e}\log\phi_e - \frac{1}{v_p}\log[D_{se}\phi_s^*(\phi_e)+D_{pe}\phi_p^*(\phi_e)]\right).\end{aligned} \tag{2.54}$$

Since μ_{eff} can be determined up to a constant term, f_{eff} can be determined up to addition of an affine function in ϕ_e. The effective dynamics $\dot{\phi}_e \approx \boldsymbol{\nabla}\cdot(M_{ee}\boldsymbol{\nabla}\mu_{\text{eff}})$, with $\mu_{\text{eff}} = v_e f'_{\text{eff}}(\phi_e)$, drive the system towards a state that minimises the total effective free energy, under the constraints that the amount of enzyme and the volume of the system are conserved. Consequently, if the effective free energy is a good description of the system, the two phases the system forms should be predicted using the common tangent construction on the effective free energy. A variety of numerical methods can then be used to calculate the common tangent points as this problem is equivalent to finding the convex hull of the free energy [31], [44]. We then construct the binodal line by varying the system parameters and tracing out the points of coexisting phases. This graphical construction equates the chemical and mechanical pressure in the system, however it is important to note that here we are dealing with a nonequilibrium system, and moreover the effective pressure quantities were only obtained in the limit of fast reactions. In particular, as in other nonequilibrium systems [45], the thermodynamic pressure may not necessarily coincide with the mechanical pressure exerted by the system on the walls of its container.

Having obtained both the spinodal and binodal curves, we can construct the phase diagram for the minimal active mixture as shown in Figure 2.5. The phase separation is driven by the enzymatic activity and so the relevant control parameters in the system are the catalytic rate, $k_{\rm cat}$, and the strength of the non-equilibrium drive, $\Delta\mu$. As the strength of the enzymatic activity is decreased, the spinodal line (calculated from (2.49)) meets the binodal at a critical point showing good agreement. Below this critical point, the non-equilibrium drive is not strong enough to overcome diffusive fluxes and cause the phase separation. These results also agree with the numerics for the system, where initialising a system in the unstable region ended with two phases as predicted from the effective free energy.

2.5.4 Stability of a Four-Component System

An additional solvent component (e.g. water) can be added to the system similarly to the enzyme component, with conserved dynamics and no reaction terms. We label this component W with volume fraction $\phi_{\rm w}$. Following a similar procedure as for the no-solvent case, we can expand around a steady state where we now have $\phi^*_{\rm s+p} \neq 1-\phi^*_{\rm e}$ but $\phi^*_{\rm w} = 1-\phi^*_{\rm s+p}-\phi^*_{\rm e}$ where, similarly to the enzyme component, $\phi^*_{\rm w}$ is the average volume fraction of component W and is constant in the system. We can eliminate the solvent volume fraction to give a 3×3 matrix describing the evolution of the E, S, and P volume fractions

$$(\delta\dot{\phi}_{\rm e}, \delta\dot{\phi}_{\rm s}, \delta\dot{\phi}_{\rm p})^T = \mathcal{K}_{\rm w}(\delta\phi_{\rm e}, \delta\phi_{\rm s}, \delta\phi_{\rm p})^T \tag{2.55}$$

with

$$\mathcal{K}_{\rm w} = \begin{pmatrix} (M^*_{\rm se}+M^*_{\rm pe}+M^*_{\rm we})\frac{\boldsymbol{q}^2}{\phi^*_{\rm e}} + M^*_{\rm we}\frac{v_{\rm e}}{v_{\rm w}}\frac{\boldsymbol{q}^2}{\phi^*_{\rm w}} & -M^*_{\rm se}\frac{v_{\rm e}}{v_{\rm s}}\frac{\boldsymbol{q}^2}{\phi^*_{\rm s}} + M^*_{\rm we}\frac{v_{\rm e}}{v_{\rm w}}\frac{\boldsymbol{q}^2}{\phi^*_{\rm w}} & -M^*_{\rm pe}\frac{v_{\rm e}}{v_{\rm s}}\frac{\boldsymbol{q}^2}{\phi^*_{\rm p}} + M^*_{\rm we}\frac{v_{\rm e}}{v_{\rm w}}\frac{\boldsymbol{q}^2}{\phi^*_{\rm w}} \\ -M^*_{\rm se}\frac{\boldsymbol{q}^2}{\phi^*_{\rm e}} - R_{\rm e} + M^*_{\rm ws}\frac{v_{\rm s}}{v_{\rm w}}\frac{\boldsymbol{q}^2}{\phi^*_{\rm w}} & (M^*_{\rm se}\frac{v_{\rm e}}{v_{\rm s}}+M^*_{\rm sp}+M^*_{\rm ws})\frac{\boldsymbol{q}^2}{\phi^*_{\rm s}} - R_{\rm s} + M^*_{\rm ws}\frac{v_{\rm s}}{v_{\rm w}}\frac{\boldsymbol{q}^2}{\phi^*_{\rm w}} & -M^*_{\rm sp}\frac{\boldsymbol{q}^2}{\phi^*_{\rm p}} + R_{\rm p} + M^*_{\rm ws}\frac{v_{\rm s}}{v_{\rm w}}\frac{\boldsymbol{q}^2}{\phi^*_{\rm w}} \\ -M^*_{\rm pe}\frac{\boldsymbol{q}^2}{\phi^*_{\rm e}} + R_{\rm e} + M^*_{\rm wp}\frac{v_{\rm s}}{v_{\rm w}}\frac{\boldsymbol{q}^2}{\phi^*_{\rm w}} & -M^*_{\rm sp}\frac{\boldsymbol{q}^2}{\phi^*_{\rm s}} + R_{\rm s} + M^*_{\rm wp}\frac{v_{\rm s}}{v_{\rm w}}\frac{\boldsymbol{q}^2}{\phi^*_{\rm w}} & (M^*_{\rm pe}\frac{v_{\rm e}}{v_{\rm s}}+M^*_{\rm sp}+M^*_{\rm wp})\frac{\boldsymbol{q}^2}{\phi^*_{\rm p}} - R_{\rm p} + M^*_{\rm wp}\frac{v_{\rm s}}{v_{\rm w}}\frac{\boldsymbol{q}^2}{\phi^*_{\rm w}} \end{pmatrix}. \tag{2.56}$$

We now assume that the substrate and product dynamics are fast in comparison to the enzyme. Setting $\delta\dot{\phi}_{\rm s} = \delta\dot{\phi}_{\rm p} = 0$ gives

$$\delta\dot{\phi}_{\rm e} = (\mathcal{K}^{-1}_{\rm w})_{1,1}\delta\phi_{\rm e} \tag{2.57}$$

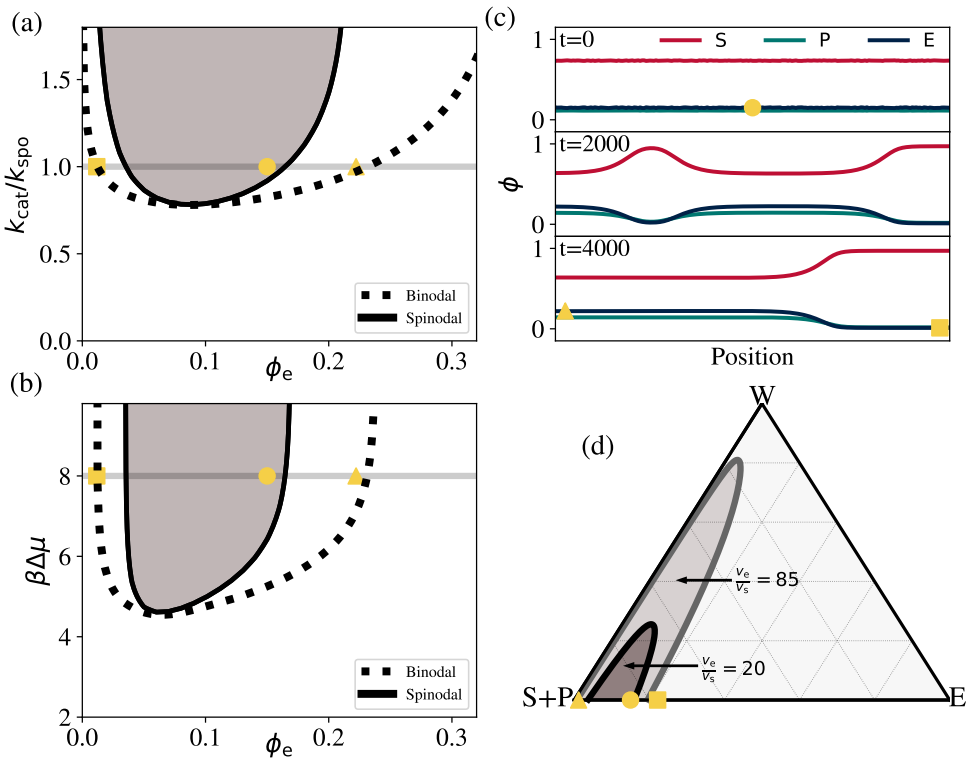

Figure 2.5: Phase behaviour and onset of CIPS. (a,b) Spinodal lines [from (2.49)] and binodal lines (from the common tangent construction of f_{eff}) for (a) varying k_{cat} with $\Delta\mu = 8k_{\text{B}}T$ and (b) varying $\Delta\mu$ with $k_{\text{cat}}/k_{\text{spo}} = 1$. (c) Numerical simulations showing the evolution of a uniform steady state with $\phi_{\text{e}} = 0.15$ into two phase-separated regions. The circle, triangle and square identify the homogeneous steady state and the dense and dilute enzyme phases, respectively, and are plotted in all other panels for comparison. (d) Stability diagram of a mixture including a water component, for $\Delta\mu = 8k_{\text{B}}T$ and $k_{\text{cat}}/k_{\text{spo}} = 1$. The darker and lighter shaded regions mark the spinodal regions for $v_{\text{e}}/v_{\text{s}} = 20$ [also used in (a–c)] and $v_{\text{e}}/v_{\text{s}} = 85$, respectively. Additional system parameters in (a–d) are $\Delta\varepsilon = -5k_{\text{B}}T$, $D_{\text{pe}} = 4D_{\text{se}}$, and $D_{\text{ps}} = 10D_{\text{se}}$; in (d) $D_{\text{ew}} = D_{\text{sw}} = D_{\text{pw}} = 5D_{\text{se}}$ and $v_{\text{w}} = v_{\text{s}}$.

and so the system is unstable when

$$(\mathcal{K}_{\mathrm{w}}^{-1})_{1,1} = \frac{(\mathcal{K}_{\mathrm{w}})_{2,2}(\mathcal{K}_{\mathrm{w}})_{3,3} - (\mathcal{K}_{\mathrm{w}})_{2,3}(\mathcal{K}_{\mathrm{w}})_{3,2}}{\det(\mathcal{K}_{\mathrm{w}})} \geq 0. \tag{2.58}$$

The numerator of (2.58) is, to order $\boldsymbol{q}^2$,

$$\boldsymbol{q}^2 \left[- R_{\mathrm{p}} \frac{M^*_{\mathrm{se}} \frac{v_{\mathrm{e}}}{v_{\mathrm{s}}} + M^*_{\mathrm{ws}}}{\phi^*_{\mathrm{s}}} - R_{\mathrm{s}} \frac{M^*_{\mathrm{pe}} \frac{v_{\mathrm{e}}}{v_{\mathrm{s}}} + M^*_{\mathrm{wp}}}{\phi^*_{\mathrm{p}}} - \frac{v_{\mathrm{s}}}{v_{\mathrm{w}} \phi^*_{\mathrm{w}}} \Big(R_{\mathrm{s}} + R_{\mathrm{p}} \Big) \Big(M^*_{\mathrm{ws}} + M^*_{\mathrm{wp}} \Big) \right]. \tag{2.59}$$

With the common choice of mobilities, $M_{ij} < 0$ for $i \neq j$, and $R_i \geq 0$, the expression (2.59) is positive and the instability condition is simply

$$\det(\mathcal{K}_{\mathrm{w}}) > 0, \tag{2.60}$$

which marks the transition from having all negative eigenvalues to having two negative and one positive eigenvalue. The determinant of $\mathcal{K}_{\mathrm{w}}$ has many terms and even when truncated to order $\boldsymbol{q}^2$ it is not a manageable expression. Numerically evaluating this expression we find that in the low solvent limit ($\phi_{\mathrm{w}} \to 0$), and assuming the common form of the mobilities in (2.32), we recover the no-solvent case. Additionally, we find that the uniform steady-state can be unstable even when all the solute components (enzyme, substrate, and product) are in dilute conditions, as shown in Figure 2.5(d). This demonstrates the wide reach of this work and its potential application to realistic systems, where the components of the active minimal model may be part of a larger ensemble of molecules.

2.5.5 Enzymatic Autoregulation

A biologically pertinent question is what happens to the enzymatic activity when the system phase separates. The average rate of catalysis in a region of size L is given by $\bar{r}_{\mathrm{cat}} = \frac{1}{L} \int_0^L r_{\mathrm{cat}} \mathrm{d}x$ in a simple 1D case. In a homogeneous state, r_{cat} will be constant throughout the system and, using (2.34), we find that in the CIPS relevant regime ($\Delta\epsilon \ll 0$ and $\Delta\mu + \Delta\epsilon \gg 0$) the activity becomes $\bar{r}^{(h)}_{\mathrm{cat}} \propto \phi_{\mathrm{e}}(1 - (1 + k_{\mathrm{cat}}/k_{\mathrm{spo}})\phi_{\mathrm{e}}) + \mathcal{O}(\phi_{\mathrm{e}}^3)$ which is a concave function of ϕ_{e}. In a phase-separated state, $\bar{r}_{\mathrm{cat}}$ is a weighted average of the catalytic rates in each phase, with the weights determined by the lever rule. Due to the concavity of $r_{\mathrm{cat}}(\phi_{\mathrm{e}})$, we

find that the catalytic rate in the phase-separated state is always smaller than in the homogeneous state; $r_{\rm cat}(\alpha\phi_{\rm e}^{\rm I} + (1-\alpha)\phi_{\rm e}^{\rm II}) \geq \alpha r_{\rm cat}(\phi_{\rm e}^{\rm I}) + (1-\alpha) r_{\rm cat}(\phi_{\rm e}^{\rm II})$ shown graphically in figure 2.6(a) (here α is the fractional volume in each state with $0 \leq \alpha \leq 1$). We observe a similar behaviour when we vary a control parameter such as $\Delta\mu$, which is controlled by the concentration of the fuel molecules in an experiment; see figure 2.6(b). In the homogeneous phase, $\bar{r}_{\rm cat}$ initially rises and then saturates with increasing $\Delta\mu$. The phase separation reduces $\bar{r}_{\rm cat}$ in the whole system and leads to saturation at a lower activity. Through this mechanism, CIPS can act to autoregulate the enzymatic activity of the mixture: once the activity reaches a threshold, the system phase separates and gives rise to a reduced overall catalytic rate. A similar saturation effect is seen when other system parameters, such as $k_{\rm cat}$, are varied causing the system to phase separate.

2.6 Discussion

The minimal active model studied here provides a thermodynamically-consistent description of a multicomponent fluid and identifies a new, purely non-equilibrium mechanism for phase separation as a consequence of the catalytic, fuelled conversion between two components (substrate and product) by a third component (enzyme). Alongside the fuelled catalytic reaction, this catalysis-induced phase separation (CIPS) requires an asymmetry in the off diagonal mobility terms, which describe the strength of coupling between enzyme-substrate and enzyme-product thermodynamic forces and fluxes. An immediate question is therefore whether this asymmetry is present in real living systems, or, for synthetic systems, if it is hard to engineer this asymmetry.

At present, measurements of the off-diagonal Onsager mobilities for biologically relevant enzyme-substrate-product systems do not exist, however for a typical biological catalytic process, we expect both the spontaneous and catalysed reactions to be strongly driven, and the enzyme protein to be much larger than the small molecular substrate and product. Given that the kinetics of catalysed reactions are generally much faster than those of spontaneous ones (due to the reduced energy

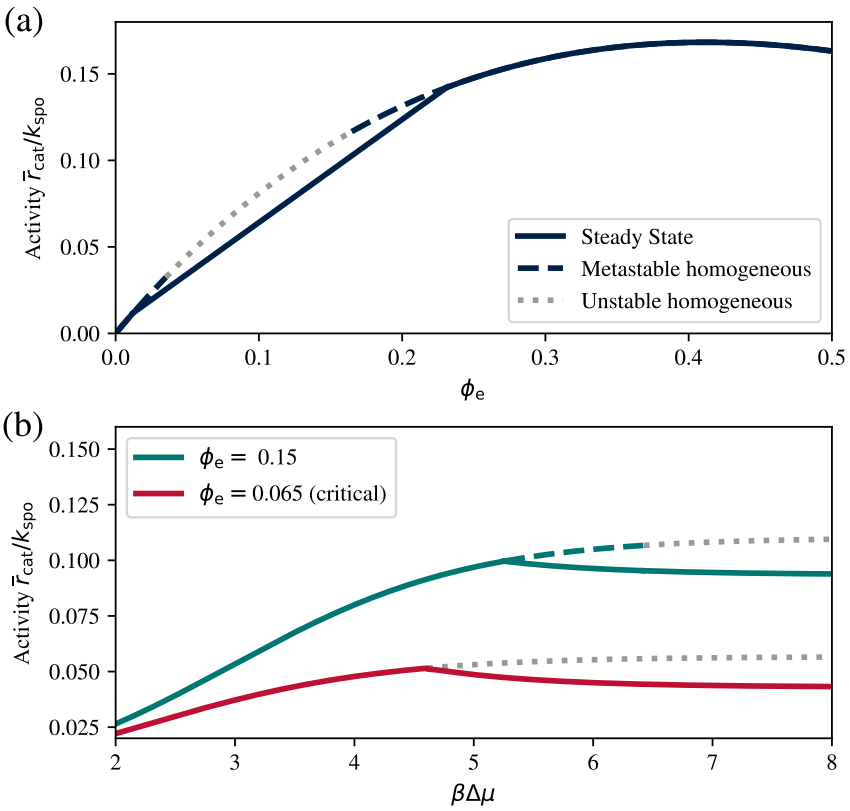

Figure 2.6: Effect of CIPS on catalytic activity. (a) Activity as a function of the initial ϕ_e. In the phase-separated state, the activity is a linear combination of the activity of the homogeneous states on either side of the binodal, which due to convexity is always smaller than that of the homogeneous state. (b) Evolution of activity with increasing $\Delta\mu$. As the system phase separates, the overall catalytic rate is reduced. When $\phi_e = 0.065$, the system passes through the critical point and there is no metastable homogeneous branch. System parameters are $\Delta\mu = 8k_BT$, $k_{cat}/k_{spo} = 1$, $\Delta\varepsilon = -5k_BT$, $D_{pe} = 4D_{se}$, and $D_{ps} = 10D_{se}$.

barrier, with $k_{cat} \gg k_{spo}$), this implies that the threshold mobility asymmetry required for CIPS can become vanishingly small. A priori, there is also no reason that the substrate and product will have symmetric response to gradients of the enzyme chemical potential and features of the molecular structure that may affect the coupling, such as shape or charge distribution will not be the same for different molecules. Existing experimental observations [46], [47] of unequal response of enzymes to gradients of substrate and product suggest that an asymmetry may generically exist between the enzyme-substrate and enzyme-product Onsager

mobilities. Furthermore, alternative descriptions of multicomponent diffusion, such as Fickian cross-diffusion [48] and Maxwell-Stefan diffusion [49] are equivalent to the Onsager framework and both molecular dynamics simulations and experimental measurements of these systems exhibit asymmetric responses [50], [51].

The mechanism behind CIPS is reminiscent of mechanisms for chemotactic or phoretic aggregation, where species move directly in response to gradients in other species [52], [53] and can cause active components to self organise, such as interacting microorganisms or catalytic colloids [25], [54]. However, these studies were based on microscopic descriptions of the chemotactic or phoretic response, typically valid only under dilute conditions, whereas using the framework developed here keeps all components on equal footing and is valid for systems at arbitrary densities. This is particularly relevant to lipid membrane systems with high lipid compositions that could act as components of the minimal model.

Due to the catalytic conversion, CIPS is fundamentally non-equilibrium and results in phase-separated states with non-vanishing fluxes, distinct from equilibrium mechanisms for phase separation. The latter rely on the presence of interaction terms (e.g. $\chi_{ij}\phi_i\phi_j$ and $\kappa_{ij}\boldsymbol{\nabla}\phi_i\cdot\boldsymbol{\nabla}\phi_j$) in the free energy density f_{FH}. Despite also requiring a size difference between components, CIPS is distinct from the entropic phase separation induced by depletion effects that is observed in binary hard-core mixtures [55], which results in equilibrium phase-separated states with vanishing fluxes. Future work may explore the competition or cooperation between equilibrium interactions and non-equilibrium catalytic effective interactions in phase separation. In particular, here we focused on effective interactions that are attractive, i.e. those with $(1-e^{-\beta\Delta\mu})(D_{\mathrm{pe}}-D_{\mathrm{se}})>0$ so that the right hand side of (2.49) is positive. One may also consider repulsive effective interactions, with $(1-e^{-\beta\Delta\mu})(D_{\mathrm{pe}}-D_{\mathrm{se}})<0$. In this case, we expect that an enzyme-rich condensate held together by equilibrium interactions may be *dissolved* by sufficiently strong non-equilibrium catalytic activity.

Another extension is to consider multi-step metabolic pathways, where the production of intermediate metabolites is known to regulate other reactions in the network and thus act as a feedback mechanism that inhibits overall metabolic

activity [56], [57]. CIPS provides a novel mechanism for this complex control of metabolism which, somewhat uniquely, autoregulates a single-step catalytic reaction and provides a simpler mechanism, potentially more amenable to fine-tuned synthetic control. A more complex reaction system with distinct enzymes, multiple species, or a different stoichiometry will change the regulatory effect of the phase separation. How this feedback could be used to control metabolic pathways is a relevant question. For example, CIPS may lead to colocalization of distinct enzymes within the same condensate, allowing for substrate channelling as in cellular metabolons [29], [58].

3

Membrane Mediated Elastic Interactions

Contents

3.1 Introduction 40
3.2 Background 43
3.2.1 Helfrich Hamiltonian 43
3.2.2 Monge Parameterisation 45
3.3 One Inclusion in an Elastic Membrane 47
3.3.1 Monopole and Quadrupole Modes 49
3.3.2 Dipole Mode 51
3.4 Multiple Inclusions in an Elastic Membrane 53
3.4.1 Calculating the Membrane Shape 54
3.4.2 Matching 56
3.4.3 Membrane Interaction Energy 62
3.4.4 Identical Inclusions 63
3.4.5 Features of the Two-Body Interaction Potential 63
3.5 Systems of Interacting Inclusions 65
3.6 Rings, Lines and Lattices 66
3.6.1 Rings 66
3.6.2 Lines 71
3.6.3 General Configurations 75
3.6.4 Configurations of Multiple Inclusions 79
3.7 Multi-Scale Model for Configurations 81
3.8 Biological Regimes 86
3.9 Discussion 88

3.1 Introduction

In addition to forming protein rich liquid droplets, many proteins are embedded in, and interact with, existing cellular structures. Biological membranes are abundant and are crucial to cellular and sub-cellular organisation. Membranes allow for the spatial and temporal management of reactions and the separation of substances and environments [59]. In addition to the familiar cellular membrane, eukaryotic cells also contain internal membranes that form the boundaries of organelles such as mitochondria, chloroplasts and lysosomes [60]. Biological membranes are sheet-like lipid bilayers that are two molecules thick (4-10nm) [3]. These are dynamic, fluid structures in which proteins float in a sea of lipids diffusing along the surface of the membrane, and different composition of these proteins and lipids can generate asymmetry across the membrane. In addition to compartmentalisation, biological membranes serve several additional functions necessary for life, such as energy storage and information transduction, and many of these are driven by the proteins associated with them [61].

Membranes are also a central focus in the development of novel biotechnology and biologically-inspired materials. For example, surrounding substances with lipid bilayer membranes can create small compartments called *liposomes* that can aid in drug delivery [62]. More recently, the development of DNA origami [63] has allowed for the engineering of sophisticated biomimetic systems of membranes that can control adsorption. These membranes are also candidates for controllable barriers, with engineered DNA nanopores displaying gating properties similar to natural ion channels switching between open and closed states depending on the transmembrane voltage [64]. Conventional engineered systems often rely on materials with specific properties at the atomic/molecular scale, but lack the hierarchical structure of interacting building blocks to enable macroscopic dynamic behaviour which is seen in biology [65]. Tunable and functional modules with active membranes may provide a scheme to develop these types of systems [66]. In addition to controlling the permeability of membranes, origami structures mimicking membrane-sculpting proteins have also been reported [67] and present the possibility

of controlling the shape of membrane bound compartments. Understanding more about the forces that govern the shaping and behaviour of membranes will therefore not only aid understanding of biophysical processes, but will also help devise new bioengineering systems.

The shape of membranes is also crucial to proper development and function. The endoplasmic reticulum (ER) and the Golgi apparatus have complex boundaries defined by the curvature of the internal membrane, but they have distinctly different shapes. Both structures have very large surface area for their volume, however the ER is more tubular compared to the more saccular Golgi apparatus [60]. This difference in structure may be related to the different functions of these organelles or be a consequence of the material within the organelle. Regardless, in order to understand the physical origin of these shapes, it is crucial to understand the interplay of the membrane with other biomolecules and structures and in particular the proteins embedded or tethered to the membrane. Membrane-bound proteins have been shown to be directly connected to membrane curvature and also to function, for example endocytosis being controlled by curvature inducing proteins that curve the membranes to form vesicles and allow the cell to take in external substances by engulfing the material [68].

Different mechanisms can control the changes in membrane shape. For example, transporter proteins can generate forces by moving material across the membrane, or the cytoskeletal structure can pull on the membrane [69]. These forces act to change the natural shape of the elastic membrane which has a bending stiffness and resists shape changes away from a rest configuration. Deformations in the membrane shape can also be caused by a variety of curvature-inducing inclusions, such as proteins that can bind to the membrane and insert structures that wedge the membrane and cause a bend [59], [70]. Two or more of these inclusions can then interact elastically, as the membrane responds to a curvature that is locally imposed by each inclusion as sketched in Figure 3.1. Since these proteins are also able to move within the fluid membrane, they will respond to forces pulling them together or pushing them apart to minimise the energy of the global deformation.

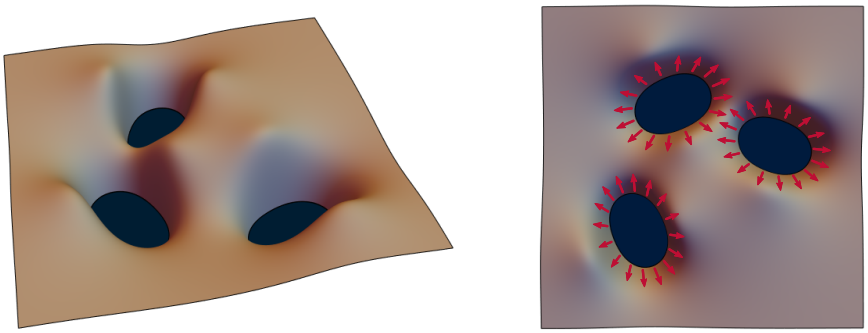

Figure 3.1: Example of three inclusions embedded in an elastic membrane and the resulting membrane shape from two different angles. The inclusions can interact via the elastic-mediated membrane forces (represented by the red arrows here).

The Bin/amphiphysin/Rvs (BAR) domain proteins are a common family of curvature-inducing membrane proteins that have a curved domain and induce curvature on the membrane by binding to it. The BAR domains consist of a protein dimer and are involved in many cellular processes. They can both sense the curvature of the membrane by preferential binding to regions with specific curvature [71] and also influence the membrane shape. Different BAR domains have different shapes and this can cause different deformations in the membrane. One common feature across the BAR domains is that they are not rotationally symmetric (viewed from the top as they lie on the membrane) and so the proteins impose more complex constraints on the membrane than simple bowl like deformations. This anisotropy is essential to the formation of membrane tubules, as symmetric deformations imposed by bowl-like proteins, such as clathrin, form spherical vesicles instead [59]. Thus, it is crucial to understand the elastic interactions between anisotropic proteins to gain insight into how membrane elasticity influences the cellular environment. Prior work has studied the role of elastic interactions between membrane bound curvature inducing inclusions [70], [72]–[74]. Different models assume different membrane tensions, inclusions separations and inclusion shape. One alternative to describing the distribution of individual interacting inclusions is to study the evolution of a density field that describes the distribution of curvature inducing inclusions on the

surface of the membrane. Continuum models [6] have been developed to study the stability of a uniform distribution of curvature inducing particles on a spherical vesicle. In addition to the elastic energy, the continuum framework is amenable to adding additional effects, such as the correlation of fluctuations, additional inclusion-inclusion interactions, out-of-equilibrium power input, and allows for the possibility of coupling the resulting deformations to the actomyosin cortex or other important cellular structures/processes [69], [75]. Growing instabilities in the distribution of curvature inducing inclusions may act to co-localise membrane proteins and to drive large scale shape changes in the cell [76].

However these top-down density field models do not specify any details of the mechanisms behind these interactions. This would be useful to know, to investigate specific regions of parameter space that correspond to the parameters observed in vivo. Understanding the mapping from individual particle properties to the parameters in the density description would present a new way to measure these small scale properties, provide alternative verification of current measurement techniques, or highlight broken symmetries from anisotropic curvature inducing inclusions. At very high densities of inclusions, interactions preventing inclusions from overlapping can drive the formation of a nematic phase [77]. However, at lower densities, when the separation between these inclusions is large, the elastic interaction is less intuitive and the role of tension that resists deformations further complicates the interactions. This is the situation we study here: a system of interacting inclusions embedded in a fluid membrane with tension that are well separated. This study is initially motivated by biological observations. However the results and methods are more general and they can provide mechanisms for the control of interactions of synthetic membranes and the formation of structures from individual inclusions.

3.2 Background

3.2.1 Helfrich Hamiltonian

A common approach to describe the response to loads applied to an elastic sheet that is fluid along its surface is to use a Hamiltonian describing the energy of

the membrane. In this case, the strain energy of the system is only associated to curvature effects [78]. The traditional setting for this type of model is the so-called Helfrich Hamiltonian that gives the strain energy for a particular membrane geometry, described by the mean curvature H and Gaussian curvature K_G [72], [79]. Additionally, to model the observation that the two monolayers in biological membranes can have different lipid composition inducing a non-flat initial geometry, we include a non-zero intrinsic mean curvature, labelled H_0.

Therefore, we model the lipid bilayer as a surface Ω endowed with an elastic energy E that only depends on the curvature:

$$E = \int_\Omega \underbrace{\frac{\kappa}{2}(H - H_0)^2 + \overline{\kappa} K_G + T}_{\text{Helfrich Hamiltonian}} \, \mathrm{d}A \tag{3.1}$$

where κ is the bending stiffness, $\overline{\kappa}$ is the saddle-splay modulus, T is the tension and the integral is taken over the entire membrane, Ω [80].

In this work, we consider Ω with fixed topology and with constant surface normal direction at the boundary of any inclusions. Therefore, the Gauss-Bonnet theorem ensures that the contribution from the Gaussian curvature, K_G, only contributes to a constant in the energy and thus does not affect the subsequent physics [78], unless there is a change in the membrane topology. Note that the Gauss-Bonnet theorem also includes a contribution from the integral of the geodesic curvature of the membrane along the membrane boundary. This contribution needs to be evaluated at infinity and around each inclusion. Infinitely far away from the inclusions the membrane returns to being flat and so this contribution is constant. In this work we only consider rigid inclusions that impose a fixed contact angle (that can vary along the edge of the inclusion). The rigid inclusions define the path of the boundary and, together with the fixed contact angle, also determine the normal vector to the membrane surface at the inclusion edge. These two quantities determine the geodesic curvature of the membrane along the edge of the inclusion. The geodesic curvature does not depend on other features of the membrane shape or the orientation of the inclusion. Since this contribution is also constant, we do not need to consider the Gaussian curvature in the minimisation.

3.2.2 Monge Parameterisation

Cell membranes are much larger than curvature inducing inclusions (often these inclusions are simply proteins). In particular, the giant vesicles used in many experiments on the physics of membranes are around 20 µm in size [81], but many times larger than the 22 nm diameter of the abundant curvature inducing Bin/amphiphysin/Rvs (BAR) domain [71]. At the scale of the protein we therefore expect membranes to appear locally as planes ($H_0 = 0$) with small regions of curvature induced by inclusions. As the proteins interact and potentially accumulate, or other cellular mechanisms force the membrane to curve this approximation may break down, but the assumption of a flat membrane provides a useful regime to explore the onset of these effects and allows us to use the Monge parameterisation to describe the surface [78].

The Monge parameterisation describes every point on a membrane as having some height above a reference plane. We non-dimensionalise the position and height of the membrane by an arbitrary length, L, so at any point on the plane $\mathbf{r} = (Lx, Ly)$ the membrane is at height $\xi L h(\mathbf{r})$, where x and y are non-dimensional positional coordinates in the reference plane. Since we expect deformations to be small, we have introduced a small non-dimensional parameter, $\xi \ll 1$, that rescales the non-dimensional height, so that h is $\mathcal{O}(1)$. This parameterisation describes surfaces that have small deformations and no overhangs and allows us to write the mean curvature of the membrane, H, in terms of $h(\mathbf{r})$ to give

$$H = \nabla_L \cdot \left(\frac{\nabla_L \xi h(\mathbf{r})}{\sqrt{1 + (\nabla_L \xi h(\mathbf{r}))^2)}} \right) = \frac{1}{L} \nabla \cdot \left(\frac{\nabla \xi h(\mathbf{r})}{\sqrt{1 + (\nabla \xi h(\mathbf{r}))^2)}} \right) = \frac{\xi}{L} \nabla^2 h(\mathbf{r}) + \mathcal{O}(\xi^2), \tag{3.2}$$

where the approximation is valid for $\xi |\nabla h| \ll 1$ and we have used ∇_L to define gradients in the dimensional coordinates and ∇ to define the gradients in the non-dimensional coordinates, x and y. The area element is not simply given by $\mathrm{d}A = L^2 \mathrm{d}x\mathrm{d}y$, but instead:

$$\mathrm{d}A = (1 + L^2 \xi^2 |\nabla_L h|^2/2 + \mathcal{O}(\xi^4)) \mathrm{d}(Lx) \mathrm{d}(Ly) = (1 + \xi^2 |\nabla h|^2/2 + \mathcal{O}(\xi^4)) L^2 \mathrm{d}x\mathrm{d}y. \tag{3.3}$$

In the zero-temperature limit, the physical membrane will minimise the energy, E, in (3.1), which in this parameterisation is

$$E = TA_0 + \xi^2 \int_\Omega \left[\frac{\kappa}{2} (\nabla^2 h)^2 + \frac{TL^2}{2} |\nabla h|^2 \right] \mathrm{d}x\mathrm{d}y + \mathcal{O}(\xi^3), \tag{3.4}$$

where A_0 is the area of the flat membrane and $\mu = \sqrt{\kappa/(TL^2)}$, is a typical non-dimensional length scale for the problem. We write this energy as

$$E = TA_0 + \kappa \xi^2 \bar{E} \tag{3.5}$$

where the non-dimensional energy, $\bar{E}$, is

$$\bar{E} = \frac{1}{2} \int_\Omega \Big((\nabla^2 h)^2 + \mu^{-2} |\nabla h|^2 \Big) \mathrm{d}x\mathrm{d}y + \mathcal{O}(\xi^3). \tag{3.6}$$

The shape of a physical membrane acts to minimise this energy. Considering a variation in $h(\mathbf{r})$, i.e. $h(\mathbf{r}) \to h(\mathbf{r}) + \delta h(\mathbf{r})$, the scaled energy becomes to first order in δh

$$\begin{aligned} \bar{E}[h(\mathbf{r}) + \delta h(\mathbf{r})] = \bar{E}[h(\mathbf{r})] &+ \int \delta h (\nabla^4 h - \mu^{-2} \nabla^2 h) \mathrm{d}A \\ &+ \oint \Big(\nabla \delta h \nabla^2 h - \delta h \nabla^3 h + \mu^{-2} \delta h \nabla h \Big) \cdot \mathbf{n} \mathrm{d}s = 0, \end{aligned} \tag{3.7}$$

for a membrane with no spontaneous curvature ($H_0 = 0$). Therefore (3.4) is minimised when the membrane satisfies the so-called *shape equation*:

$$\nabla^4 h - \mu^{-2} \nabla^2 h = 0. \tag{3.8}$$

Additionally the boundary terms vanish when the energy is extremal, which imposes two further constraints on the boundary of the membrane. Firstly, the minimisation requires

$$\oint \Big(\nabla \delta h \nabla^2 h \Big) \cdot \mathbf{n} \mathrm{d}s = 0, \tag{3.9}$$

which is solved by either fixing the derivative of h perpendicular to the boundary, that is $\mathbf{n} \cdot \nabla \delta h = 0$, or by setting $\nabla^2 h = 0$. Secondly, the minimisation requires

$$\oint \Big(-\delta h \nabla^3 h + \mu^{-2} \delta h \nabla h \Big) \cdot \mathbf{n} \mathrm{d}s = 0, \tag{3.10}$$

which is solved by either fixing the value of h on the boundary, $\delta h = 0$, or by $(\nabla^3 h + \mu^{-2}\nabla h) \cdot \mathbf{n} = 0$.

Bending and deformations of the membrane are imposed by boundary conditions on h. For example the edge of a curvature-inducing inclusion will introduce an interior boundary with associated boundary conditions. In the bulk, the membrane then satisfies the shape equation subject to these constraints, and infinitely far away from the inclusion, the membrane returns to being flat. The perturbed membrane returns to being flat more slowly when tension is lower compared to the bending stiffness, and the membrane becomes flat more quickly in higher tension systems.

3.3 One Inclusion in an Elastic Membrane

We begin by considering a single circular inclusion of non-dimensional radius ϵ in an elastic sheet. The inclusion imposes a contact angle at its edge, and thus will induce a shape deformation in a flat membrane as shown in Figure 3.2. The membrane will respond elastically and will adopt an equilibrium shape that minimises the energy subject to the imposed contact angle. The inclusion can arbitrarily tilt and move vertically to minimise the energy. We calculate this minimising shape in a non-dimensional polar coordinate system, (r, ϕ), with origin at the centre of the inclusion so that the boundary of the inclusion is given by $r = \epsilon$.

In the bulk of the membrane, the scaled height, h, follows the shape equation, (3.8). Far away from the inclusion, we impose the that the elastic sheet returns to the flat rest shape, so that

$$\left.\frac{\partial h}{\partial r}\right|_{r\to\infty} = 0. \tag{3.11}$$

Additionally, the membrane shape is constrained by the contact angle $\tilde{\alpha}(\phi)$, which defines the slope of h at the edge of the inclusion relative to the plane of the inclusion. Here, the curvature-inducing inclusions are modelled as circular, however varying the contact angle around the edge of the inclusion gives the inclusions an orientation. The varying contact angle therefore induces an anisotropic response of the membrane

and so the membrane response will depend on the inclusion orientation, as is expected for many biophysical structures that break the radial symmetry.

Since the contact angle is periodic around the edge of the inclusion and assumed to be continuous, it can be expanded in Fourier modes as

$$\tilde{\alpha}(\phi) = \sum_{m=0}^{\infty} \tilde{\alpha}^{(m)} \cos(m\phi + \nu_m). \tag{3.12}$$

We expect the lower-order modes to induce the largest deformations and capture the distinct behaviours of curvature-inducing inclusions. As such, we consider the first three modes of the expansion of the contact angle, when $m = 0, 1, 2$, which we refer to as the *monopole*, the *dipole* and the *quadrupole* modes, respectively.

The dipole mode contributes to the contact angle with a positive contribution on one half of the inclusion and a negative contribution on the other half and consequently generates a tilt in posture of the inclusion at equilibrium.

The quadrupole and monopole modes do not generate tilt, as the sign of the contact angle is symmetric about the diameters of the inclusion.

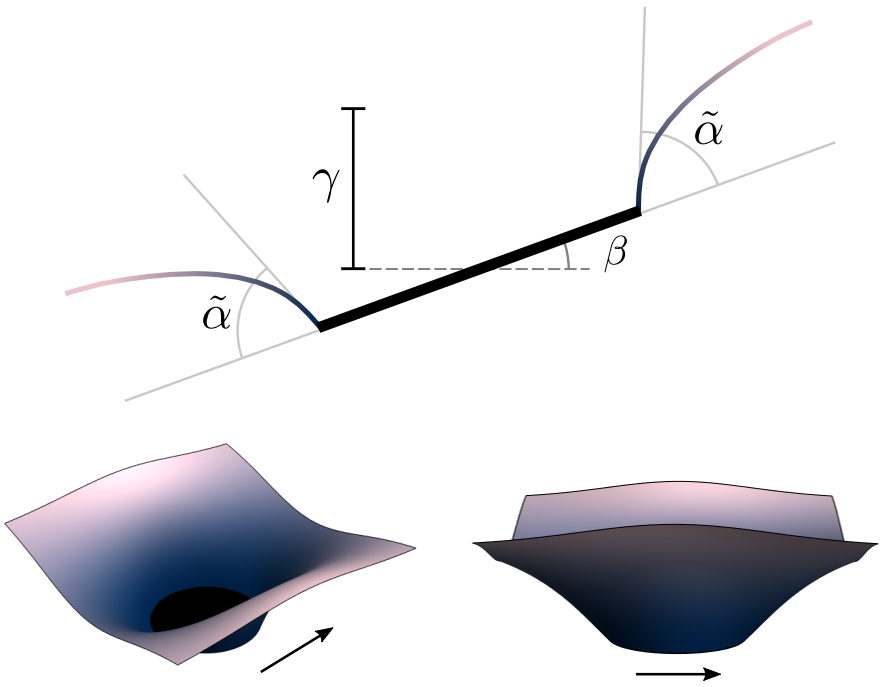

Figure 3.2: Contact angle induced by a circular inclusion. The top scheme shows a cross section of the inclusion. The bottom two surface plots show the membrane response locally to an anisotropic inclusion, where the arrow indicates the orientation.

3.3.1 Monopole and Quadrupole Modes

The lowest order modes that do not induce a tilt for a single inclusion are the monopole and quadrupole modes, where the quadrupole mode breaks the radial symmetry and gives each inclusion an orientation. The monopole and quadrupole modes have strength $\tilde{\alpha}^{(0)}$ and $\tilde{\alpha}^{(2)}$ respectively so that the contact angle is

$$\tilde{\alpha}(\phi) = \tilde{\alpha}^{(0)} + \tilde{\alpha}^{(2)} \cos(2\phi), \tag{3.13}$$

as we can choose to set $\nu_0 = \nu_2 = 0$ without loss of generality (this amounts to choosing the orientation of the inclusion in the membrane). Despite not inducing a tilt, the monopole gives the inclusion a clear up and down orientation (a bowl looks different holding soup $\cup$ or trapping a spider $\cap$, face up or down) and so compared to the far-field flat membrane, we expect the inclusion to be positioned at some non-zero height, γ, that will be up or down from the initial plane depending on $\tilde{\alpha}^{(0)}$. The boundary conditions for the membrane around the inclusion are therefore

$$\begin{aligned} \left.\frac{\partial h}{\partial r}\right|_{r=\epsilon} &= \tilde{\alpha}^{(0)} + \tilde{\alpha}^{(2)} \cos(2\phi) + \beta \cos\phi \\ \left. h \right|_{r=\epsilon} &= \gamma + \epsilon\beta \cos\phi, \end{aligned} \tag{3.14}$$

where γ is to be determined by force balance on the edge of the inclusion, equivalent to (3.9) and (3.10). The force balance also gives $\beta = 0$, as the monopole and quadrupole do not induce a tilt (Section 3.3.2 considers the tilt inducing the dipole mode).

The general solution in the bulk to the shape equation with a monopole and quadrupole is

$$\begin{aligned} h(r,\phi) = A_1 + A_2 \log(r) + A_3 I_0(r/\mu) + A_4 K_0(r/\mu) \\ + \cos(2\phi)\left(A_5 r^2 + \frac{A_6}{r^2} + A_7 I_2(r/\mu) + A_8 K_2(r/\mu)\right), \end{aligned} \tag{3.15}$$

where I_ν and K_ν are modified Bessel functions of the first and second kind respectively. However, since the membrane is assumed to be flat as $r \to \infty$ we find $A_3 = A_5 = A_7 = 0$. At the boundary of the inclusion, the normal derivative

is fixed by the contact angle. Since the inclusion is rigid and not tilted $\delta h(\phi)$ is constant and the force balance in (3.10) becomes

$$\int_0^{2\pi} \epsilon \frac{\partial}{\partial \mathbf{n}} \left(\nabla^2 h - \mu^{-2} h \right) \mathrm{d}\phi = 0. \tag{3.16}$$

Evaluating the integral for the membrane gives $A_2 = 0$ and we choose, without loss of generality, the far-field membrane height to vanish so that $A_1 = 0$. The remaining terms must satisfy the boundary conditions from the imposed contact angle and inclusion shape, which are satisfied when

$$A_4 = -\frac{\tilde{\alpha}^{(0)}\mu}{K_1(\epsilon/\mu)}, \quad A_6 = \frac{\tilde{\alpha}^{(2)}\epsilon^2 \mu K_2(\epsilon/\mu)}{K_1(\epsilon/\mu)}, \quad A_8 = -\frac{\tilde{\alpha}^{(2)}\mu}{K_1(\epsilon/\mu)}. \tag{3.17}$$

Therefore, the membrane shape that satisfies the boundary conditions is

$$h(r,\phi) = -\frac{\tilde{\alpha}^{(0)}\mu}{K_1(\epsilon/\mu)} K_0(r/\mu) + \cos(2\phi) \left(\frac{\tilde{\alpha}^{(2)}\epsilon^2 \mu K_2(\epsilon/\mu)}{K_1(\epsilon/\mu)} r^{-2} - \frac{\tilde{\alpha}^{(2)}\mu}{K_1(\epsilon/\mu)} K_2(r/\mu) \right) \tag{3.18}$$

and using (3.14) gives the inclusion height

$$\gamma = -\tilde{\alpha}^{(0)} \frac{\mu K_0(\epsilon/\mu)}{K_1(\epsilon/\mu)}, \tag{3.19}$$

which does not depend on the quadrupole mode as expected. The energy of the membrane can now be found by evaluating the energy functional (3.4) using the solution in (3.18). A convenient way to calculate this integral is to integrate by parts, and evaluate the boundary terms. Using the identity

$$\int_\Omega \left((\nabla^2 h)^2 + \mu^{-2} |\nabla h|^2 \right) \mathrm{d}x\mathrm{d}y = \int_{\partial\Omega} \left(\nabla^2 h \frac{\partial h}{\partial \mathbf{n}} - h \frac{\partial}{\partial \mathbf{n}} (\nabla^2 h) + \mu^{-2} h \frac{\partial h}{\partial \mathbf{n}} \right) \mathrm{d}s, \tag{3.20}$$

and the condition that the membrane is flat far away from the inclusion gives the energy of the membrane to be

$$\bar{E} = -\frac{1}{2} \int_0^{2\pi} \epsilon \left(\nabla^2 h \frac{\partial h}{\partial r} - h \frac{\partial}{\partial r} (\nabla^2 h) + \mu^{-2} h \frac{\partial h}{\partial r} \right) \mathrm{d}\phi \tag{3.21}$$

where the integral is evaluated at $r = \epsilon$. Evaluating this energy on (3.18) gives

$$\bar{E} = \left(\tilde{\alpha}^{(0)} \right)^2 \frac{\pi\epsilon}{\mu} \frac{K_0(\epsilon/\mu)}{K_1(\epsilon/\mu)} + \left(\tilde{\alpha}^{(2)} \right)^2 \frac{\pi}{8\epsilon^2\mu} \left[9\epsilon^2\mu + 16\mu^3 + \frac{4\epsilon\left(\epsilon^2 + 2\mu^2\right) K_0(\epsilon/\mu)}{K_1(\epsilon/\mu)} + \frac{16\mu^3 K_2(\epsilon/\mu)^2 - \epsilon^2 \mu K_3(\epsilon/\mu)^2}{K_1(\epsilon/\mu)^2} \right]. \tag{3.22}$$

This result is valid for one inclusion in an elastic membrane with small deformations. However, for the small inclusions that induce membrane curvature the length scale of the system L (such that $\mu \sim O(1)$) will be much larger than the radius of the inclusion so that $\epsilon \ll 1$. The limiting behaviour of the modified Bessel functions for small arguments is $K_0(x) \sim -\ln(x/2) - \gamma_{\mathrm{EM}}$, where γ_{EM} is the Euler–Mascheroni constant and for $n > 0$ then $K_n(x) \sim (2/x)^n \Gamma(n)/2$. The energy of the deformation to fourth order then further simplifies to

$$\bar{E} = \pi \left(\tilde{\alpha}^{(2)}\right)^2 - \left(\left(\tilde{\alpha}^{(0)}\right)^2 + \frac{\left(\tilde{\alpha}^{(2)}\right)^2}{2} \right) \frac{\pi \epsilon^2}{\mu^2} \left(\gamma_{\mathrm{EM}} + \ln(\epsilon/2\mu)\right) + \mathcal{O}(\epsilon^4). \tag{3.23}$$

The form of the energy has two terms, corresponding to the radial and azimuthal curvatures at the boundary of the inclusion.

3.3.2 Dipole Mode

We now consider an inclusion that imposes a contact angle with a dipole mode that is proportional to $\cos\phi$. When embedded in an elastic membrane, the inclusion will tilt to directly oppose the deformation of the membrane that the dipole boundary condition generates. This tilt alters the slope of the membrane at the inclusion edge (as the contact angle is measured relative to the tilted inclusion) and also changes the footprint of the inclusion, which will now appear as an ellipse in the xy plane, making the shape equation hard to solve with the elliptical internal boundary. However since we consider small deformations, $\xi|\nabla h| \ll 1$, any tilt of the inclusion will also be small. Without loss of generality, we consider tilts along the y-axis and define the angle that the tilted inclusion makes with the reference plane as $\xi\beta$, where β is $\mathcal{O}(1)$ as shown in Figure 3.2. The boundary of the inclusion is the solution to

$$y^2 + \frac{x^2}{\cos(\xi\beta)} \approx y^2 + x^2(1 + \xi^2\beta^2) = \epsilon^2 \tag{3.24}$$

which is unchanged to first order in ξ. The tilt will also change the height and gradient of the membrane at the boundary edge. The boundary conditions are

$$h\Big|_{\partial\Omega} = \epsilon\beta\cos\phi, \tag{3.25}$$

$$\frac{\partial h}{\partial r}\Big|_{\partial\Omega} = \left(\tilde{\alpha}^{(1)} + \beta\right)\cos(\phi), \tag{3.26}$$

as well as the membrane returning to being flat far away from the inclusion. The general solution with the dipole mode is

$$h(r,\phi) = \left(A_1 r + \frac{A_2}{r} + A_3 K_1(r/\mu) + A_4 I_1(r/\mu)\right)\cos\phi. \tag{3.27}$$

Following the same steps as before, the solution that satisfies the boundary conditions is

$$h(r,\phi) = \left(-\frac{\left(\tilde{\alpha}^{(1)} + 2\beta\right)\mu}{K_0(\epsilon/\mu)}K_1(\epsilon/\mu) + \frac{\epsilon}{r}\left(\epsilon\beta + \frac{\left(\tilde{\alpha}^{(1)} + 2\beta\right)K_1(\epsilon/\mu)}{K_0(\epsilon/\mu)}\right)\right)\cos\phi. \tag{3.28}$$

Additionally, we need to solve for the tilt that minimises the membrane energy, which is equivalent to the zero-torque configuration which we can find from the boundary terms in (3.7). As the inclusion is rigid, the variations on the boundary and variation in the derivative are connected to variations of the tilt, $\delta\beta$. The geometry gives

$$\nabla\delta h\cdot\mathbf{n} = -\delta\beta\cos\phi \qquad \text{and} \qquad \delta h = \epsilon\delta\beta\cos\phi, \tag{3.29}$$

so that the torque balance becomes

$$\nabla^2 h - \epsilon\frac{\partial}{\partial r}\left(\nabla^2 h - \mu^{-2}h\right)\Big|_{\partial\Omega} = 0 \tag{3.30}$$

which is solved by

$$\beta = -\frac{2\tilde{\alpha}^{(1)}\mu K_1(\epsilon/\mu)}{\epsilon K_0(\epsilon/\mu) + 4\mu K_1(\epsilon/\mu)}. \tag{3.31}$$

The energy of the membrane is

$$\begin{aligned}\bar{E} = \frac{\pi\left(\tilde{\alpha}^{(1)}\right)^2}{8\mu\left(\epsilon K_0(\epsilon/\mu) + 4\mu K_1(\epsilon/\mu)\right)^2}\Big[&4\left(4\epsilon^2\mu + \mu^3\right)K_1(\epsilon/\mu)^2 \\ &+ 4\epsilon\left(\epsilon^2 + \mu^2\right)K_1(\epsilon/\mu)K_0(\epsilon/\mu) + \epsilon^2\mu K_0(\epsilon/\mu)^2 - \epsilon^2\mu K_2(\epsilon/\mu)^2\Big].\end{aligned} \tag{3.32}$$

We consider again the limit of small inclusions, $\epsilon \ll 1$, and expand the energy to obtain

$$\bar{E} = \frac{\pi \left(\tilde{\alpha}^{(1)}\right)^2 \epsilon^2}{8\mu^2} + \frac{\pi \left(\tilde{\alpha}^{(1)}\right)^2 \left(\ln(\epsilon/2\mu) + \gamma_{\mathrm{EM}}\right) \epsilon^4}{32\mu^4} + O\left(\epsilon^5\right). \tag{3.33}$$

Comparing this energy to the energy in (3.23) obtained for the monopole and quadrupole, we can observe that each term of the dipole contribution can be found in the monopole and quadrupole energy, but the dipole contribution always appears at a higher order in ϵ. Hence, the dipole energy can be seen as a higher-order correction of the monopole/quadrupole energy. In similar work [80] the dipole mode was shown not to affect the interactions between small inclusions as the inclusions could simply tilt to balance the forces from the dipole. Therefore, we do not consider this mode in deriving the elastic interaction between inclusions and we will not consider dipole effects further.

3.4 Multiple Inclusions in an Elastic Membrane

When multiple inclusions are embedded in an elastic membrane, the resulting deformation field can be calculated in the same way as for a single inclusion. Each inclusion will constrain the value of the membrane height and its derivatives on an interior boundary defined by the inclusion edge. Away from the inclusions the membrane returns to being flat. In general it is not possible to solve exactly for the shape of the membrane for an arbitrary configuration of inclusions. However, the small size of the inclusions can be exploited to find an asymptotic solution for the membrane shape.

The inclusions are assumed to be much smaller than the distance between inclusions. We set L as the typical inclusion separation and the non-dimensional inclusion radius is ϵ. We will consider the case where $\epsilon \ll 1$ where μ remains $\mathcal{O}(1)$ as $\epsilon \to 0$. The deformation field around each inclusion will be dominated by the constraints from the contact angle of that specific inclusion. This defines an *inner* region around each inclusion which is of size $\mathcal{O}(\epsilon)$. When viewing the system on length scales comparable to the separation of inclusions, the membrane shape

will be determined by all inclusions and this defines the *outer* region, as shown in Figure 3.3. Studying the shape of the membrane in both regions and using matched asymptotic analysis give a perturbation series for the deformation field everywhere in response to the presence of all inclusions and so the interaction energy of the deformation due to the position and orientation of each inclusion can be calculated.

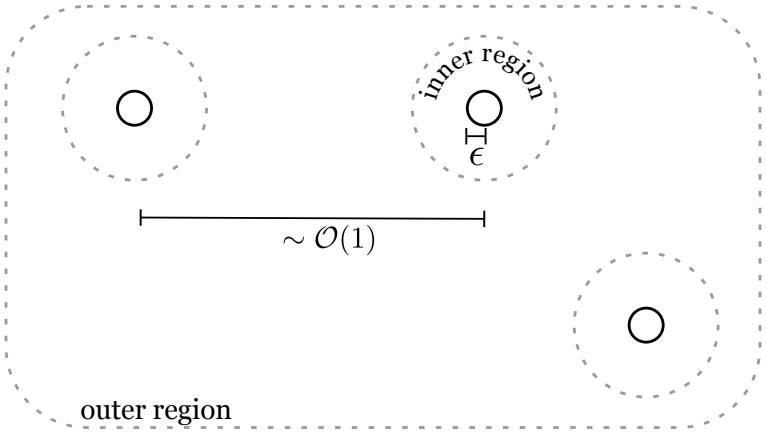

Figure 3.3: Summary of the inner and outer regions for the problem of multiple, small inclusions interacting through the membrane. There is an inner region around each inclusion.

3.4.1 Calculating the Membrane Shape

We begin by considering a system containing N inclusions, each of which we model as a circular disc. The i^{th} inclusion has contact angle $\tilde{\alpha}_i$ and its centre at (x_i, y_i) and we define the anticlockwise bearing and distance between the i^{th} and j^{th} inclusion to be θ_{ij} and R_{ij}, respectively. The anisotropic inclusions also have an orientation and so we define ψ_i as rotation of the inclusion i measured from the x-axis. The typical separation between inclusions defines the length scale, L, used to non-dimensionalise this problem. This geometry and setup is shown in Figure 3.4. The inclusion has a posture described by the height of the centre γ_i and two angles β_{i1} and β_{i2} that describe the tilt about the y- and x-axis, respectively. Even if the contact angle has no tilt inducing Fourier mode, the location of other inclusions could break the symmetry and generate tilts. Therefore on the boundary of the i^{th} inclusion

$$h\Big|_{\partial D_i} = \gamma_i + \beta_{i1}(x - x_i) + \beta_{i2}(y - y_i), \tag{3.34}$$

similarly to the setup in (3.25). Again since we expect small deformations, the boundary will be unchanged to first order in ξ. The contact angle imposes

$$\left.\frac{\partial h}{\partial \hat{\mathbf{n}}_i}\right|_{\partial D_i} = \tilde{\alpha}_i(x,y) + \beta_{i1}\frac{\partial x}{\partial \hat{\mathbf{n}}_i} + \beta_{i2}\frac{\partial y}{\partial \hat{\mathbf{n}}_i}, \tag{3.35}$$

where $\hat{\mathbf{n}}_i$ is the normal to the boundary in the xy-plane. When $\epsilon \ll 1$, the height displacement of the inclusion is given by (3.19):

$$\gamma = \epsilon\tilde{\alpha}^{(0)}(\gamma_{\mathrm{EM}} + \ln(\epsilon/2\mu)) + \mathcal{O}(\epsilon^2). \tag{3.36}$$

To keep the typical displacements as $\mathcal{O}(1)$ we set $\tilde{\alpha}(\phi) = \epsilon^{-1}\alpha(\phi)$ where $\alpha_i(\phi) \sim \mathcal{O}(1)$. We include a monopole and quadrupole mode due to the contact angle so that

$$\alpha_i(\phi) = \alpha_i^{(0)} + \alpha_i^{(2)}\cos(2\phi). \tag{3.37}$$

The anisotropy of the inclusion is defined as $\omega_i = \alpha_i^{(2)}/\alpha_i^{(0)}$ and we will consider the distinguished limit of strong anisotropy and strong tension: $\omega_i = \mathcal{O}(1)$ and $\mu = \mathcal{O}(1)$ as $\epsilon \to 0$. In this regime the interactions between well separated inclusions are tension dominated.

Around each inclusion we define an inner coordinate system. The centre of each inclusion, (x_i, y_i), is the origin for a set of local polar coordinates, (ρ_i, ϕ_i) where ϕ_i is measured from the x-axis. The inner radial coordinate is scaled by the inclusion radius, ϵ, to give

$$x - x_i = \epsilon\rho_i\cos\phi_i, \tag{3.38}$$

$$y - y_i = \epsilon\rho_i\sin\phi_i, \tag{3.39}$$

so that the inclusion is a disc of radius 1. The membrane height in the inner region around the i^{th} inclusion is $h_i(\rho_i, \phi_i)$.

We expand the membrane height and the parameters describing the posture of the inclusion in the system in integer powers of ϵ, for example, $h_i = h_i^{(0)} + \epsilon h_i^{(1)} + \epsilon^2 h_i^{(2)} + \cdots$ and $\beta_{i1} = \beta_{i1}^{(0)} + \epsilon\beta_{i1}^{(1)} + \epsilon^2\beta_{i1}^{(2)} + \cdots$. In the inner coordinates, the shape equation (3.8) becomes

$$\nabla_i^4 h_i - \epsilon^2\mu^{-2}\nabla_i^2 h_i = 0, \tag{3.40}$$

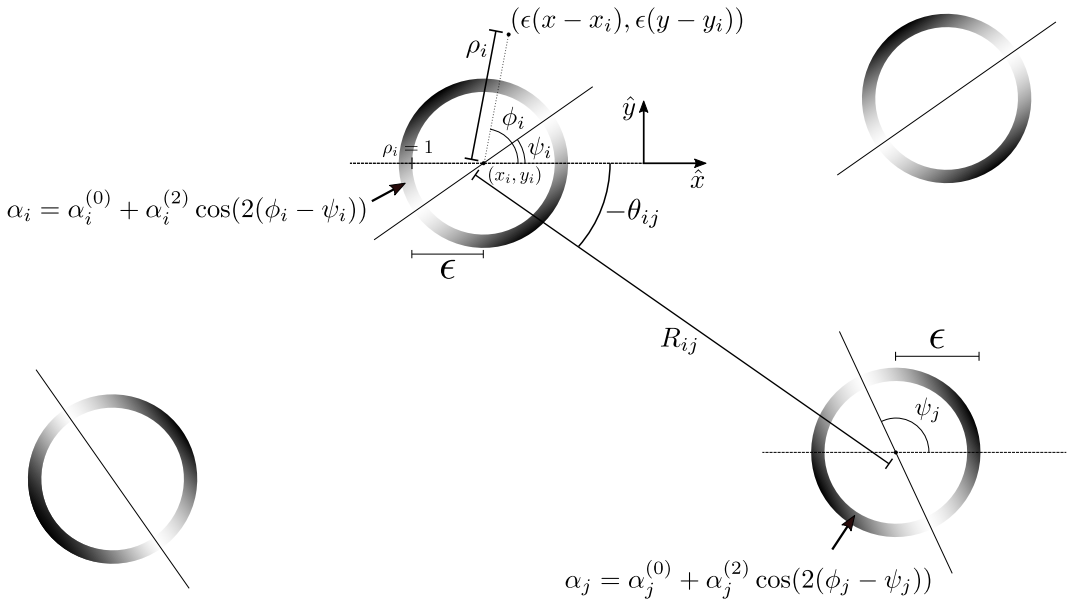

Figure 3.4: Parameterisation of the membrane elastic problem. The example shows the distribution of four inclusions where the inner coordinate system around the ith inclusions is shown and the parameters describing the relative location of the jth inclusion are also shown. All angles are measured clockwise from the x-axis.

where the subscript on the gradient operator indicates the inner coordinate system around the i^{th} inclusion. This equation, along with the inclusion boundary conditions and the force balance, must be satisfied at every order. The membrane shape in the outer region is given by $h_{\text{o}}(x, y)$, which we also expand in powers of ϵ, and the inclusions appear as point singularities as $\epsilon \to 0$.

3.4.2 Matching

At leading order the inner solution must satisfy

$$\nabla_i^4 h_i^{(0)} = 0, \tag{3.41}$$

$$h_i^{(0)}\Big|_{\rho_i=1} = \gamma_i^{(0)}, \tag{3.42}$$

$$\frac{\partial h_i^{(0)}}{\partial \rho_i}\bigg|_{\rho_i=1} = \alpha_i^{(0)} + \alpha_i^{(2)} \cos(2\phi_i - 2\psi_i). \tag{3.43}$$

Note that there is no inclusion tilt at this order. In polar coordinates the biharmonic equation can be solved by separation of variables to obtain the so called Michell solution. The boundary conditions only allow solutions with the monopole and

quadrupole angular dependence, giving

$$h_i^{(0)} = \gamma_i^{(0)} + \alpha_i^{(0)} \log \rho_i + \frac{\alpha_i^{(2)}}{2}\left(1 - \frac{1}{\rho_i^2}\right)\cos(2\psi_i - 2\phi). \tag{3.44}$$

In the outer region, the shape equation for h_o is the same at every order:

$$\nabla^4 h_\mathrm{o}^{(k)} - \mu^{-2}\nabla^2 h_\mathrm{o}^{(k)} = 0, \qquad k = 0, 1, \ldots \tag{3.45}$$

Around each inclusion the membrane approaches a singularity, which must match with the inner solution, and far away from all inclusions, the membrane returns to being flat. The solution that matches and decays at infinity is given by

$$h_\mathrm{o}^{(0)} = c_0 + \sum_i \left(c_{1i} K_0(r_i/\mu) + c_{2i}\cos(2\phi_i - 2\psi_i)\left(\frac{4\mu^2}{r_i^2} - 2K_2(r_i/\mu)\right)\right), \tag{3.46}$$

where $r_i = ((x - x_i)^2 + (y - y_i)^2)^{1/2}$ and $\phi_i = \tan^{-1}((y - y_i)/(x - x_i))$. Expanding in inner variables about inclusion i gives

$$\begin{aligned}
h_\mathrm{o}^{(0)} = c_0 \; & - c_{1i}(\gamma_\mathrm{EM} + \log(\epsilon\rho_i/2\mu)) + \frac{c_{1i}}{4}(1 - \gamma_\mathrm{EM} + \log 2 - \log \epsilon\rho_i/\mu)\frac{\epsilon^2\rho_i^2}{\mu^2} \\
& + c_{2i}\cos(2\phi_i - 2\psi_i)\left(1 + \frac{\epsilon^2\rho_i^2 \log(\epsilon\rho_i/2\mu)}{4\mu^2} + \frac{\epsilon^2\rho_i^2(4\gamma_\mathrm{EM} - 3)}{16\mu^2}\right) \\
& + \sum\nolimits_{j\neq i}\Bigg\{ c_{1j}\Bigg[K_0\left(\frac{R_{ij}}{\mu}\right) + \frac{K_1\left(\frac{R_{ij}}{\mu}\right)}{\mu}\epsilon\rho_i\cos(\phi_i - \theta_{ij}) + \frac{K_0\left(\frac{R_{ij}}{\mu}\right)}{2\mu^2}\epsilon^2\rho_i^2\cos^2(\phi_i - \theta_{ij}) \\
& \qquad + \frac{K_1\left(\frac{R_{ij}}{\mu}\right)}{2\mu R_{ij}}\cos(2\phi_i - 2\theta_{ij})\epsilon^2\rho_i^2\Bigg] \\
& \qquad + c_{2j}\Bigg[\cos(2\psi_j - 2\theta_{ij})\Bigg(f\left(\frac{R_{ij}}{\mu}\right) - \frac{\epsilon\rho_i\cos(\theta_{ij} - \phi_i) f'\left(\frac{R_{ij}}{\mu}\right)}{\mu} \\
& \qquad + \epsilon^2\rho_i^2\Bigg(- \frac{2f\left(\frac{R_{ij}}{\mu}\right)\sin^2(\phi_i - \theta_{ij})}{R_{ij}^2} + \frac{\sin^2(\phi_i - \theta_{ij}) f'\left(\frac{R_{ij}}{\mu}\right)}{2\mu R_{ij}} + \frac{\cos^2(\phi_i - \theta_{ij}) f''\left(\frac{R_{ij}}{\mu}\right)}{2\mu^2}\Bigg)\Bigg) \\
& \qquad + \sin(2\psi_j - 2\theta_{ij})\Bigg(- \frac{2\epsilon\rho_i f\left(\frac{R_{ij}}{\mu}\right)\sin(\phi_i - \theta_{ij})}{R_{ij}} \\
& \qquad + \epsilon^2\rho_i^2\Bigg(- \frac{2\cos(\phi_i - \theta_{ij}) f\left(\frac{R_{ij}}{\mu}\right)\sin(\phi_i - \theta_{ij})}{R_{ij}^2} \\
& \qquad\qquad + \frac{2\cos(\phi_i - \theta_{ij})\sin(\phi_i - \theta_{ij}) f'\left(\frac{R_{ij}}{\mu}\right)}{R_{ij}\mu}\Bigg)\Bigg)\Bigg]\Bigg\} + O(\epsilon^3),
\end{aligned} \tag{3.47}$$

where $f(a) = 4/a^2 - 2K_2(a)$, $R_{ij} = ((x_j - x_i)^2 + (y_j - y_i)^2)^{1/2}$ and $\theta_{ij} = \arctan(x_j - x_i, y_j - y_i)$ (as shown in Figure 3.4). This equation matches the leading order inner solutions to give

$$c_{1i} = -\alpha_i^{(0)}, \quad c_{2i} = \frac{\alpha_i^{(2)}}{2}, \tag{3.48}$$

and

$$\gamma_i^{(0)} = c_0 - c_{1i}\left(\log\left(\frac{\epsilon}{2\mu}\right) + \gamma_{\text{EM}}\right) + \sum\nolimits_{i\neq j}\Big\{c_{1j}K_0(R_{ij}/\mu) + c_{2j}\cos(2\psi_j - 2\theta_{ij})f\left(R_{ij}/\mu\right)\Big\} \tag{3.49}$$

which holds for any inclusion. At first order, the inner equation is

$$\nabla_i^4 h_i^{(1)} = 0, \tag{3.50}$$

$$h_i^{(1)}\Big|_{\rho_i=1} = \gamma_i^{(1)} + \beta_{i1}^{(0)}\cos(\phi_i) + \beta_{i2}^{(0)}\sin(\phi_i), \tag{3.51}$$

$$\frac{\partial h_i^{(1)}}{\partial \rho_i}\Big|_{\rho_i=1} = \beta_{i1}^{(0)}\cos(\phi_i) + \beta_{i2}^{(0)}\sin(\phi_i). \tag{3.52}$$

Additionally, as $\rho_i \to \infty$ the solution must match the first order terms in (3.47) and so

$$\begin{aligned} h_i^{(1)}\Big|_{\rho_i\to\infty} \sim \sum\Bigg\{ & \rho_i\cos(\phi_i)\left(\frac{\cos(\theta_{ij})_{j\neq i}\left(-2\alpha_j^{(0)}K_1\left(\frac{R_{ij}}{\mu}\right) - \alpha_j^{(2)}\cos(2\psi_j - 2\theta_{ij})f'\left(\frac{R_{ij}}{\mu}\right)\right)}{2\mu}\right. \\ & \left. + \frac{\alpha_j^{(2)}\sin(\theta_{ij})f\left(\frac{R_{ij}}{\mu}\right)\sin(2\psi_j - 2\theta_{ij})}{R_{ij}}\right) \\ & + \rho_i\sin(\phi_i)\left(\frac{\sin(\theta_{ij})\left(-2\alpha_j^{(0)}K_1\left(\frac{R_{ij}}{\mu}\right) - \alpha_j^{(2)}\cos(2\psi_j - 2\theta_{ij})f'\left(\frac{R_{ij}}{\mu}\right)\right)}{2\mu}\right. \\ & \left. - \frac{\alpha_j^{(2)}\cos(\theta_{ij})f\left(\frac{R_{ij}}{\mu}\right)\sin(2\psi_j - 2\theta_{ij})}{R_{ij}}\right)\Bigg\}. \end{aligned} \tag{3.53}$$

The solution to (3.50) with the correct limiting behaviour is

$$h_i^{(1)} = \gamma_i^{(1)} + \beta_{i1}^{(0)}\rho_i\cos(\phi_i) + \beta_{i2}^{(0)}\rho_i\sin(\phi_i), \tag{3.54}$$

where the matching gives

$$\begin{aligned}
\beta_{i1}^{(0)} &= \sum\nolimits_{j\neq i} \frac{\cos(\theta_{ij})\left(-2\alpha_j^{(0)}K_1\left(\frac{R_{ij}}{\mu}\right) - \alpha_j^{(2)}\cos(2\psi_j - 2\theta_{ij})f'\left(\frac{R_{ij}}{\mu}\right)\right)}{2\mu} \\
&\quad + \frac{\alpha_j^{(2)}\sin(\theta_{ij})f\left(\frac{R_{ij}}{\mu}\right)\sin(2\psi_j - 2\theta_{ij})}{R_{ij}} \\
\beta_{i2}^{(0)} &= \sum\nolimits_{j\neq i} \frac{\sin(\theta_{ij})\left(-2\alpha_j^{(0)}K_1\left(\frac{R_{ij}}{\mu}\right) - \alpha_j^{(2)}\cos(2\psi_j - 2\theta_{ij})f'\left(\frac{R_{ij}}{\mu}\right)\right)}{2\mu} \\
&\quad - \frac{\alpha_j^{(2)}\cos(\theta_{ij})f\left(\frac{R_{ij}}{\mu}\right)\sin(2\psi_j - 2\theta_{ij})}{R_{ij}}.
\end{aligned} \tag{3.55}$$

Note the difference of sign in the term $\propto \sin(2\psi_j - 2\theta_{ij})$ between $\beta_{i1}^{(0)}$ and $\beta_{i2}^{(0)}$.

Expressing (3.54) in outer variables, the only term that is first order in ϵ is $\gamma_i^{(1)}$. The matching therefore requires

$$h_{\mathrm{o}}^{(1)} = \gamma_i^{(1)}, \tag{3.56}$$

for all i, so that $\gamma_i^{(1)} = \gamma_j^{(1)}$ for all inclusions.

For the second order inner solution we have

$$\nabla_i^4 h_i^{(2)} = \nabla_i^2 h_i^{(0)} = -\frac{2\alpha_1^{(2)}\cos(2\phi_i - 2\psi_i)}{\mu^2\rho^2}, \tag{3.57}$$

$$h_i^{(2)}\Big|_{\rho_i=1} = \gamma_i^{(2)} + \beta_{i1}^{(1)}\cos(\phi_i) + \beta_{i2}^{(1)}\sin(\phi_i), \tag{3.58}$$

$$\frac{\partial h_i^{(2)}}{\partial \rho_i}\Big|_{\rho_i=1} = \beta_{i1}^{(1)}\cos(\phi_i) + \beta_{i2}^{(1)}\sin(\phi_i), \tag{3.59}$$

and from matching with the second order terms in (3.47) we find that

$$
\begin{aligned}
h_i^{(2)}\Big|_{\rho_i\to\infty} \sim & -\rho_i^2\frac{\alpha_i^{(0)}}{4\mu^2}(1-\gamma_{\rm EM}-\log\epsilon-\log\rho_i/2\mu) \\
& +\alpha_i^{(2)}\cos(2\phi_i-2\psi_i)\left(\frac{\epsilon^2\rho_i^2\log(\epsilon\rho_i/2\mu)}{8\mu^2}+\frac{\epsilon^2\rho_i^2(4\gamma_{\rm EM}-3)}{32\mu^2}\right) \\
& +\sum_j\Bigg\{\rho_i^2\Bigg[-\alpha_j^{(0)}\frac{K_0\left(\frac{R_{ij}}{\mu}\right)}{4\mu^2}+\alpha_j^{(2)}\cos(2\theta_{ij}-2\psi_j)\left(\frac{-f\left(\frac{R_{ij}}{\mu}\right)}{2R_{ij}^2}+\frac{f'\left(\frac{R_{ij}}{\mu}\right)}{8\mu R_{ij}}+\frac{f''\left(\frac{R_{ij}}{\mu}\right)}{8\mu^2}\right)\Bigg] \\
& +\cos 2\phi_i\rho_i^2\Bigg[-\alpha_j^{(0)}\cos(2\theta_{ij})\frac{R_{ij}K_0\left(\frac{R_{ij}}{\mu}\right)+2\mu K_1\left(\frac{R_{ij}}{\mu}\right)}{4\mu^2R_{ij}} \\
& +\alpha_j^{(2)}\sin(2\theta_{ij})\sin(2\psi_j-2\theta_{ij})\left(\frac{f\left(\frac{R_{ij}}{\mu}\right)}{2R_{ij}^2}-\frac{f'\left(\frac{R_{ij}}{\mu}\right)}{2\mu R_{ij}}\right) \\
& +\alpha_j^{(2)}\cos(2\theta_{ij})\cos(2\psi_j-2\theta_{ij})\left(\frac{f\left(\frac{R_{ij}}{\mu}\right)}{2R_{ij}^2}-\frac{f'\left(\frac{R_{ij}}{\mu}\right)}{8\mu R_{ij}}+\frac{f''\left(\frac{R_{ij}}{\mu}\right)}{8\mu^2}\right)\Bigg] \\
& +\sin 2\phi_i\rho_i^2\Bigg[-\alpha_j^{(0)}\sin(2\theta_{ij})\frac{R_{ij}K_0\left(\frac{R_{ij}}{\mu}\right)+2\mu K_1\left(\frac{R_{ij}}{\mu}\right)}{4\mu^2R_{ij}} \\
& +\alpha_j^{(2)}\sin(2\theta_{ij})\cos(2\psi_j-2\theta_{ij})\left(\frac{f\left(\frac{R_{ij}}{\mu}\right)}{2R_{ij}^2}-\frac{f'\left(\frac{R_{ij}}{\mu}\right)}{8\mu R_{ij}}+\frac{f''\left(\frac{R_{ij}}{\mu}\right)}{8\mu^2}\right) \\
& +\alpha_j^{(2)}\cos(2\theta_{ij})\sin(2\psi_j-2\theta_{ij})\left(\frac{f\left(\frac{R_{ij}}{\mu}\right)}{2R_{ij}^2}-\frac{f'\left(\frac{R_{ij}}{\mu}\right)}{2\mu R_{ij}}\right)\Bigg]\Bigg\},
\end{aligned}
\tag{3.60}
$$

where we have used that as $a\to 0$,

$$
f\sim 1+\frac{a^2\log(a/2)}{4}+\frac{(4\gamma_{\rm EM}-3)a^2}{16}. \tag{3.61}
$$

Identifying the terms that depend on the inner coordinate system we write this last expression as

$$
\begin{aligned}
h_i^{(2)}\Big|_{\rho_i\to\infty} =& M_C\rho_i^2\cos(2\phi_i)+M_S\rho_i^2\sin(2\phi_i)+M_0\rho_i^2+M_1\rho_i^2\log\rho_i \\
& +\alpha_i^{(2)}\cos(2\phi_i-2\psi_i)\left(\frac{\rho_i^2\log(\epsilon\rho_i/2\mu)}{8\mu^2}+\frac{\rho_i^2(4\gamma_{\rm EM}-3)}{32\mu^2}\right).
\end{aligned}
\tag{3.62}
$$

The solution is, therefore,

$$
\begin{aligned}
h_i^{(2)} =& \gamma_i^{(2)}+\alpha_i^{(2)}\cos(2\phi_i-2\psi_i)\left(\frac{\rho_i^2\log(\epsilon\rho_i/2\mu)}{8\mu^2}+\frac{\rho_i^2(4\gamma_{\rm EM}-3)}{32\mu^2}\right) \\
& +\mathcal{M}_C\left(\rho_i^2-2+\frac{1}{\rho_i^2}\right)\cos(2\phi_i)+\mathcal{M}_S\left(\rho_i^2-2+\frac{1}{\rho_i^2}\right)\sin(2\phi_i) \\
& +M_0(-1+\rho_i^2-2\ln\rho_i)+M_1(\rho_i^2\ln\rho_i-\ln\rho_i),
\end{aligned}
\tag{3.63}
$$

where we have considered each angular mode separately. Terms that include either $\cos(n\phi_i)$ and $\sin(n\phi_i)$ with $n \geq 3$ do not appear in the solution to the shape equation as they cannot satisfy the matching and boundary conditions. When $n = 1$, the solution would be $(A_1(\rho_i - \rho_i^{-1} - 2\rho_i \log(\rho_i)) + \beta_{i1}^{(1)}\rho_i)\cos(\phi_i)$ and similarly for $\sin(\phi_i)$. However, matching with (3.56) gives $A_1 = \beta_{i1}^{(1)} = \beta_{i2}^{(1)} = 0$ and so there is no $n = 1$ contribution to $h_i^{(2)}$.

Writing out the full solution gives

$$
\begin{aligned}
h_i^{(2)} = \; & \gamma^{(2)} + \frac{\left(-\alpha_i^{(0)}\right)}{4\mu^2}\left(\rho_i^2 \log\rho_i - \log\rho_i\right) + \frac{\alpha_i^{(2)}}{16\mu^2}\cos(2\phi_i - 2\psi)\Bigg(\rho_i^2(2\gamma_{\mathrm{EM}} - 3/2) \\
& \qquad + \frac{2\gamma_{\mathrm{EM}} - 1/2 + 2\log\left(\frac{\epsilon}{2\mu}\right)}{\rho_i^2} + 2 - 4\gamma_{\mathrm{EM}} - 4\log\left(\frac{\epsilon}{2\mu}\right)\Bigg) \\
& + \left(-1 + \rho_i^2 + 2\log\rho_i\right)\Bigg\{\frac{\left(-\alpha_i^{(0)}\right)}{4\mu^2}(1 - \gamma_{\mathrm{EM}} - \log(\epsilon/2\mu)) + \sum_{j\neq i}\Bigg[\left(-\alpha_j^{(0)}\right)\frac{K_0\left(\frac{R_{ij}}{\mu}\right)}{4\mu^2} \\
& \qquad + \left(\frac{\alpha_j^{(2)}}{2}\right)\cos(2\theta_{ij} - 2\psi_j)\left(\frac{-f\left(\frac{R_{ij}}{\mu}\right)}{R_{ij}^2} + \frac{f'\left(\frac{R_{ij}}{\mu}\right)}{4\mu R_{ij}} + \frac{f''\left(\frac{R_{ij}}{\mu}\right)}{4\mu^2}\right)\Bigg]\Bigg\} \\
& + \sum_{j\neq i}\Bigg\{\cos 2\phi_i\left(\rho_i^2 - 2 + \frac{1}{\rho_i^2}\right)\Bigg[\left(-\alpha_j^{(0)}\right)\cos(2\theta_{ij})\frac{R_{ij}K_0\left(\frac{R_{ij}}{\mu}\right) + 2\mu K_1\left(\frac{R_{ij}}{\mu}\right)}{4\mu^2 R_{ij}} \\
& \qquad + \left(\frac{\alpha_j^{(2)}}{2}\right)\sin(2\theta_{ij})\sin(2\psi_j - 2\theta_{ij})\left(\frac{f\left(\frac{R_{ij}}{\mu}\right)}{R_{ij}^2} - \frac{f'\left(\frac{R_{ij}}{\mu}\right)}{\mu R_{ij}}\right) \\
& \qquad + \left(\frac{\alpha_j^{(2)}}{2}\right)\cos(2\theta_{ij})\cos(2\psi_j - 2\theta_{ij})\left(\frac{f\left(\frac{R_{ij}}{\mu}\right)}{R_{ij}^2} - \frac{f'\left(\frac{R_{ij}}{\mu}\right)}{4\mu R_{ij}} + \frac{f''\left(\frac{R_{ij}}{\mu}\right)}{4\mu^2}\right)\Bigg] \\
& \quad + \sin 2\phi_i\left(\rho_i^2 - 2 + \frac{1}{\rho_i^2}\right)\Bigg[\left(-\alpha_j^{(0)}\right)\sin(2\theta_{ij})\frac{R_{ij}K_0\left(\frac{R_{ij}}{\mu}\right) + 2\mu K_1\left(\frac{R_{ij}}{\mu}\right)}{4\mu^2 R_{ij}} \\
& \qquad + \left(\frac{\alpha_j^{(2)}}{2}\right)\sin(2\theta_{ij})\cos(2\psi_j - 2\theta_{ij})\left(\frac{f\left(\frac{R_{ij}}{\mu}\right)}{R_{ij}^2} - \frac{f'\left(\frac{R_{ij}}{\mu}\right)}{4\mu R_{ij}} + \frac{f''\left(\frac{R_{ij}}{\mu}\right)}{4\mu^2}\right) \\
& \qquad + \left(\frac{\alpha_j^{(2)}}{2}\right)\cos(2\theta_{ij})\sin(2\psi_j - 2\theta_{ij})\left(\frac{f\left(\frac{R_{ij}}{\mu}\right)}{R_{ij}^2} - \frac{f'\left(\frac{R_{ij}}{\mu}\right)}{\mu R_{ij}}\right)\Bigg]\Bigg\}.
\end{aligned}
\tag{3.64}
$$

This gives sufficient terms in the expansion of the height to calculate the deformation energy.

3.4.3 Membrane Interaction Energy

We can now use the shape of the membrane to find the energy of a given configuration of inclusions. The energy comes from evaluating (3.4) which can be more easily calculated in this regime by integrating by parts, and evaluating the boundary terms as in (3.20). Since the membrane is flat at infinity ($\partial h/\partial \rho_i = 0$ as $\rho_i \to \infty$) the integral is simply the integral around the edge of each inclusion which we calculate in the inner region. Therefore, to first order in ϵ, we have

$$\bar{E} = \sum_{i=1}^{N} B_i, \tag{3.65}$$

where B_i is the boundary energy term around the ith inclusion, given by:

$$\begin{aligned} B_i = {} & \pi \left(\alpha_i^{(2)}\right)^2 \left(\frac{1}{\epsilon^2} + \frac{\gamma_{\text{EM}}}{\mu^2} + \frac{\log(\frac{\epsilon}{2\mu})}{\mu^2}\right) - \pi \left(\alpha_i^{(0)}\right)^2 \left(\frac{\gamma_{\text{EM}}}{2\mu^2} + \frac{\log(\frac{\epsilon}{2\mu})}{2\mu^2}\right) \\ & \sum_{j\neq i} \left[\frac{\pi \alpha_i^{(2)} \alpha_j^{(2)}}{2\mu^2} \left(\cos\left(4\theta_{ij} - 2(\psi_i + \psi_j)\right) \left(\frac{-48\mu^4}{R_{ij}^4} + K_4\left(\frac{R_{ij}}{\mu}\right)\right) \right.\right. \\ & \qquad \left.\left. + \cos\left(2\psi_i - 2\psi_j\right) K_0\left(\frac{R_{ij}}{\mu}\right) \right) \right. \\ & \left. + \frac{\pi \alpha_i^{(0)} \alpha_j^{(0)}}{\mu^2} K_0\left(\frac{R_{ij}}{\mu}\right) + \frac{\pi \alpha_i^{(0)} \alpha_j^{(2)}}{\mu^2} \cos(2\psi_j - 2\theta_{ij}) K_2\left(\frac{R_{ij}}{\mu}\right) \right. \\ & \qquad \left. + \frac{\pi \alpha_j^{(0)} \alpha_i^{(2)}}{\mu^2} \cos(2\psi_i - 2\theta_{ij}) K_2\left(\frac{R_{ij}}{\mu}\right) \right]. \end{aligned} \tag{3.66}$$

We recognise the constant term before the sum as the deformation energy from a single inclusion given by (3.23) and note that it is independent of the inclusion configuration. The remaining part of the energy consists of an interaction term that for each inclusion runs over the sum of all other inclusions. We can rewrite this double sum as a sum over all unique pairs of inclusions. For each pair of inclusions, labelled k and l, there will be a contribution to the energy when $i = k$ and $j = l$ and also when $i = l$ and $j = k$ and from the geometry of the system $R_{kl} = R_{lk}$ and $\theta_{kl} = \theta_{lk} + \pi$ (up to a shift of 2π). Thus, the summand is unchanged under the exchange of these indices and both terms involving a unique pair of inclusions are the same. We conclude with the following important observation: *the interaction energy of a configuration of multiple inclusions is the pairwise sum of all the two-body interaction energy terms.*

3.4.4 Identical Inclusions

Next, we will focus on the case of systems with identical inclusions, $\alpha_i^{(0)} = \alpha^{(0)}$, $\alpha_i^{(2)} = \alpha^{(2)}$, and an identical anisotropy parameter $\omega = \alpha^{(2)}/\alpha^{(0)}$. In this case, the membrane deformation energy can be scaled with the magnitude of the induced curvature. We can therefore write the membrane energy as

$$\bar{E} = \frac{\pi(\alpha^{(0)})^2}{\mu^2}(\bar{E}_\infty + \bar{E}'), \tag{3.67}$$

where $\bar{E}_\infty$ is the constant term from the energy of embedding each inclusion infinitely far apart so that they do not interact and $\bar{E}'$ is the interaction energy between inclusions. We will consider the case where $\mu = 1$. Changing μ alters the interaction energy as shown in (3.67) and additionally simply acts to scale the inclusion separations. In this case, we define

$$\begin{aligned}\bar{E}_2(R_{ab}, \psi_a, \psi_b) = {} & 2K_0(R_{ab}) + 2\omega K_2(R_{ab})(\cos 2\psi_a + \cos 2\psi_b) \\ & + \omega^2 \cos(2(\psi_a - \psi_b))K_0(R_{ab}) \\ & + \omega^2 \cos(2(\psi_a + \psi_b)) \left(K_4(R_{ab}) - \frac{48}{R_{ab}^4} \right),\end{aligned} \tag{3.68}$$

and the interaction deformation energy is

$$\bar{E}' = \sum_i^n \sum_{j=i+1}^n \bar{E}_2(R_{ij}, \psi_i - \theta_{ij}, \psi_j - \theta_{ij}). \tag{3.69}$$

The scaled two-body interaction energy between two inclusions with positions $\{(x_1, y_1),\ (x_2, y_2)\}$ and orientations $\{\psi_1, \psi_2\}$ is

$$\begin{aligned}&\bar{E}_{xy}(x_1, x_2, y_1, y_2, \psi_1, \psi_2) = \\ &\bar{E}_2 \left(\sqrt{(x_1-x_2)^2+(y_1-y_2)^2}, \psi_1 - \arctan(x_1-x_2, y_1-y_2), \psi_2 - \arctan(x_1-x_2, y_1-y_2) \right).\end{aligned} \tag{3.70}$$

3.4.5 Features of the Two-Body Interaction Potential

The interaction between multiple inclusions is the pairwise sum of individual interactions and so we expect insight into the collective behaviour to come from features of this two-body interaction potential. We focus on the case of identical inclusions and set for all inclusions $\alpha_i^{(0)} = 1$, $\alpha_i^{(2)} = \omega$, where setting the strength of the monopole

to 1 simply rescales the interaction energy. For radially symmetric inclusions with no quadrupole moment (analogous to $\omega = 0$), previous work showed that the interaction energy between two identical inclusions decreases with separation, and the interaction exerts a repulsive force to push the inclusions apart [82].

When the inclusions are anisotropic the interaction also depends on the relative orientation of the inclusions as well as the separation between them. At every separation of the two inclusions there will be some orientation that minimises the energy. There exists a *critical anisotropy*, $\omega^* \approx 0.242$, such that for $\omega > \omega^*$ the minimum energy strictly increases with separation and the interaction is *attractive* for all values of R_{ab} (see Figure 3.6 and below). The anisotropy therefore changes the interaction from being *repulsive* to being *attractive*. Other work also reports attractive interactions for inclusions that break the symmetry in tension-less systems, for example by considering elliptical inclusions [83].

When the anisotropy is smaller, $0 < \omega < \omega^*$, then the interaction potential is non-monotonic and the interaction force changes from being attractive to being repulsive, Figure 3.5 show examples of this interaction potential. In this regime, the interaction energy is minimised when $\psi_1 = \psi_2 = \pi/2$ and the system undergoes a bifurcation to give an unstable equilibrium at separation $\tilde{R}$, and a larger stable equilibrium separation at R^*. The bifurcation diagram in Figure 3.6 shows this transition and as $\omega \to 0$ we see that $\tilde{R} \to 0$ and $R^* \to \infty$ which gives a limiting behaviour that agrees with the symmetric inclusion case.

The fact that this energy is pairwise might be surprising. Recent theoretical work identified that the multibody interactions can in fact be of similar size to the two body interactions when the membrane is tensionless [84], or at short distances where the inclusions impose large contact angles [85]. However, in the model developed here the membrane tension is nonzero and comparable to the bending stiffness and the inclusions are well separated with each inclusion inducing a small deformation. The tension will localise the membrane deformation to each inclusion with small slowly varying deformations in the outer region connecting the inclusions. It is these small deformations in the outer region through which the inclusions interact.

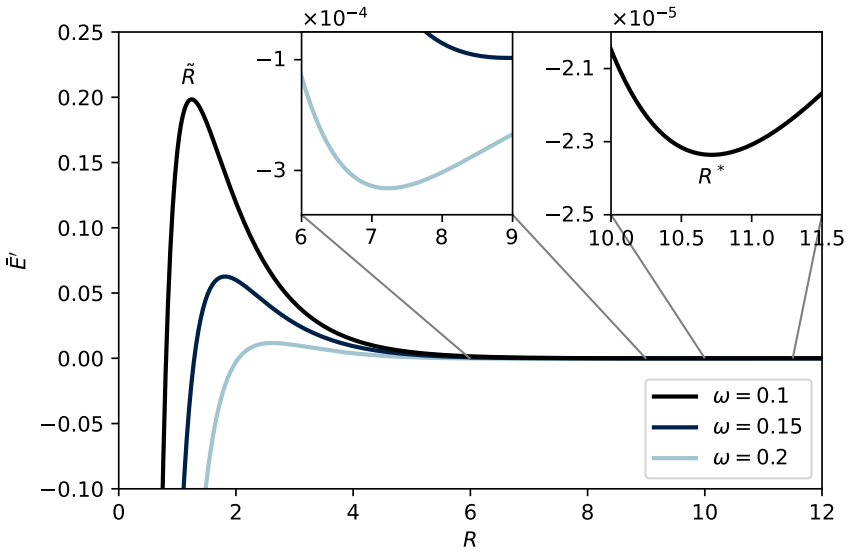

Figure 3.5: Energy of a configuration of two inclusions separated by a distance R, with the inclusions orientated perpendicular to the line separating them. The maximum $\bar{E}'$ defines the value of $\tilde{R}$ and the stable equilibrium (locally minimum $\bar{E}'$) at R^* is shown in the inset (for $\omega = 0.1$).

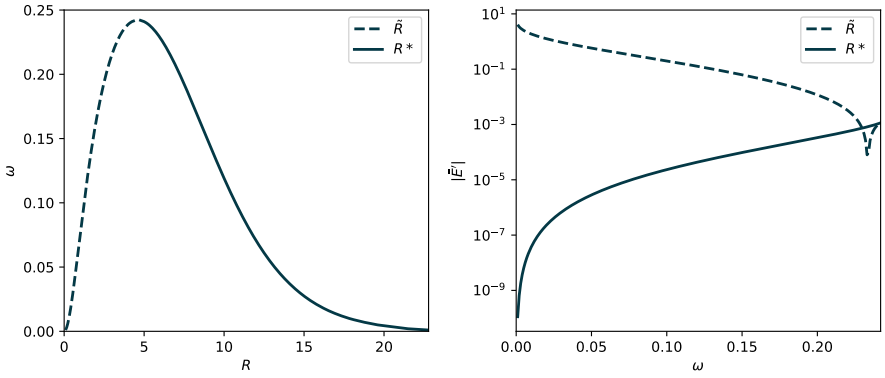

Figure 3.6: Bifurcation diagram showing how the existence of equilibrium solutions depends on the anisotropy parameter, ω.

3.5 Systems of Interacting Inclusions

Armed with this potential describing the interactions between curvature inducing inclusions, we can explore the structures and dynamics of various configurations of inclusions. The fluid mosaic structure of the lipid bilayer allows for in-plane fluid flows with high viscosity [86], [87]. Forces acting on inclusions embedded in a lipid bilayer will therefore cause motion as the flows allow the system to relax and find an

energy minimum. Due to the high viscosity, we expect the motion to be overdamped and so each inclusion undergoes a gradient descent in the energy of the system, given by the interaction potential derived earlier. Continuing with the flat membrane approximation, we take the gradient of the energy in the xy-reference plane which we used to construct the Monge parameterisation. The motion of each variable follows

$$\dot{q}_i = \bar{\mu}_q F_{q_i} = -\bar{\mu}_q \frac{\partial \bar{E}'}{\partial q_i}, \tag{3.71}$$

where q is either x, y, or ψ, $\bar{\mu}_q$ is a non-dimensional mobility, and F_{q_i} is the force acting on the particle (note that q is non-dimensional). When the energy is at a minimum in all variables, the configuration will not evolve in time and we call this a stationary configuration.

From the xy symmetry of an infinite membrane, we have that $\bar{\mu}_x = \bar{\mu}_y$ and mobilities are connected to diffusivities via the Einstein relation ($D \propto \mu$). The ratio of the translational and rotational diffusivity $D_T/D_R \propto \epsilon^2$ where ϵ is the radius of the circular inclusion and $\epsilon \ll 1$. As such we expect that $\bar{\mu}_x, \bar{\mu}_y \ll \bar{\mu}_\psi$ so that the orientation of the inclusions relaxes much faster than their position [83], [88]. In this work we will often take $\bar{\mu}_\psi = 10\bar{\mu}_x = 10\bar{\mu}_y$.

Starting with an initial configuration of inclusions, we can evolve the system numerically using a third order Backward Differentiation Formula method [89]. This will allow us to study the evolution of inclusions subject to membrane mediated elastic interactions.

3.6 Rings, Lines and Lattices

3.6.1 Rings

There are many possible ways to arrange n inclusions, with each inclusion being described by two positional coordinates and an angle describing the orientation. This creates a huge space of possible inclusion configurations. To gain insight about inclusion interactions, we start with simple geometries, such as lines, rings, and lattices. Due to their symmetry, rings are particularly easy to handle. Therefore, we investigate inclusion interactions by placing them evenly on the vertices of a n

sided polygon of radius l. We first look for the conditions that such a configuration is an equilibrium, then explore its stability and how stability changes depending on the asymmetry parameter (ω), or the spacing between the inclusions (the size of the ring). We restrict the study to configurations where all inclusions are separated by at least $\tilde{R}$ to prevent the collapse of structures caused by the diverging interaction energy for small separations.

The ring is parameterised by the number of inclusions, n, and their distance, l, from a central point. This forms a regular polygon of edge length $l_e = 2l\sin(\pi/n)$ — the separation between neighbouring inclusions. We label each inclusion from 1 to n with the i^{th} inclusion at position

$$(x_i, y_i) = (l\cos(2\pi i/n), l\sin(2\pi i/n)), \quad i = 1, \ldots, n. \tag{3.72}$$

However, there are two choices of ψ_i for the inclusions to form a maximally symmetric arrangement. These arrangements are when the axis of each inclusion either points radially ($\psi_i = 2\pi/i$) or tangentially ($\psi_i = 2\pi/i + \pi/2$) as sketched in Figure 3.7. We can calculate the energy as a function of the radial separation. The energy for a symmetric arrangement of n inclusions is given by

$$\bar{E}_n^{\text{ring}} = \frac{n}{2}\sum_{i=1}^{n-1} \bar{E}_{xy}(l, l\cos(2\pi i/n), 0, l\sin(2\pi i/n), 0, 2\pi i/n) \tag{3.73}$$

where rather than summing over all pairs we just note the n-fold rotational symmetry. The factor $n/2$ prevents double counting and when $n = 2$, we recover the two body interaction energy given by (3.70).

For a ring of n inclusions, there is some edge length, $l_e(n)$ that minimises the energy of the configuration. This equilibrium ring size can be determined numerically and is shown in Figure 3.8 for varying n and for two different values of ω. There are two different values of l_e for each n: the inclusion separation that minimises the radial configuration, $l_e^R(n)$, or the tangential configuration, $l_e^T(n)$. Depending on n, we find the following equilibrium configurations:

- When $n < 4$, the tangential equilibrium ring is smallest, $l_e^T(n) < l_e^R(n)$.

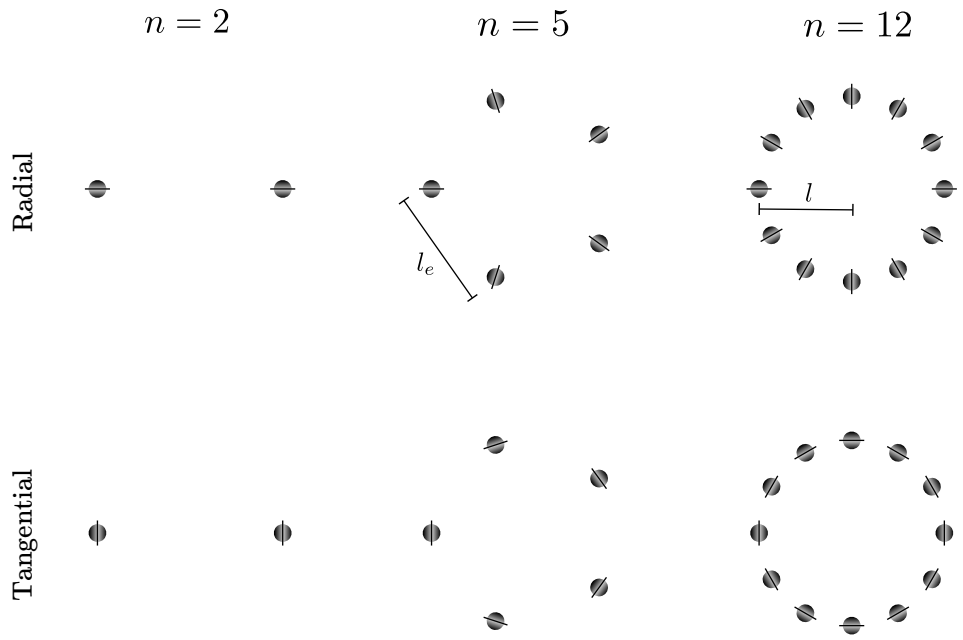

Figure 3.7: Radial and tangential setup for rings of $n = 2, 5, 12$.

- When $n = 4$, we have $l_e^T(4) \approx l_e^R(4)$ (with $l_e^T(4) < l_e^R(4)$). This is due to the fact that the symmetry of the two body interaction implies that the adjacent inclusions have the same interaction energy in both the radial and tangential configurations and the only difference between the two configurations comes from the pairs of inclusions in opposite corners. In fact, only the diagonal energy term that is proportional to $(\cos 2\psi_a + \cos 2\psi_b)$ is different between the two arrangements.

- For $n > 4$, we have, $l_e^T(n) > l_e^R(n)$, the radial equilibrium ring is smallest and for large n we find that $l_e^T(n) \approx l_e^R(2)$ and $l_e^R(n) \approx l_e^T(2)$. This can be understood as follows: for large n, adjacent inclusions in the tangential configuration look very similar to the radial configuration of the two inclusion case i.e. nearest neighbours for the tangential $n = 12$ in Figure 3.7 look similar to the setup in the radial $n = 2$ case on the left of the figure.

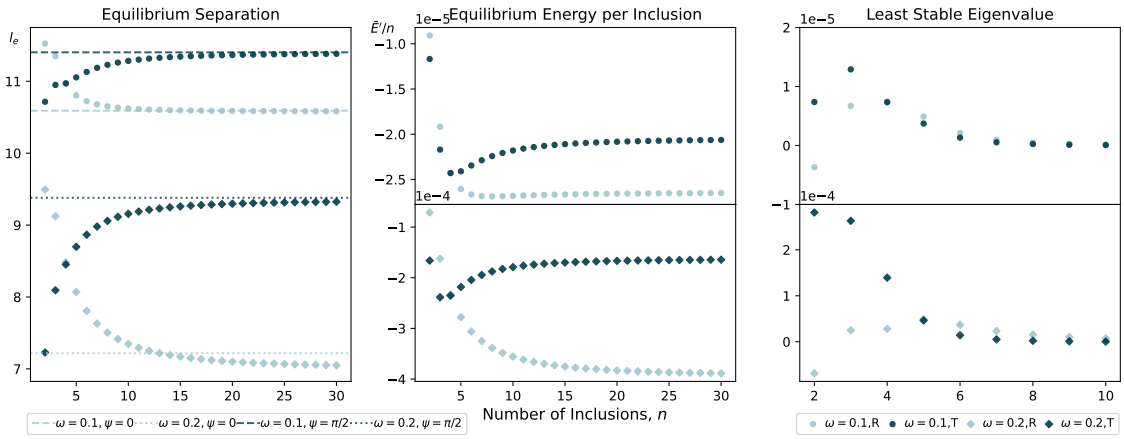

Figure 3.8: Comparisons of the equilibrium ring configurations for different sized rings, showing; inclusion to inclusion separation (left), energy per inclusion (centre), and least table eigenvalue (right) for inclusions with $\omega = 0.1$ and $\omega = 0.2$. Both the radial and tangential configurations are shown. The radial configuration all have $\psi_i^R = 2\pi i/n$, compared to the tangential case of $\psi_i^T = 2\pi i/n + \pi/2$.

The stability of a configuration of inclusions can be determined by studying the eigenvalues of the energy Hessian matrix, $\mathbf{H} \in \mathbb{R}^{3n\times 3n}$, evaluated for a ring configuration. Here, the Hessian is defined as

$$\mathbf{H}_{ij} = \frac{\partial^2 \bar{E}'}{\partial p_i \partial q_j}, \quad i,j = 1,\dots,n, \quad p,q \in x,y,\psi. \tag{3.74}$$

If the Hessian is positive semidefinite, $\mathbf{H} \succeq 0$, all of the eigenvalues are positive and the energy increases under any perturbation. This means the equilibrium is stable and under the overdamped dynamics, the system will approach this minimum state from other configurations in the basin of attraction.

The Hessian and the eigenvalues can be calculated for different sized rings. For any n there are three zero eigenvalues that correspond to the symmetries of the energy: two orthogonal translations of all inclusions and a rotation of the position and angle of all inclusions. In addition to these modes, for $n > 2$ all other perturbations increase the energy of the system and we conclude that: *rings of n inclusions are stable for all $n > 2$.*

The Hessian, $\mathbf{H}$, being a $3n \times 3n$ matrix, it is difficult to provide a clear interpretation of its eigenvectors for large n. Since we expect the translational dynamics to be much slower than the rotational dynamics, we can reduce the

number of degrees of freedom by considering only the rotational degree of freedom for each inclusion.

Perturbations in the angle are always stable. However it is instructive to study the corresponding mode associated with the eigenvectors. When n is even for both the radial and tangential configurations, the least stable mode - i.e. the mode with the least positive eigenvalue - is a mode with the angles all perturbed by the same magnitude, but with alternating sign between adjacent inclusions, i.e. $\delta\psi_i = (-1)^i\delta\psi$. For rings with odd numbers of inclusions these alternating rotations would create a mismatch between the first and n^{th} inclusions which can generate a frustration in exciting this oscillatory mode. In fact, for $n > 3$ and odd, the eigenvector with the lowest eigenvalue still corresponds to rotating adjacent inclusions in opposite directions however the magnitude of these rotations varies in such a way that at the mismatch the magnitude of the rotation is very small, $\delta\psi_i \propto (-1)^i \sin(\pi i/n)$. Uniquely when $n = 2$, the radial configuration is unstable, however the unstable mode is given by an equal and opposite rotation of each inclusion.

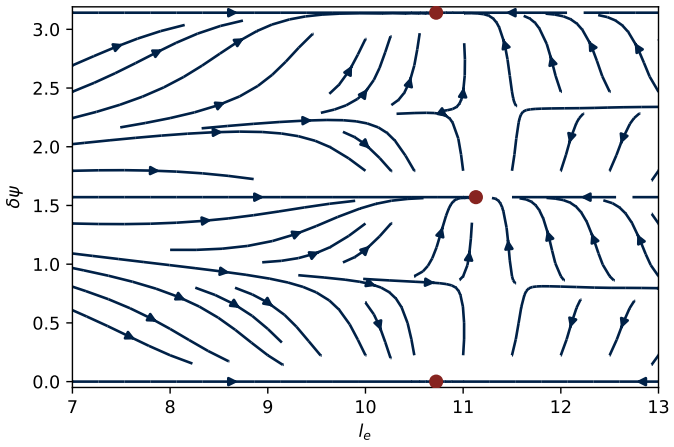

Figure 3.9: Stream plot showing gradient descent for a ring of inclusions in the reduced parameter space of the alternating angular modes at various inclusion-to-inclusion separations. Shown for $n = 6$, $\omega = 0.1$ and the key features are the same for $\omega = 0.2$.

Focusing on a ring with even n number of inclusions, this eigenvector with alternating signs for the rotation connects the radial and tangential configurations. For example starting at the radial configuration, if we perturb all angles by $\delta\psi_i =$

$(-1)^i\pi/2$, the system will be in the tangential configuration. This path represents a trajectory between the two configurations with constant ring radius l that begins and ends along the path of minimum energy. Setting $\psi_i = (-1)^i\delta\psi + 2\pi i/n$ and varying $\delta\psi$ and l_e we can explore the energy landscape of these configurations in a massively reduced parameter space that will still give a good representation of the stability of the system.

Figure 3.9 shows the gradient descent flow of a ring of inclusions constrained to be evenly radially distributed with an inter inclusion length of l_e, and with orientation perturbations that alternate when measured from the radial configuration. The minima for the two maximally symmetric cases are shown by the red dots and, as expected, the system will approach these two stable configurations anywhere in the phase space. At large l_e the system will approach the nearest configuration in angular space, however at low separations the system approaches the radial ($\delta\psi = 0$) configuration for a wider range of angles.

Despite being a subspace of all possible configurations, this observation is informative of the basin of attraction of these two equilibria in all configuration space and indeed when simulating the gradient descent of a random set of perturbations, it is observed that the radial configuration emerges more frequently when the system is initialised at a smaller l_e.

3.6.2 Lines

Infinite Lines

As the number of inclusions in the ring increases, the length between neighbouring inclusions, l_e, converges to a constant equilibrium value and the ring radius tends to infinity. In the limit this ring of inclusions becomes a line of inclusions separated by l_e, and with all inclusions having the same orientation, either $\psi_i = 0$ or $\pi/2$ which are analogous to the limits of the tangential or radial rings respectively. Similarly to rings of inclusions, we can explore the energy landscape of the line. Since there are infinitely many inclusions, we expect the energy of the configuration to be infinite. The energy of the interacting inclusions will still be pairwise and

so we define the energy of a radial line ($\psi_i = \pi/2$) of inclusions with a separation l_e to be $\bar{E}^R_{line}(l_e)$. We have

$$\begin{aligned}\bar{E}^R_{line}(l_e) &= \sum_{i\neq j} \bar{E}_2(R_{ij}, \pi/2, \pi/2) \\ &= \sum_{i=-\infty}^{\infty} \sum_{j=1}^{\infty} \bar{E}_2(l_e \times j, \pi/2, \pi/2),\end{aligned} \tag{3.75}$$

where we can identify the energy *per inclusion* of the line as $\sum_{j=1}^{\infty} \bar{E}_2(l_e \times j, \pi/2, \pi/2)$. When x is large, $K_\nu(x) \sim e^{-x}/\sqrt{x}$ and therefore $\sum_{n=1}^{\infty} K_\nu(nx)$ will converge. We also have $\sum_{n=1}^{\infty}(1/n^4) = \pi^4/90$ and so the energy per inclusion in an infinite line will be finite (see $\delta\psi = 0$ in Figure 3.10).

For rings of inclusions, we studied the least stable perturbation of the orientations of the inclusions, where each inclusion is rotated by the same amount but in opposite directions. A line of inclusions can be perturbed in the same way and again this will transition between a configuration with $\psi_i = 0$ to $\psi_i = \pi/2$ for all inclusions, i. The energy of a system with $\psi_i = (-1)^i \delta\psi$ is given by summing over the inclusions that are rotated in the opposite and same direction separately. The energy of the perturbed line is given by

$$\begin{aligned}\bar{E}_{alt}(\delta\psi) =& 2\sum_{i=1}^{\infty} K_0(l_e \times i) - 4\omega\cos(2\delta\psi)\sum_{i=1}^{\infty} K_2(l_e \times i) + \omega^2 \sum_{i=1,\text{even}}^{\infty} K_0(l_e \times i) \\ &+ \omega^2\cos(4\delta\psi)\sum_{i=1,\text{odd}}^{\infty} K_0(l_e \times i) \\ &+ \omega^2\cos(4\delta\psi)\sum_{i=1,\text{even}}^{\infty}\left(K_4(l_e \times i) - \frac{48}{(l_e \times i)^4}\right),\end{aligned} \tag{3.76}$$

and can be plotted, analogously to Figure 3.9. The energy profile for the line is shown in Figure 3.10. Similarly to the rings, the line is stable when $\delta\psi = 0$ or $\pi/2$. These configurations correspond to end-to-end alignment of anisotropic inclusions, forming linear aggregates. The interactions from the infinite line therefore stabilises the unstable two body radial configuration, similarly to the rings of inclusions. The energy minimum is deeper when the inclusions are aligned perpendicular to their separation, when $\delta\psi = 0$, and this configuration is likely to also have a larger basin of attraction than when $\delta\psi = \pi/2$. Similar structures have been

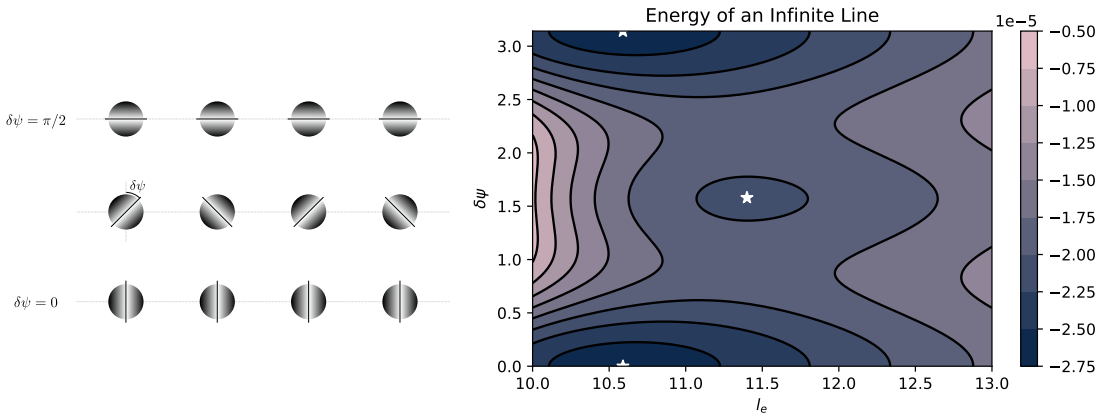

Figure 3.10: Interaction energy per inclusion for an infinite line inclusions. The energy is calculated by evaluating (3.76) and is plotted as the inclusion separation and alternating mode perturbation are varied. The schematic on the left shows the configurations.

observed experimentally [90] and in molecular dynamics simulations [91], where the lines of inclusions then localise to membrane buds and support the formation of membrane tubules.

Finite Lines

Lines with a finite number of inclusions are relevant to the study of physically realisable finite systems. The existence of an infinite line would require an infinite system, but also it is likely that shorter lines made up of fewer inclusions will form as intermediates if longer (or even infinite) lines of inclusions were to form. Again, there are two obvious orientations of inclusions to study, but unlike the infinite line each inclusion sees a different arrangement of the other inclusions. As such the equilibrium separation between neighbouring inclusions is not constant but depends on their position along the line. The more central inclusions on the lines have a slightly lower separation than those closer to the ends, however this variation in separation was seen to be at most a change of around 2% between the different inclusions.

Again, by studying the Hessian of energy at this stationary configuration, we observe that a finite line of inclusions along the x-axis with the inclusions orientated at $\psi_i = \pi/2$ is stable. This is the configuration similar to the radial ring configuration.

However, when the inclusions are orientated at $\psi_i = 0$, the finite line is no longer stable (analogous to the tangential ring).

For the specific case of a finite line of two inclusions, we saw earlier that only one angular orientation was stable. Larger, but still finite lines of inclusions with tangential alignment remain unstable and in particular a long oscillatory mode is excited as the line transitions into another configuration. The ring geometry was able to stabilise the unstable two-body interaction however the finite line does not.

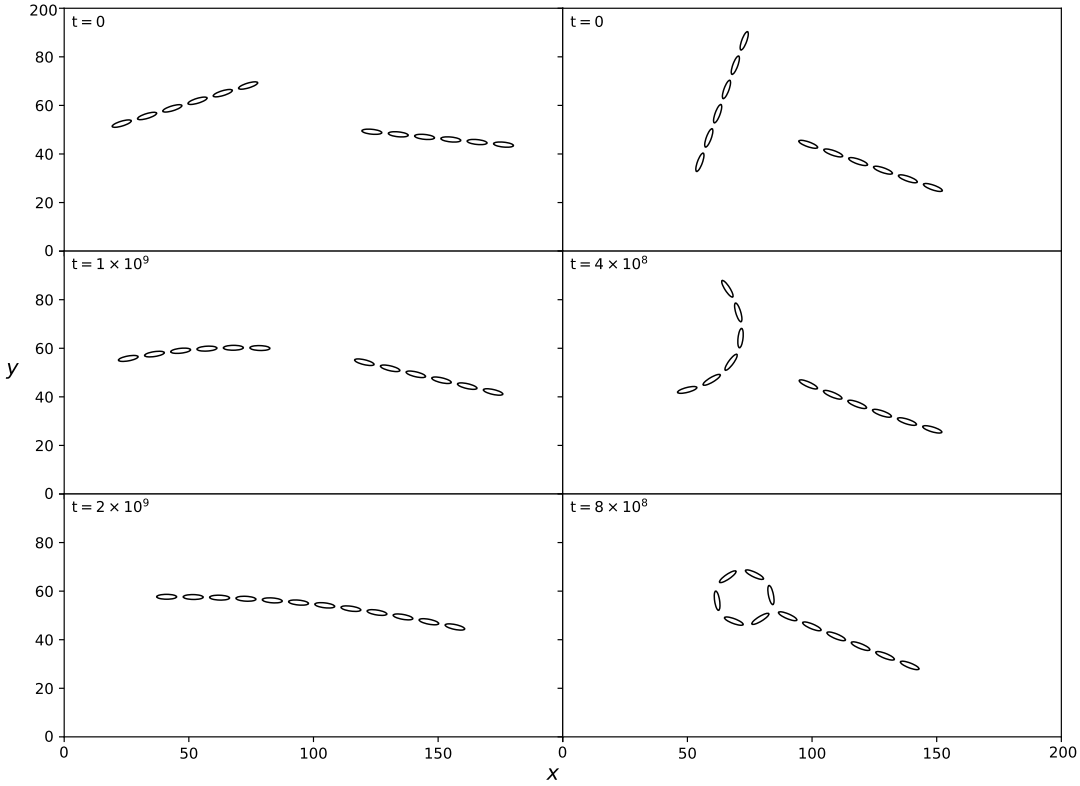

Figure 3.11: Examples of the dynamics of two interacting finite lines with different initial relative orientations, either approximately aligned (left column) or perpendicular (right column). Distances non-dimensionalised by L and time by $\bar{\mu}_x$. The ellipse is drawn such that the normal aligns with the inclusion orientation. In the simulation $\omega = 0.1$ and $\bar{\mu}_x = \bar{\mu}_y = \bar{\mu}_\psi/10$.

Two or more stable finite lines will also interact with each other via the elastic mediated interaction. Allowing a group of finite lines to evolve subject to this potential we find that short lines, such as pairs or three co-linear inclusions, will rotate so that their orientations align and then attract to form a large finite line. For larger co-linear groups of inclusions, the initial distribution of the lines can

affect the final configuration. Figure 3.11 shows two examples of interacting finite lines of inclusions. A group of inclusions that approach a line perpendicular to the line of the inclusions will generate different interactions with the different inclusions in the line. As the groups of inclusions approach, this difference in interaction can become large enough to bend the line and transition into a radial ring of inclusions (right hand column of Figure 3.11). If the two finite lines of inclusion are aligned initially (but with a spacing to form distinct groups), then the lines will simply coalesce into a longer line (left hand column of Figure 3.11). As such, the final configuration depends on the initial distributions of the lines.

3.6.3 General Configurations

Studying rings and lines is useful as these configurations massively reduce the number of coordinates needed to describe the system. In biophysical systems, observed inclusion configurations can be initially generated by diffusing proteins binding onto the membranes or as a consequence of driven cellular process that may drag inclusions before detaching, for example from the membrane-cortex attachment [92]. It is therefore useful to explore the elastic forces acting on generic inclusion arrangements which will not necessarily be as symmetric as the rings and lines. We can explore the evolution of a generic configuration by evolving the system to respond to gradients in energy in the overdamped regime, following the dynamics in (3.71). We choose $\bar{\mu}_x = \bar{\mu}_y = \bar{\mu}_\psi/10$, so that the inclusions rotate more quickly in response to gradients of a free energy than they translate and the system is initialised in a random starting configuration with all separations between inclusions greater than $\tilde{R}$ (defined in Figure 3.5). Ensuring this initial separation prevents any of the inclusions from collapsing with diverging energy and allows us to observe the subsequent relaxation of the system to a minimum energy configuration.

As the system is allowed to evolve according to the gradient descent dynamics, the inclusions begin to form aggregates. The system relaxes to a low energy state, where each inclusion is surrounded by a set of neighbouring inclusions that are all approximately R^* away. This makes sense: the interaction from nearby inclusions

gives the main contribution to the interaction energy and so the system will try to minimise the two body interaction energy for neighbouring inclusions, however this equilibrium will be slightly perturbed by inclusions that are further away. Similarly to rings, the non-neighbouring inclusions will perturb both the separation compared to the two-body equilibrium, and in particular, the anisotropy of the inclusions can generate frustration that alters the orientation that minimises the energy.

To visualise the structure of the aggregates, we construct a graph and associated 2D embedding for each configuration. Each inclusion is represented by a node in the graph, embedded at the inclusion location, and edges of the graph connect nearest neighbour inclusions, which we define to be inclusions closer than a distance of $1.3R^*$ apart. This threshold is chosen to capture the range of nearest neighbour interactions that were seen from the stable ring and line configurations, without connecting inclusions further away. In particularly, it is good for the threshold to be less than $\sqrt{2}R^*$ else diagonal inclusions in a square configuration may appear as nearest neighbours. Constructing this graph and visualising the edges, many of the aggregates formed were comprised of rings of aggregates that were positioned next to each other to form a lattice of polygons. Additionally, there were also stable configurations containing lines of inclusions that protruded out from the aggregate.

To sample some stable aggregates, we uniformly distributed 20 inclusions in a 60×60 box with random orientation and evolved the system until $t = 10^7$ for 100 different initial conditions. The ensemble of stable configurations that resulted are shown and plotted in Figure 3.12 as well as the square lattice with 20 inclusions (note that we align the semi-minor axis with ψ_i). The lower energy aggregates typically have a smaller footprint and we quantify this footprint as the area of the convex hull made from the inclusion locations. This sample of end configurations demonstrates the vast number of possible energy minima a system can evolve to when the initial inclusion distribution is unconstrained.

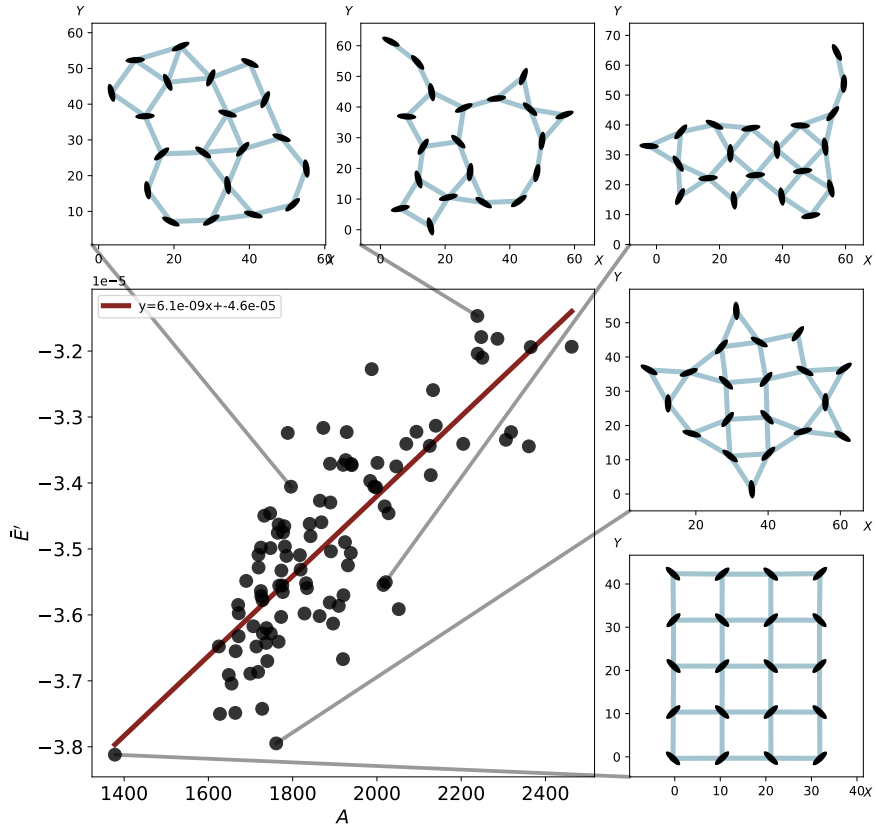

Figure 3.12: Sample stable configurations generated from an initial configuration of 20 inclusions. The graph structure described in the text is shown in light blue. The area, A, is the dimensionless area of the convex hull of inclusion locations. The regression demonstrates the relation ship between hull area and configuration energy. The inclusions are shown as ellipses with semi-minor axis aligned with ψ_i.

Aggregate Structure Depends on Initial Distribution

The final stable configuration of inclusions depends on the initial configuration. For example, for the case of interacting finite lines the resulting inclusion configuration can be a larger line or a ring, depending on how the initial lines are orientated. This idea holds more generally, and we see a strong dependence of the final stable configuration of inclusions on the initial inclusion configuration. A starting configuration that is closely packed together (still with the minimum separation between inclusions greater than $\tilde{R}$) will initially feel a strong repulsion from nearby

inclusions and the inclusions will spread out. During this process, the repulsion dominates, and transient triangular lattices with a lattice spacing less than R^* emerge. As the inclusions are forced to separate by this potential, the average inter-inclusion separation approaches R^* and the inclusions change orientation to minimise the interaction energy, forming a lattice with many rings of size four (similar to the square configuration seen earlier). In fact, depending on the initial starting configuration the inclusions can form a square lattice, chequerboard pattern of tangential and radial configurations (for an example see Figure 3.13).

In systems of many interacting inclusions, we expect that the square lattice will minimise the configuration energy. Each nearest neighbour will lower the interaction energy, since the two body contribution is negative. The square lattice is the 2D polygonal structure that maximises the number of compatible nearest neighbours and therefore minimises the energy. Not all combinations of regular polygons tile the plane and if they do, there is an additional geometric constraint on the orientation with adjacent polygons. For example, in a triangular lattice, there are six nearest neighbours, however any arrangement of inclusions will be unstable in some mode. This also means that the most dense lattice that can form is the square lattice and so when starting from a high density configuration, the system will encounter this minimum first during its relaxation to an equilibrium.

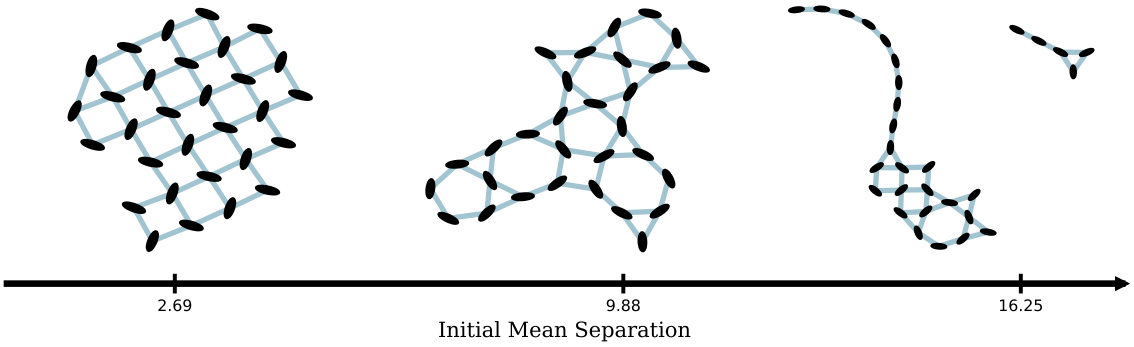

Figure 3.13: Examples of the different lattice structures formed from different initial mean nearest neighbours configurations. The initial mean distance to the nearest neighbour is shown on the axis in dimensionless units.

When inclusions are initialised further apart, all inclusions are initially attracted towards each other. The inclusions are attracted to closer inclusions more strongly and as such two inclusions will suddenly coalesce into the 2-body equilibrium configuration before coalescing with further single inclusions or group of previously coalesced inclusions. This process repeats to form aggregated structures, where groups of coalesced inclusions sequentially grow. In the very low density limit, the spacing between inclusions is very large, so that as they approach, the inclusions align and are appended onto the end of existing lines. Multiple inclusions coalescing at similar times or large lines of inclusions coalescing can perturb the finite lines and generate rings of inclusions. In this scenario the lines of inclusions will have grown significantly before forming rings and so the rings formed can be much larger than the small polygons ($n \lesssim 5$) typically seen for closer initial conditions. In Figure 3.13 the larger initial inclusion separations form lattices with larger rings, or linear protrusions.

Observed rings of inclusions formed from random configurations often result in the radial equilibrium. Again, when the inclusions are initialised at large separation, they will sequentially form a chain in the equivalent of a radial configuration. If the inclusions are perturbed by other inclusions in the system, then this line will collapse into a radial ring. Alternatively if multiple inclusions are initialised close together then the streamplot in Figure (3.9) shows that the basin of attraction for the radial configuration is larger than the tangential configuration and as such any rings formed will preferentially form radial rings.

3.6.4 Configurations of Multiple Inclusions

The interactions between small anisotropic inclusions can form stable lattice-like structures. Ultimately the quadrupole symmetry of the inclusions prevents the formation of a denser lattice, such as the triangular lattice, instead forming the polygonal lattices that balance the effective valence of inclusions with the geometric frustration. The square lattice is comprised of inclusions that form a chequerboard of alternating orientations, with $\psi_i = \psi_G + \pi/4$ and $\psi_G - \pi/4$ (where ψ_G is some

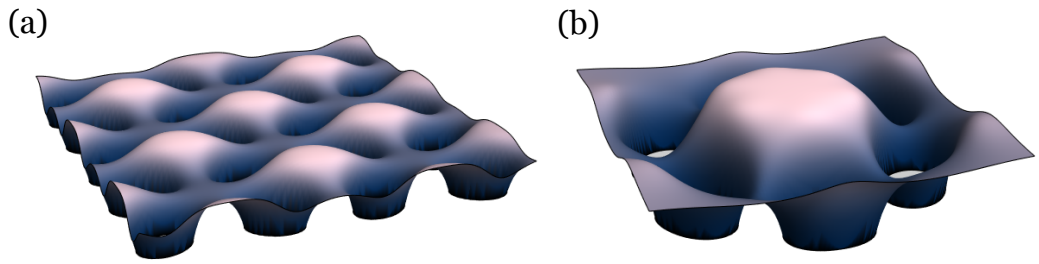

Figure 3.14: Examples of the surfaces generated by equilibrium configurations of inclusions with $\omega = 0.1$. (a) is an egg carton configuration of 20 inclusions and (b) is a ring of 6 inclusions. Note that the membrane has been truncated as it approaches a singularity around each inclusion.

global rotation of the lattice). Square lattices with similar alternating orientations have also been predicted but for isotropic curvature inducing inclusions, where adjacent inclusions have a flipped embedding in the membrane changing the sign of induced curvature [85].

Prior work has also identified lines and lattices as an important class of arrangements of curvature inducing inclusions for anisotropic inclusions. Experimental studies of BAR proteins show the formation of long end-to-end linear aggregates [90] and in membrane simulations anisotropic banana shaped proteins can form networks of inclusions [93], [94]. However in these simulations the edges of the network comprise of multiple (≈ 10) inclusions and membrane tubulation can be initiated at the nodes of this network which correspond to local clusters of inclusions. Lines, rings and lattices have also been observed in models with zero membrane tension where anisotropic point-like inclusions set the curvature tensor locally [95]. Typical equilibrium aggregates show stable structures as rings or lines of inclusions depending on the anisotropy of the inclusions and the induced curvature. Additionally, this model predicts the formation of a square-like lattice structures and these structures induce 'egg-carton' shaped deformations on the membrane such as the example in Figure 3.14(a) [95], [96]. Here we have shown that, similarly to the case of tensionless systems with close inclusions, square lattices can form at much larger separations in a membrane with strong tension and for finite sized inclusions. The lattice spacing is determined by the anisotropy parameter, ω, and the non-dimensional length,

μ, which scales the inclusion separations. Since $\mu \propto T^{-1/2}$ we expect the inclusion density to increase linearly with the tension. In synthetic, clamped membranes where the tension can be varied, this might serve as control mechanism for the density of curvature inducing inclusions.

Curvature induced anisotropic forces can also occur as a result of other substrate mediated interactions. For example, ellipsoids floating an oil and water can interact via an anisotropic interfacial deformation and this can lead to the formation of polygons of ellipses and linear end-to-end configurations [97]. However, unlike the structures studied here, the interfacial ellipses form lines and rings where the ends of the ellipses are in contact. This is because the interaction potential is always attractive and limited only by the finite ellipse size. Spherical colloids floating on an oil/water interface can also interact to form square lattices with a finite separation [98]. Rather than an anisotropic contact angle, a curved liquid interface can break the symmetry so that the interface must be deformed to maintain a constant contact angle on the colloid. Many interacting colloids then form a square lattice with a finite separation, where the orientation of the lattice aligns with the underlying interface curvature. When constrained to higher densities than the square lattice, triangular lattice begin to form as seen during the formation of lattices here.

3.7 Multi-Scale Model for Configurations

So far, we have only considered the dynamics of inclusions that are initialised sufficiently far apart, such that the equilibrium configurations explore the stable equilibrium around R^*. However, curvature inducing inclusions can combine to form dimers or larger oligomers [99] that are much closer together. Inspired by this observation, we explore structures formed when inclusions are initialised close together. Inclusions that are separated by a distance less that $\tilde{R}$ will be attracted to each other by the diverging interaction potential. This is not physical, as the inclusions cannot overlap and the interaction is expected to be repulsive for identical inclusions at close separations [85]. As the inclusions approach each other, the inclusions separation reduces and the characteristic length μ stops being $\mathcal{O}(1)$. In

this regime, we use the form of the two body interaction energy from a previous work [80] that determined the two body interaction energy when $\mu \sim \mathcal{O}(\epsilon^{-1})$. Indeed, the two body energy is repulsive at short distances due to an energy contribution of $\epsilon^2 \frac{4}{R^4}((\alpha_1^{(0)})^2 + (\alpha_2^{(0)})^2)$. Therefore, we include this term in the two-body interaction energy here to give

$$\begin{aligned}\bar{E}_2(R,\psi_1,\psi_2) = 2K_0(R) &+ 2\omega K_2(R)(\cos 2\psi_1 + \cos 2\psi_2) \\ &+ \omega^2 \cos(2(\psi_1-\psi_2))K_0(R) \\ &+ \omega^2 \cos(2(\psi_1+\psi_2))\left(K_4(R) - \frac{48}{R^4}\right) + \epsilon^2 \frac{8}{R^4}.\end{aligned} \tag{3.77}$$

This potential now diverges to positive infinity as $R \to 0$ (since $K_4(x) - 48/x^4 \sim -x^{-2}$ as $x \to 0$). Hence, for $\epsilon \ll 1$, there exists an equilibrium at small separation. The inclusions orientate to be perpendicular to the axis of separation (as before), but separated by a small distance R_c that depends on ϵ. Gradients in the energy are much steeper about this equilibrium, and the system's relaxation to equilibrium is therefore dominated by the energy landscape at small separations. Initially we will consider the dynamics of two inclusions that are in the collapsing regime and show that they rapidly converge to the close equilibrium separation, which we will call a *close pair*. Regardless of the additional inclusions farther away, these inclusions will stay separated by R_c.

We can describe the close pairs by the x, y and ψ coordinates describing each inclusion. However, similar to interacting particles in an external field, we can also describe these inclusions in a centre-of-mass coordinate system. In this frame, the external field is provided by the other far away inclusions which will exert a much smaller force on each inclusion in the pair compared to the force they experience from each other. A natural choice to parameterise the positional coordinates is therefore

$$\begin{aligned} x_c = \frac{x_1+x_2}{2}, \quad &\text{and} \quad y_c = \frac{y_1+y_2}{2} \\ r = \sqrt{(x_1-x_2)^2+(y_1-y_2)^2}, \quad &\text{and} \quad \theta = \arctan(y_1-y_2, x_1-x_2). \end{aligned} \tag{3.78}$$

where describing the orientation of the inclusion pair is useful as this will be coupled to the individual inclusion alignment. A convenient treatment of the orientations

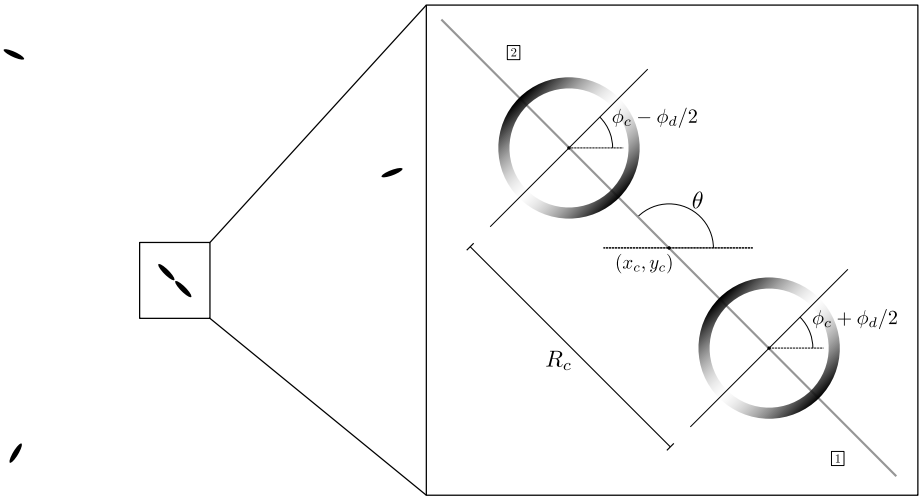

Figure 3.15: The parameterisation of a close pair of inclusions.

will be to consider the average and difference between the orientations of the two separate inclusions. We define

$$\begin{aligned} \phi_c &= \frac{1}{2}(\psi_1 + \psi_2) \\ \phi_d &= \psi_1 - \psi_2. \end{aligned} \tag{3.79}$$

Note that the values of ϕ_c and ϕ_d will depend on how ψ_1 and ψ_2 are measured, but this will not affect the resulting dynamics. Figure 3.15 shows this parameterisation diagrammatically.

The new set of coordinates highlights the slow and enslaved variables. From the steep potential around the close equilibrium separation we expect that to leading order $r = R_c$ and $\phi_d = 0$. We also expect that $\theta = \pi/2 + \phi_c$ and as such the pair of inclusions can be described by three slow variables. However, we still need to consider the gradients in ϕ_c or θ as they may dominate the dynamics. That is, we need to determine whether the rotation of the pair is limited by the translational motion of the inclusions or the rotation. Thus, simply setting $\theta = \pi/2 + \phi_c$ or $\phi_c = \theta - \pi/2$ may not capture the behaviour of the inclusion pair. To include both the translation and rotation of the individual inclusions when considering the motion of the pair, we take a linear combination of the two to eliminate the slow variable and define

$$\psi_c = \frac{\theta + \chi(\frac{\pi}{2} + \phi_c)}{1 + \chi} \quad \text{and} \quad \psi_d = \theta - \left(\frac{\pi}{2} + \phi_c\right), \tag{3.80}$$

where χ is to be determined. Thus ψ_c gives the overall orientation of the pair and we expect ψ_d to quickly relax to zero.

We write the overdamped dynamics in a compact form as

$$\frac{\mathrm{d}\mathbf{X}}{\mathrm{d}t} = -\mathbf{M}\frac{\mathrm{d}\bar{E}}{\mathrm{d}\mathbf{X}}, \tag{3.81}$$

where we define the coordinate vector $\mathbf{X} = (x_1, x_2, y_1, y_2, \psi_1, \psi_2)$ and the mobility matrix, $\mathbf{M} = \mathrm{diag}(\bar{\mu}_t, \bar{\mu}_t, \bar{\mu}_t, \bar{\mu}_t, \bar{\mu}_r, \bar{\mu}_r)$.

Defining the new coordinate vector, $\mathbf{Y} = (x_c, y_c, \psi_c, r, \psi_d, \phi_d)$ and the Jacobian matrix between these two coordinate systems, $\mathbf{J}$, the new variables will evolve as

$$\frac{\mathrm{d}\mathbf{Y}}{\mathrm{d}t} = -\mathbf{J}\frac{\mathrm{d}\mathbf{X}}{\mathrm{d}t} = \mathbf{J}\mathbf{M}\frac{\mathrm{d}\bar{E}}{\mathrm{d}\mathbf{X}} = -\underbrace{\mathbf{J}\mathbf{M}\mathbf{J}^{-1}}_{\mathbf{M}'}\frac{\mathrm{d}\bar{E}}{\mathrm{d}\mathbf{Y}}. \tag{3.82}$$

This gives the same evolution equation, but with a modified mobility matrix given by

$$\mathbf{M}' = \begin{pmatrix} \frac{\bar{\mu}_t}{2} & 0 & 0 & 0 & 0 & 0 \\ 0 & \frac{\bar{\mu}_t}{2} & 0 & 0 & 0 & 0 \\ 0 & 0 & \frac{\chi^2\bar{\mu}_r + \frac{4\bar{\mu}_t}{(x_1-x_2)^2+(y_1-y_2)^2}}{2(\chi+1)^2} & 0 & \frac{\frac{4\bar{\mu}_t}{(x_1-x_2)^2+(y_1-y_2)^2} - \chi\bar{\mu}_r}{2(\chi+1)} & 0 \\ 0 & 0 & 0 & 2\bar{\mu}_t & 0 & 0 \\ 0 & 0 & \frac{\frac{4\bar{\mu}_t}{(x_1-x_2)^2+(y_1-y_2)^2} - \chi\bar{\mu}_r}{2(\chi+1)} & 0 & \frac{\bar{\mu}_r}{2} + \frac{2\bar{\mu}_t}{(x_1-x_2)^2+(y_1-y_2)^2} & 0 \\ 0 & 0 & 0 & 0 & 0 & 2\bar{\mu}_r \end{pmatrix}. \tag{3.83}$$

Coupling θ and ϕ_c introduces off diagonal terms in the mobility matrix, that depend on the other coordinates in the system. However choosing $\chi = 4\bar{\mu}_t/(r^2\bar{\mu}_r)$ these off-diagonal terms vanish and at the pair equilibrium we expect, $r = R_c$ which is constant and therefore we take $\chi = 4\bar{\mu}_t/(R_c^2\bar{\mu}_r)$. The value of χ indicates whether the evolution of the orientation of the pair is limited by the rotation of each individual inclusion, or the by the translational motion. With this choice, the mobility matrix is diagonal,

$$\mathbf{M}' = \mathrm{diag}\left(\frac{\bar{\mu}_t}{2}, \frac{\bar{\mu}_t}{2}, \frac{2\bar{\mu}_r\bar{\mu}_t}{r^2\bar{\mu}_r + 4\bar{\mu}_t}, 2\bar{\mu}_t, \frac{\bar{\mu}_r}{2} + \frac{2\bar{\mu}_t}{r^2}, 2\bar{\mu}_r\right), \tag{3.84}$$

and we have a reduced system where we set $r = R_c$, $\psi_d = 0$, and $\phi_d = 0$. We can evolve the remaining three variables, describing the pair of inclusions using the overdamped dynamics and transformed mobilities.

In addition to the modified mobility, we need to calculate gradients of the energy in the reduced system. Using the general two body interaction energy $\bar{E}_2(R, \psi_a, \psi_b)$ we label a configuration of n inclusions with the inclusions 1 and 2 being in a close pair. The energy of the configuration with the pair is therefore

$$\begin{aligned}\bar{E}_{overall} = &\left(\sum_{i=3}^{n}\sum_{i=j+1}^{n}\bar{E}_2\Big(R_{ij}, \psi_i - \theta_{ij}, \psi_j - \theta_{ij}\Big)\right) + \bar{E}_2\Big(R_{12}, \psi_1 - \theta_{12}, \psi_2 - \theta_{12}\Big) \\ &+ \sum_{i=3}^{n}\left(\bar{E}_2\Big(R_{i1}, \psi_i - \theta_{i1}, \psi_1 - \theta_{i1}\Big) + \bar{E}_2\Big(R_{i2}, \psi_i - \theta_{i2}, \psi_2 - \theta_{i2}\Big)\right),\end{aligned} \tag{3.85}$$

where we split the interaction energy into contributions from inclusions not in the pair, inclusions in the pair, and an inclusion in the pair and interacting with an inclusion away from the pair.

The first term is unaffected by the coordinate transformation. The second term is the interaction between the two inclusions in the pair that drives the fast dynamics in the system, constraining the pair of inclusions to be at their equilibrium separation and orientation. This contribution can be written as $\bar{E}_2\Big(R_{12}, \psi_1 - \theta_{12}, \psi_2 - \theta_{12}\Big) = \bar{E}_2\Big(r, \pi/2, \pi/2\Big)$ which will be constant for the slow dynamics. For the final term in the energy, we note that the inclusions in the pair are close to x_c and y_c, that is $r \ll 1$, and so we can expand the energy around these points. For inclusion 1 this gives

$$\begin{aligned}&\bar{E}_2\Big(R_{i1}, \psi_i - \theta_{i1}, \psi_1 - \theta_{i1}\Big) = \\ &\quad \bar{E}_2\Big(R_{ic}, \psi_i - \theta_{ic}, \psi_c - \theta_{ic}\Big) + \left[\left(\frac{\partial \bar{E}_2}{\partial R}\frac{\partial R_{i1}}{\partial x_1} - \left(\frac{\partial \bar{E}_2}{\partial \psi_a} + \frac{\partial \bar{E}_2}{\partial \psi_b}\right)\frac{\partial \theta_{i1}}{\partial x_1}\right)\frac{r}{2}\cos\psi_c\right. \\ &\quad \left. + \left(\frac{\partial \bar{E}_2}{\partial R}\frac{\partial R_{i1}}{\partial y_1} - \left(\frac{\partial \bar{E}_2}{\partial \psi_a} + \frac{\partial \bar{E}_2}{\partial \psi_b}\right)\frac{\partial \theta_{i1}}{\partial y_1}\right)\frac{r}{2}\sin\psi_c\right]_{R=R_{ic}, \psi_a=\psi_i-\theta_{ic}, \psi_b=\psi_c-\theta_{ic}} \\ &\quad + \mathcal{O}(r^2),\end{aligned} \tag{3.86}$$

where $R_{ij} = \sqrt{(x_i - x_j)^2 + (y_i - y_j)^2}$ and $\theta_{ij} = \arctan(x_i - x_j, y_i - y_j)$. We can follow the same steps for inclusion 2 which gives an identical expansion except with $r \to -r$ and so the linear terms in the expansion exactly cancel out in the expansion.

We can now write the energy as

$$E_{overall} = \left(\sum_{i=3}^{n} \sum_{i=j+1}^{n} \bar{E}_2\Big(R_{ij}, \psi_i - \theta_{ij}, \psi_j - \theta_{ij}\Big) \right) + \sum_{i=3}^{n} 2\bar{E}_2\Big(R_{ic}, \psi_i - \theta_{ic}, \psi_c - \theta_{ic}\Big) + \mathcal{O}(r^2), \tag{3.87}$$

where the energy has been shifted by the self interaction energy of the inclusion pair. This procedure can be generalised so that the interaction of multiple pairs of inclusions can also be described, where two interacting pairs of inclusions contribute $4\bar{E}_2\Big(R_{ic}, \psi_i - \theta_{ic}, \psi_c - \theta_{ic}\Big)$ to the total interaction energy. Recall that we scaled the interaction energy by the magnitude of the monopole mode. An inclusion with the same asymmetry, but double the magnitude of the induced curvature would contribution twice as much to the interaction energy which is exactly the effect of the inclusion pair, up to $\mathcal{O}(r^2)$.

We conclude that *we can model a pair of inclusions as one single inclusion, with the same anisotropy but twice the monopole mode and a modified translational and rotational mobility.* The reduced mobility is also consistent with a larger induced deformation. The footprint of this deformation will be larger and so this might slow down the movement of the inclusion [100].

The reduced system can be used to evolve a random configuration of inclusions, that also includes pairs of inclusions that are close together. The pair-to-inclusion and pair-to-pair interactions have the same features as the inclusion-to-inclusion interaction and numerically evolving mixtures of pairs and inclusions leads to stable configurations with the same lattice structures. However, depending an the initial configuration a system containing a pair of inclusions might converge to a different final configuration when compared to single inclusions that are initialised with the same starting configuration due to the differences in mobilities.

3.8 Biological Regimes

A prominent feature of biological membranes is their diversity in composition. Membranes contain different lipids, cholesterol, or embedded proteins that might

modify the membrane bending stiffness locally [101], [102]. Rearrangements of lipid into ordered domains can cause increases in the bending stiffness of a membrane which can occur due to temperature changes, or large differential stress from bilayer asymmetry [103]. However, in addition to increasing bending stiffness, the bilayer asymmetry may induce a non-zero spontaneous curvature or the close packing in the ordered domain might significantly affect the mobility of inclusions. Lipid domains can cause macroscopic or nanoscopic patterning, depending on the composition of the membrane [104] which can therefore introduce significant heterogeneity on the length scale of inclusion separations, L. These ordered regions and the varied membrane composition could alter the biophysical properties of the membrane which would need to be reflected in a more detailed model. The membrane tension might also vary spatially within the membrane. For example, different mechanical stimuli have been shown to alter the membrane tension in different ways [105]. Pulling on the membrane will only locally change the tension, whereas larger mechanical stimuli that also engage the actin cortex will change the membrane tension globally on a cell membrane.

We now consider the magnitude of the elastic forces in biological systems of interacting proteins. Substituting (3.67) into (3.5) gives

$$E = \left(\xi\tilde{\alpha}^{(0)}\right)^2 \pi \left(\epsilon L\right)^2 T\bar{E}' \tag{3.88}$$

where we also used $\alpha^{(0)} = \epsilon\tilde{\alpha}^{(0)}$. The measured contact angle is $\xi\tilde{\alpha}^{(0)}$ and the structure of the BAR domain proteins gives $\xi\tilde{\alpha}^{(0)} \approx 0.4 - 0.8$ and a typical radius $\epsilon L \approx 10$nm [106]. The membrane tension in biological systems is typically about 0.5mNm^{-1} [107] although this can vary and rupture occurs at higher tensions [102]. Using a membrane bending stiffness of $60\text{K}_B\text{T}$ [96] and choosing $\mu = 1$ gives the typical length scale, $L = 20$nm and $\epsilon \approx 0.5$. Typical cells have radii of around $10^{-5} - 10^{-4}$m which are much larger than the proteins size scale and the length scale of the system. The size of the non-dimensional interaction energy for an aggregate of inclusions is typically 10^{-4} so that we find $|E| \approx 10^{-23}$J.

This lattice energy is less than typical thermal energy in the system $k_BT \approx 10^{-21}J$ and so for these biological systems thermal fluctuations will dominate. However the membranes can support significantly higher tensions (up to around 10mNm^{-1} [102]) that would increase the interaction energy from deformations. Larger inclusions, will also have a larger interaction energy and this could be relevant in colloidal systems where microparticles ($\epsilon L \approx 500$nm [108]) partially bind to lipid membranes, or during the binding of viral capsids ($\epsilon L \approx 35$nm [109]). Increasing the tension and inclusion radius will change the value of μ and ϵ and care must be taken that the system remains in the small inclusion, well separated regime studied here. This might additionally require an increased membrane bending stiffness which depends on, for example, lipid composition or cholesterol [101], [102].

In systems of larger inclusions and higher tensions, we might expect thermal fluctuations to induce transitions between configurations of inclusions. Additionally, fluctuation induced forces generate attractive forces with an interaction energy $\sim R^{-4}$ [110]. These forces and thermal fluctuations in the position of inclusions may induce a cascade through different energy configurations and ultimately into the energy minimising square lattice. The formation of the lattice could be a useful control mechanism in the design of different functional synthetic membranes with large bending stiffnesses.

3.9 Discussion

This work has focused on a specific limit of the membrane mediated interaction between curvature inducing inclusions: when the inclusions induce small curvatures and when the inclusions are far apart. This is a previously understudied regime, with many models considering inclusions that are much closer together. In the well separated limit considered here, the larger scale elastic deformations are more prevalent compared to the near field interactions, such as volume exclusion effects, or changes to the bilayer thickness from the protein binding (we expect this variation to decay exponentially with oscillatory term) [111].

The anisotropy of the inclusions fundamentally changes the interaction by the introduction of an equilibrium separation, rather than infinite repulsion for the symmetric case. Furthermore, the anisotropy has an effect in the formation of aggregates of inclusions. Typically, an interaction with an equilibrium separation, but no orientation dependence will form a triangular packing however this can induce geometric frustrations if the interaction depends on how the particles are aligned, which is again due to the anisotropy. In fact, the formation of the polygonal lattices observed here could be general to any potential with a monopole-quadrupole or quadrupole-quadrupole interaction.

Using the interaction energy between well-separated inclusions and a repulsive correction term at very short distances, we developed an effective model to describe the dynamics of close inclusion pairs. Additionally, we could consider larger clusters of inclusions, for example three inclusions close together, and try to determine a reduced model in this case. However this work studies the limit of low inclusion density, which typically results in well separated inclusions. Random configurations of inclusions may have multiple inclusions within $\tilde{R}$ of each other, but this is unlikely and the likelihood decreases for larger groups close inclusions.

Introducing a correction term for close inclusions maintains the property that the total energy in the system is the sum of the pairwise interactions for all inclusions. However, for nearby inclusions we expect a significant multi-body contributions to the interaction energy [84]. This could affect the separation of the close pair, or additionally introduce a significantly different membrane deformation in the inner region and therefore change the interactions with far away external inclusions. A significantly different local deformation around the inclusions may also directly affect the inclusion mobility and response to forces in the membrane. For example, diffusion properties of embedded transporter proteins can change when the conformation of the protein changes [112]. This could be connected to the locally induced curvature and so changing the confirmation would change the local membrane shape and therefore the transport properties of the inclusion.

Mean field descriptions of systems comprised of anisotropic curvature inducing particles have been developed in the past [77], [113]. Such theories aim to describe the key features of the system as a function of some order parameter that depends on average behaviour within a region. These might include excluded volume interactions between elliptical inclusions, or membrane-inclusion interactions due curvature to mismatch. The aim of these descriptions is to model the distribution of particles using the average direction without tracking each individual particle. However in the lattices studied here, we find that in the aggregates of inclusions the alignment of inclusions varies between neighbouring inclusions and this variation depends on the lattice formed. Models of a director field would therefore need to keep track of every inclusion and this would limit the ability of the model to describe a larger number of inclusions. In the ring configurations that comprise the lattice, inclusions are placed at equally spaced angles. We therefore expect the distribution of angles from a very large lattice to be uniform over angle and as such, the average induced curvature of the aggregate will be the monopole mode. At this scale, the continuum models of isotropic curvature may still provide a useful description for a much broader class of inclusions (even those with anisotropy).

4

Protein Aggregation in Disease

Contents

4.1 Introduction 92
4.2 Background 92
4.2.1 Aggregating Neurodegenerative Disease 93
4.3 Aggregation Kinetics in vitro 93
4.3.1 Failure to Describe Features of Disease 98
4.4 Aggregation Kinetics in vivo 101
4.4.1 Unbounded Clearance 102
4.4.2 Bounded Clearance 106
4.4.3 Reduced Models of in vivo Aggregation 109
4.5 Generalising the Dynamics 113
4.5.1 Generalised Models of Clearance 113
4.5.2 Exponential Growth is Unphysical 115
4.5.3 Non-Conserved Monomer 117
4.5.4 Length Dependent Seeding 118
4.5.5 Length Dependent Clearance 119
4.6 Transitions to Disease and Therapeutic Scenarios . . . 121
4.6.1 Ageing reduces Clearance 122
4.6.2 Explaining Genetic Susceptibility 123
4.6.3 Rational Therapeutic Design 124
4.7 Summary and Conclusions 127

4.1 Introduction

Effective treatments for neurodegenerative diseases require a mechanistic understanding of the onset and progression of disease. The reaction kinetics that form toxic aggregates associated with disease are well understood in test tube experiments, but this understanding does not translate well to the disease in humans. Prior work has tried to extend these models into living systems by including aggregate removal processes. However, so far, this work has only considered unphysical aggregate removal mechanisms. In this chapter, I will review the existing tools to describe the kinetics of aggregation and then extend these models to include physically motivated aggregate removal processes. I will show how these physically motivated removal processes can explain many features of human disease and I will discuss how to harness this understanding for the design of rational therapeutics.

4.2 Background

Protein-protein interactions, while crucial for normal cellular function, can also be the underlying cause of disease. This can occur in two main ways: (a) by interfering with the proteins' normal function, or (b) by causing proteins to adopt a toxic mode of action. A notable example of this is found in diseases associated with protein aggregation. In these diseases, proteins aggregate into large, typically linear structures known as fibrils, where multiple monomer proteins combine in an ordered fashion [15]. These aggregates can contribute to disease through both mechanisms mentioned: (a) by sequestering functional proteins, thereby reducing the concentration of free monomers available for normal cellular functions, and (b) by producing reactive, toxic oligomers [15], [16]. Oligomers are small, partially structured protein aggregates, including intermediaries in the formation of fibrils. These oligomers can undergo internal structural reorganisation, forming short, ordered aggregates that then attract additional monomers, eventually maturing into long fibrils composed of thousands of monomers. There are still many open questions around the exact mechanisms by which oligomers cause cellular

dysfunction, however the toxicity of oligomers has been shown to correlate with the exposure of hydrophobic groups [114] and oligomer size [16]. Perhaps the reactivity and small size of oligomers means they can explore the cellular environment and disrupt various cellular processes.

4.2.1 Aggregating Neurodegenerative Disease

Protein aggregation that occurs in the brain can trigger the progressive loss of neurons and neurodegenerative diseases (NDDs). Individuals with NDDs can experience symptoms of dementia, including gradual memory loss and ultimately loss of independent function [115]. Alzheimer's disease (AD) is the most common cause of dementia worldwide, estimated to affect 24 million people globally with prevalence increasing in later life [116]. AD neuropathology has two main features; extracellular amyloid plaques and intracellular neurofibrillary tangles. These are aggregates of amyloid-beta (Aβ) which is a cleavage product of the amyloid precursor protein and the microtubule-associated protein tau respectively.

In addition to AD, a variety of other NDDs are associated with aggregates of different proteins, for example, prion diseases, Parkinsons Disease (PD), Huntingtons's Disease, and amyotrophic lateral sclerosis (ALS) [15], [16]. The molecular structure of the different proteins and the aggregates differs between diseases, however descriptions of the aggregation kinetics can unify our understanding of the development of pathologies across diseases [117].

4.3 Aggregation Kinetics in vitro

There are multiple processes that can convert protein monomers into ordered aggregates. We model these aggregates as 1D chains of the monomer protein which can vary in length and describe an aggregate of length i as $\mathcal{A}_i$, and the concentration of aggregates of size i is given by p_i. We describe the monomers as $\mathcal{M}$ and the monomer concentration as m. There are typically three distinct mechanisms that can form new aggregates and these are discussed below and shown in Figure 4.1.

- **Primary Nucleation** is the spontaneous conversion of n_c monomers into an aggregate of length of n_c: $n_c\mathcal{M} \rightarrow \mathcal{A}_{n_c}$. Using mass action, we expect the rate of this reaction to be $k_n m^{n_c}$ where k_n is the rate constant for this process. We expect that n_c is set by the energy dependence on aggregate length and so n_c is constant and all aggregates smaller than n_c are unstable and subsequently have negligible concentration.

- **Secondary Nucleation** is an autocatalytic conversion of n_2 monomers into an aggregate of length of n_2 occurring on the surface of existing aggregates: $n_2\mathcal{M} + \mathcal{A}_i \rightarrow \mathcal{A}_{n_2} + \mathcal{A}_i$. This reaction occurs uniformly over the surface (i.e. length) of all existing aggregates and so we expect the rate to be proportional to the total length of aggregates, $\sum ip_i$. The reaction rate then becomes $k_2 m^{n_2}(\sum ip_i)$ where k_2 is the rate constant for secondary nucleation. Note that we set $n_2 \geq n_c$ as smaller aggregates would not be stable.

- **Fragmentation** is the splitting of a longer aggregate into two smaller aggregates: $\mathcal{A}_{i+j} \rightarrow \mathcal{A}_i + \mathcal{A}_j$. Again, we assume that fracturing occurs uniformly over every bond between monomers, so that for an aggregate of size i, there are $i-1$ bonds that could fracture. The rate for a specific bond to fracture will be some constant rate, k_-, however the overall fracture rate of aggregates of size i will be $k_-(i-1)p_i$. When an aggregate fractures it forms two new smaller aggregates and so increases the number of aggregates.

Additionally, aggregates change size via the addition or removal of a monomer protein on the end of an aggregate, we describe this process as:

- **Elongation** is the addition of a monomer onto an existing aggregate: $\mathcal{M} + \mathcal{A}_i \rightarrow \mathcal{A}_{i+1}$. This happens at a rate proportional to the number of aggregate ends ($2p_i$) and the monomer mass m to give the overall elongation rate of aggregates of size i to size $i+1$ is $2k_{\text{on}}mp_i$.

- **Depolymerisation** is the dissociation of a monomer from an existing aggregate: $\mathcal{A}_i \rightarrow \mathcal{M} + \mathcal{A}_{i-1}$. This process happens at rate $2k_{off}p_i$.

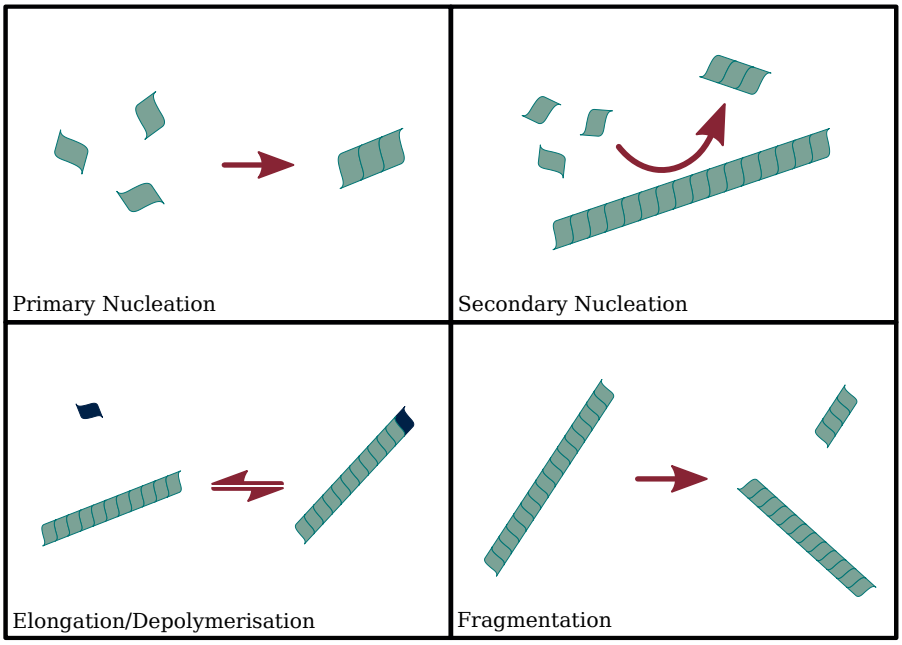

Figure 4.1: Schematic of different aggregation Processes.

Combining all of these processes gives the master equation that describes the evolution of the population of aggregates of a given length i,

$$\begin{aligned}\frac{\mathrm{d}p_i}{\mathrm{d}t} &= \delta_{i,n_c} k_n m^{n_c} + \delta_{i,n_2} k_2 m^{n_2} \left(\sum_{j=n_c}^{\infty} j p_j \right) + 2k_{\mathrm{on}} m (p_{i-1} - p_i) \\ &\quad + 2k_{\mathrm{off}}(p_{i+1} - p_i) - k_-(i-1)p_i + 2k_- \left(\sum_{j=i+1}^{\infty} p_j \right)\end{aligned} \tag{4.1}$$

and, if the total monomer in the system is conserved then $\mathrm{d}m/\mathrm{d}t = -\sum_i i \mathrm{d}p_i/\mathrm{d}t$, which is

$$\begin{aligned}\frac{\mathrm{d}m}{\mathrm{d}t} &= -n_c k_n m^{n_c} - n_2 k_2 m^{n_2} \left(\sum_{i=n_c}^{\infty} i p_i \right) - 2k_{\mathrm{on}} m \left(\sum_{i=n_c}^{\infty} p_i \right) \\ &\quad + 2k_{\mathrm{off}} \left(\sum_{i=n_c+1}^{\infty} p_i \right) + 2n_c k_{\mathrm{off}} p_{n_c}.\end{aligned} \tag{4.2}$$

The final term in (4.1) describes the rate at which new aggregates are made by fragmentation and has an additional factor of 2. This is because an aggregate of length $j > i$ can split at two different points to form an aggregate of length i, either at the i^{th} or $(j-i)^{\mathrm{th}}$ monomer. Exceptionally, when $j = 2i$ there is only one place where the aggregate can break to produce aggregates of length i, however this produces two aggregates of length i, $\mathcal{A}_{2i} \to 2\mathcal{A}_i$, and so the rate maintains

the factor of 2. In general, this infinite system of coupled ordinary differential equations is hard to solve. Strategies to numerically integrate the system involve truncating the series of p_is and introducing some boundary conditions in the length space, e.g. introducing an absorbing boundary, or by setting the population of very large aggregates to be zero.

A convenient way to describe the system is to consider the moments of the aggregate length distribution. The η^{th} moment of the aggregate length distribution is given by

$$Q^{(\eta)} = \sum_{i=n_c}^{\infty} i^{\eta} p_i. \tag{4.3}$$

Two particularly important moments (so important that we give them special names) are the total number concentration of aggregates, $P = \sum p_i$ and the total aggregate mass concentration, $M = \sum i p_i$. These are the 0th and 1st moments respectively. Summing over the master equation (or differentiating M), we can find the evolution of the moments during the aggregation process

$$\begin{aligned}\frac{\mathrm{d}M}{\mathrm{d}t} = 2k_{\text{on}}mP + n_c k_n m^{n_c} + k_2 m^{n_2} M - 2k_{\text{off}}P - 2(n_c-1)k_{\text{off}}p_{n_c} \\ - k_- n_c(n_c-1)P\end{aligned} \tag{4.4}$$

$$\frac{\mathrm{d}P}{\mathrm{d}t} = k_n m^{n_c} + k_2 m^{n_2} M - 2k_{\text{off}}p_{n_c} + k_- M - k_- n_c(n_c-1)P. \tag{4.5}$$

Experimental methods cannot typically determine the full distribution describing the number of aggregates at each length and so often only these first two moments are experimentally accessible. Additionally, when P and M describe a closed system of equations we can get insight into the aggregation process by studying these two quantities without worrying about the aggregate length distribution. However, (4.4) and (4.5) still depend on the concentration of the smallest aggregate, p_{n_c}. Since we typically expect that only a very small fraction of the total aggregate mass made up of the smallest aggregates, $n_c p_{n_c} \ll M$ and as a consequence, this term can be ignored in the moment equations [118]. Remarkably, the terms arising from the fragmentation and the other microscopic processes result in a closed set of equations that depend only on the first two moments, M and P.

Moving forward in this thesis, we focus on the situation that occurs when $k_- = k_{\text{off}} = 0$. This is a system that does not fragment or depolymerise, a model that describes stable aggregates, perhaps from a high monomer binding energy. Such a system will produce long growing aggregates and thus will isolate the effects of aggregate removal mechanisms that we will explore later in this chapter. The system is then described by

$$\frac{\mathrm{d}M}{\mathrm{d}t} = 2k_{\text{on}}mP + n_{\text{c}}k_n m^{n_{\text{c}}} + n_2 k_2 m^{n_2} M, \tag{4.6}$$

$$\frac{\mathrm{d}P}{\mathrm{d}t} = k_n m^{n_c} + k_2 m^{n_2} M. \tag{4.7}$$

To fully close the system we also need to consider the monomer concentration. In test tube experiments, there is a fixed quantity of monomer that is converted into aggregates. The total protein in an experiment is constant, $M_{total} = M + m$, so that $\dot{m} = -\dot{M}$ (where the dot is a derivative with respect to time). For completeness we write this explicitly as

$$\frac{\mathrm{d}m}{\mathrm{d}t} = -2k_{\text{on}}mP - n_{\text{c}}k_n m^{n_{\text{c}}} - n_2 k_2 m^{n_2} M. \tag{4.8}$$

Standard numerical solvers can integrate this closed system of equations to determine the *aggregation curve* that describes the transition from monomer to aggregate and in some circumstances approximate solutions can be derived and fitted [119]. Additionally, the aggregation curve can be observed experimentally. A well established method is to use the dye Thioflavin T which can bind to amyloid fibrils and results in increased intensity in fluorescence and a shift in wavelength [120], [121]. The change in this spectrum can therefore quantify the concentration of aggregates in a sample at different times, and thus we can *watch* the overall aggregation process. Fitting this data to the numerical solutions of (4.6)-(4.8) gives an accurate description of the in vitro kinetics and can be used to determine the rate constants of aggregation, e.g. k_{on}, k_2 etc. An example of an experimental aggregation curve and the fitting is shown in Figure 4.2.

Typical aggregation shows an initial exponential increase in aggregate concentration due to the secondary nucleation process. As the monomer concentration is

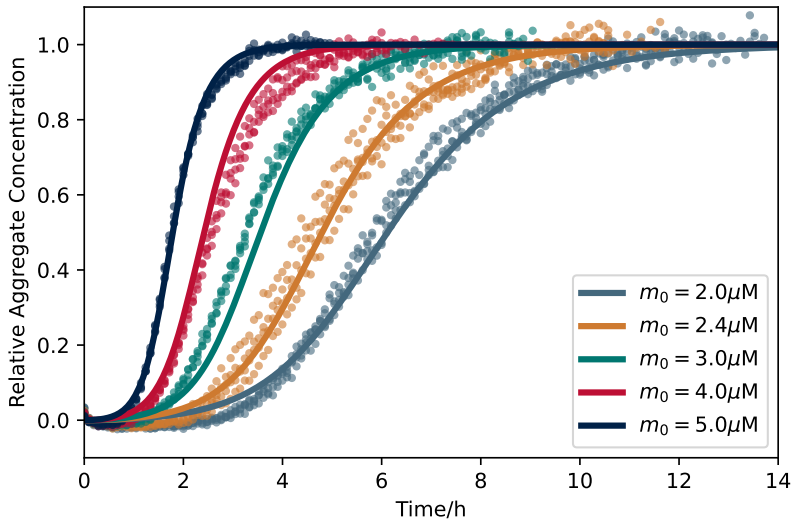

Figure 4.2: Fitting in vitro aggregation data. The rate constants have been fit globally. We set $n_c = 2$, $n_2 = 2$ and the fit gives $k_{on}k_2 = 5.60 \times 10^{16}\text{M}^{-2}\text{hr}^{-2}$ and $k_{on}k_n = 9.992 \times 10^{8}\text{M}^{-2}\text{hr}^{-3}$. Fitting has been done using *AmyloFit* software [119] using a secondary nucleation model (see the SI of [119]) so that only the parameter combinations can be determined. Data taken with permission from [122].

depleted the rate of aggregation slows until all the monomer is aggregated. The secondary nucleation step is autocatalytic as aggregates speed up the formation of more aggregates leading to a positive feedback and fast transition from mostly monomer to mostly aggregate.

4.3.1 Failure to Describe Features of Disease

The aggregation curves in test tube experiments are well understood by the reaction kinetics, but lack many crucial features of the development of neurodegenerative disease in living systems. Specifically, the model in (4.6)-(4.8) does not permit the discrete seeding transition, observed recovery of mice following treatment, or explain why the disease typically occurs in later life. These observations and the contradiction with the in vitro model are outlined below. Subsequent sections will explore the additional processes that occur in living systems and how this affects aggregation.

Discrete Seeding Transition to Disease

In some model systems of neurodegenerative diseases, aggregation is only observed when the tissue or cells are seeded [123], [124]. For example, pathological aggregates are only observed in hippocampal slice cultures from P301S tau transgenic mice when the system is exposed to a high concentration of preformed assemblies at some earlier time (seeding) [123]. Small doses of tau assemblies do not increase aggregate concentration when compared to an unseeded system. However, for large doses of tau assemblies, the observed aggregate concentration was increased (and further increased when the dose was increased again). This phenomenon is well established [125] and has been used to develop reporter lines assays to determine the presence of aggregates.[126]

The in vitro dynamics cannot explain this phenomenon. The in vitro early time aggregation is dominated by an exponential growth, from the secondary nucleation process, $M(t) \sim M_0 \exp(k_2 m_0^{n_2} t)$ where M_0 is the aggregate population at time $t = 0$. Thus, addition of a seeding mass of aggregates, M_S, would correspond to shifting the aggregation process in time, but would not cause this transition between a stable monomer system and an aggregating system at some non-zero seeding.

Explaining and Informing Treatments

Currently the leading therapeutics for neurodegenerative diseases are based on immune therapies, such as monoclonal antibody therapies. Particularly promising drugs include lecanemab [127] donanemab [128] and aducanumab [129]. In these treatments, antibodies bind to pathological fibrils to either disrupt the toxicity, or identify the structures for destruction via immune processes [3], [130]. However, these immune processes do not occur in test tubes and so cannot be described or explored using in vitro models.

More recently, short, synthetic, single-stranded DNA or RNA molecules, called antisense oligonucleotides (ASOs) are being explored as therapeutic candidates to treat NDDs [131]. The ASOs bind to target mRNA and thus limit transcription, reducing the expression of the aggregating monomer protein. In multiple studies,

injections of ASOs were able to reduce the monomeric protein and this led to reduction and even removal of aggregates in the brain [132]–[134]. These studies demonstrate the enormous clinical potential of ASOs that target tau and α-synuclein, two aggregating proteins associated with PD and AD. More sophisticated epigenetic editor technology is being developed to lower monomer concentration for prion diseases [135] and modification of the monomer concentration presents a major opportunity to develop effective treatments for NDDs.

However, in order to realise these therapeutic opportunities, it is necessary to understand the different processes that affect the development of the disease in living cells and tissues. Test tube experiments show an inevitable conversion of monomer into aggregates, and cannot capture the behaviour responsible for the reduction of aggregates and associated recovery of brain function in treated mice [132]. Furthermore, developing a quantitative theory that can describe the onset and progression of disease will be able to predict the size of effects required for an intervention to have a meaningful change in prognosis.

Long timescale in disease

Test tube aggregation kinetics provide estimations for typical aggregation parameters and timescales. Typical aggregation experiments, such as those shown in Figure 4.2, approach completion after around 10 hours, and have a doubling time of around an hour during the early exponential growth phase [136]. However, this understanding does not translate to the onset of disease in human populations. Around one in ten adults over the age of 65 have AD, increasing to four in every ten adults over 95 [137], and the doubling time for tau aggregates in human populations was estimated to be $\sim$ 5 years [138]. This late age of onset is also seen for PD and ALS, with only 4% of PD cases being under the age of 50 and the incidence increasing by a factor of 5–10 from cases in their fifties to eighties [139], [140]. This disparity of five orders of magnitude (one hour to one decade) clearly shows that something is missing from the current mechanistic models mapping in vitro protein aggregation kinetics onto the development of disease.

4.4 Aggregation Kinetics in vivo

In living systems, there are additional processes in the 'life cycle' of a protein: specifically how proteins are manufactured and removed. Many proteins that aggregate during disease are functional, for example microtubule-associated protein tau can stabilise microtubules and regulate transport by molecular motors [2], as well as causing tauopathy in AD. As such, we expect the concentration of these proteins will be maintained as part of homeostasis and thus in vivo the monomer concentration is constant, $m(t) = m_0$. In order to maintain the monomer concentration precisely, the cellular production and removal will need to be much faster than the aggregation kinetics and thus we write this as

$$\frac{\mathrm{d}m}{\mathrm{d}t} = \epsilon^{-1}\left(\gamma - \lambda_1 m\right) + \text{aggregation kinetics} \tag{4.9}$$

where γ and λ_1 are scaled rate constants for production and removal of the monomer respectively and ϵ is a small parameter that separates the timescales. The leading order solution to (4.9) is $m = \gamma/\lambda_1$ which sets m_0. In the subsequent analysis we only consider this leading order behaviour. A full solution as an expansion in ϵ could be explored, however the leading order behaviour is sufficient to capture key features of the disease at this stage.

In living systems aggregates can also be removed via active processes in the cells or surrounding tissue, for example by autophagy or removal by lymph flow. This changes the master equation to

$$\frac{\mathrm{d}p_i}{\mathrm{d}t} = \delta_{i,n_C} k_n m^{n_C} + \delta_{i,n_2} k_2 m^{n_2} \left(\sum_{j=n_c}^{\infty} j p_j\right) + 2k_{\mathrm{on}} m(p_{i-1} - p_i) - \lambda_i(p_i), \tag{4.10}$$

where $\lambda_i(p_i)$ is the clearance rate for aggregates of each size. The functional form of the clearance could also depend on other quantities, such as the concentration of aggregates of other lengths, or the monomer concentration, however we write it as $\lambda_i(p_i)$ here for simplicity.

4.4.1 Unbounded Clearance

The exact mechanisms of clearance and their kinetics remain unknown in many living systems. In the spirit of Occam's (or informally OCIAM's) razor, we begin by considering the simplest kinetics: the clearance rate is proportional to the number of aggregates and independent of size so that $\lambda_i(p_i) = \lambda \times p_i$. We initially develop and study this simple model, but consider more complex clearance kinetics in subsequent sections.

The moment equations now define a linear system, since $m = m_0$ is constant, and so we can define $\mathbf{q} = (P, M)^{\mathrm{T}}$ and the evolution of the system becomes

$$\dot{\mathbf{q}} = \underbrace{\begin{pmatrix} -\lambda & k_2 m_0^{n_2} \\ 2k_{\mathrm{on}} m_0 & n_2 k_2 m_0^{n_2} - \lambda \end{pmatrix}}_{\mathbf{A}} \mathbf{q} + \underbrace{\begin{pmatrix} k_n m_0^{n_c} \\ n_c k_n m_0^{n_c} \end{pmatrix}}_{\mathbf{b}} \tag{4.11}$$

where the dot indicates the time derivative and we'vewe defined the matrix $\mathbf{A}$ and vector $\mathbf{b}$ in the equation. The solution is

$$\mathbf{q} = -\mathbf{A}^{-1}\mathbf{b} + \left(\mathbf{q}_0 + \mathbf{A}^{-1}\mathbf{b}\right) e^{\mathbf{A}t} \tag{4.12}$$

where $\mathbf{q}_0$ is a vector of the initial aggregate number and aggregate mass concentration. The steady state behaviour is determined by the eigenvalues of $\mathbf{A}$, which are

$$\nu_{\pm} = \frac{1}{2}\left(k_2 m_0^{n_2} n_2 \pm \sqrt{8k_{\mathrm{on}} m_0 k_2 m_0^{n_2} + \left(n_2 k_2 m_0^{n_2}\right)^2} - 2\lambda\right). \tag{4.13}$$

The system always has $\nu_- \leq 0$, however the sign of ν_+ depends on the the clearance constant, λ. If $\nu_+ > 0$, then the system has no steady state and both the mass and number of aggregates have unbound growth. For $\nu_+ < 0$ then there exists a steady state solution for $t \to \infty$, $\mathbf{q}_\infty = -\mathbf{A}^{-1}\mathbf{b}$. The stability of the system is independent of the primary nucleation rate as this processes occurs at constant rate, however the nucleation process still affects the steady state aggregate mass. Given a set of rate constants we can therefore define a *critical clearance*, λ_{crit}, that determines whether the aggregation will be bound. Solving (4.13) for $\nu_+ = 0$ gives

$$\lambda_{\mathrm{crit}} = \frac{1}{2}\left(k_2 m_0^{n_2} n_2 + \sqrt{8k_{\mathrm{on}} m_0 k_2 m_0^{n_2} + \left(n_2 k_2 m_0^{n_2}\right)^2}\right). \tag{4.14}$$

When $\lambda > \lambda_{\text{crit}}$ the system approaches a steady state and when $\lambda < \lambda_{\text{crit}}$ the mass of aggregates grows exponentially as $M(t) \sim M(0)e^{\nu_+ t}$.

Alternatively, we could fix the clearance rate and determine the maximum monomer concentration, m_0, that leads to a steady state solution. The critical stability condition is

$$-2k_2k_{\text{on}}m_0^{n_2+1} - n_2k_2\lambda m_0^{n_2} + \lambda^2 = 0 \tag{4.15}$$

which has exactly one positive solution that defines the critical monomer concentration $m_0^{(\text{crit})}$. At monomer concentrations above $m_0^{(\text{crit})}$ the system has unbound aggregation and below $m_0^{(\text{crit})}$ the aggregate mass approaches a steady state. This is a useful perspective as the new treatment technologies treatments can vary m_0 as a therapeutic strategy, however currently no theoretical description exists to capture this behaviour.

We can determine the average aggregate length as the ratio of the aggregate mass and aggregate number, $\bar{l} = P/M$. At the steady state this will be

$$\bar{l}^* = \frac{M^*}{P^*} = \frac{2k_{\text{on}}m_0 + n_{\text{c}}\lambda_{\text{crit}}}{\lambda_{\text{crit}} + (n_{\text{c}} - n_2)k_2m_0^{n_2}}. \tag{4.16}$$

The effect of secondary nucleation on the average length initially seems confusing, and in particular it might seem strange that the dependence on k_2 vanishes when $n_{\text{c}} = n_2$. This can be explained as aggregates are only nucleated at length n_{c} or n_2 and the population of aggregates at other lengths decays geometrically away from these source terms. In the specific situation when $n_{\text{c}} = n_2$ there is only one source term, therefore the average aggregate length is determined entirely by the rate of decay of the aggregate population with increasing length. If the nucleation rate were increased, the population at length n_c would increase, and subsequently the population of aggregates of every length would increase proportionally, however the decay length would remain the same and the *average* aggregate length would also be unchanged. For $n_2 > n_{\text{c}}$ the source term at n_2 increases the aggregate population at large lengths and so increases the average length.

Exactly Solving the Full Linear System

When the system clears aggregates at a rate proportional to the aggregate concentration we can calculate the steady state aggregate length distribution as well as the time evolution of an arbitrary number of moments of this distribution. The evolution of an arbitrary moment space is given by

$$\frac{\mathrm{d}Q^{(\eta)}}{\mathrm{d}t} = n_C^{\eta} k_n m^{n_C} + n_2^{\eta} k_2 m^{n_2} M + \sum_{\tau=0}^{\eta-1} 2k_{\mathrm{on}} m \binom{\eta}{\tau} Q^{(\tau)} - \lambda Q^{(\eta)}. \tag{4.17}$$

Since the evolution of a moment only depends on itself, orlower order moments, we can still solve the system given by (4.11).

It is also possible to find p_i for the steady state and we demonstrate this here for $n_{\mathrm{c}} = n_2$. In steady state the concentration of each aggregate size is in detailed balance with the concentration of aggregates of other lengths so for the smallest aggregates, of length n_c, we have

$$k_n m_0^{n_{\mathrm{c}}} + k_2 m_0^{n_{\mathrm{c}}} M - 2k_{\mathrm{on}} m_0 p_{n_{\mathrm{c}}} - \lambda p_{n_{\mathrm{c}}} = 0 \tag{4.18}$$

and detailed balance for all aggregates of other lengths gives

$$(2k_{\mathrm{on}} m_0 + \lambda) p_{i+1} = 2k_{\mathrm{on}} m_0 p_i. \tag{4.19}$$

This is solved by

$$p_i = \alpha^{i-n_{\mathrm{c}}} p_{n_{\mathrm{c}}} \quad \text{with} \quad \alpha = \frac{2k_{\mathrm{on}} m_0}{2k_{\mathrm{on}} m_0 + \lambda} \tag{4.20}$$

and so we get another equation connecting M and $p_{n_{\mathrm{c}}}$, that is

$$M = \sum_{i=n_{\mathrm{c}}}^{\infty} i\alpha^{i-n_{\mathrm{c}}} p_{n_{\mathrm{c}}} = p_{n_{\mathrm{c}}} \left(\frac{(\lambda + 2k_{\mathrm{on}} m_0)(2k_{\mathrm{on}} m_0 + \lambda n_{\mathrm{c}})}{\lambda^2} \right). \tag{4.21}$$

Combining (4.18) and (4.21) gives the same mass, M, as from $\mathbf{q}_\infty$ and

$$p_{n_{\mathrm{c}}} = \frac{\lambda^2 k_n m_0^{n_{\mathrm{c}}}}{(2k_{\mathrm{on}} m_0 + \lambda n_{\mathrm{c}}) \left(\lambda^2 - k_2 m_0^{n_{\mathrm{c}}} (2k_{\mathrm{on}} m_0 + \lambda n_{\mathrm{c}})\right)} \tag{4.22}$$

which for realistic signs of the parameters (e.g. no negative clearance) gives the critical behaviour at the same values as before (for the specific case of $n_{\mathrm{c}} = n_2$).

Numerical Solution

Moving from the master equation to the moment description of the kinetics, we have assumed the system can support infinite aggregates and, for depolymerising systems, that $n_c p_{n_c} \ll M$. Numerical simulation of the dynamics of the system at the level of the master equation can verify this coarse grained description provides an accurate summary and prediction of the kinetics. Simulating an unbound upper aggregate length presents computational challenges, and so here, we introduce a maximum aggregate length that does not grow by elongation but is still removed via the clearance mechanisms. In fact this makes sense as cells have some finite size and so cannot support infinitely long aggregates. We use typical values from in vitro measurements, such as those reported by Thompson, Meisl, Knowles, *et al.* [141]. These values also give relevant phenomena occurring at physiological concentrations, for example protein and mass concentrations of $\sim 10^{-6} - 10^{-5}$M.

We simulate the system by explicitly evolving the aggregate population at each length i for i from n_c to $N + n_c$, where N is a simulation parameter. We prescribe some initial length distribution at time $t = 0$ and the system is evolved using a fourth order Runge Kutta method that explicitly updates the aggregate population at each length at time intervals of $\mathrm{d}t$ from $t = 0$ until $t = T$, where again $\mathrm{d}t$, T and the initial length distribution are simulation parameters. The theoretical predictions describe systems with a maximum length significantly larger than the mean length distribution and we can additionally ensure that any differences between the full and truncated systems are small by ensuring that $\alpha^N \ll 1$. With the values shown in Figure 4.3 and for $m_0 = 1 \times 10^{-6}$M we find that $\alpha^N = 8.7 \times 10^{-19}$ and so we expect the truncated system to give good agreement with the theoretical full infinite system.

To help visualise the evolution of the system, we plot the flow of the first two moments of the length distribution and these are shown on the top row of Figure 4.3. When the system has proportional clearance, the fixed point is attracting for all values of the first two moments. We can also plot the aggregate mass concentration at $t = T$ to numerically approximate the steady state aggregate mass. Figure 4.3 shows exceptional agreement between the steady state predicted by the

theory, when $\bar{l}$ is given by (4.16), and the steady state value after numerically solving the system for a long time.

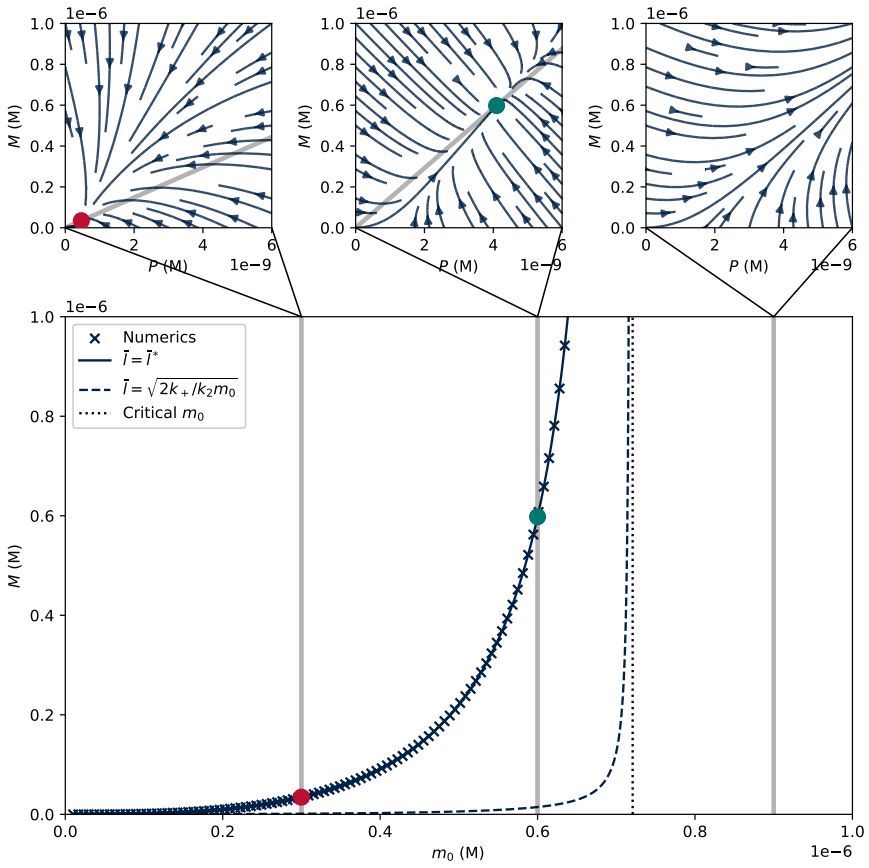

Figure 4.3: Summary of three variable description for the proportional clearance model. The top row shows the flow of M and P, given by (4.11), with $m_0 = 3 \times 10^{-7}$M, 6×10^{-7}M and 9×10^{-7}M. The main panel shows the steady state aggregate mass for varying monomer concentration, comparing the value from numerics with the two reduced models. The critical monomer concentration is $m_0 \approx 7.21 \times 10^{-7}$M. System parameters: $k_n = 4800.0\text{M}^{-1}\text{hr}^{-1}$, $k_{\text{on}} = 1.2 \times 10^8\text{M}^{-1}\text{hr}^{-1}$, $n_2 = 2$, $n_c = 2$, $\lambda = 1.0\text{hr}^{-1}$, $k_2 = 1.1 \times 10^{10}\text{M}^{-2}\text{hr}^{-1}$. Simulation parameters: $\text{d}t = 0.001\text{hr}$, $T = 1500.0\text{hr}$, $N = 10000$.

4.4.2 Bounded Clearance

The proportional clearance described above permits an analytically solvable model that gives insight into the role of clearance in neurodegenerative diseases. However the proportional clearance is an unphysical description for the removal of aggregates in all scenarios. Breaking down aggregates into the clearance products will require energy to break the bonds along the fibre that hold the monomers together, typically

hydrogen bonds and hydrophobic interactions [16]. The energy consumption will increase linearly with the number of these bonds being overcome and thus the rate of energy consumption increases with rate of aggregate mass clearance. There will be some maximum energy consumption rate for the cell and this will therefore translate to a maximum clearance rate of aggregates. In this section we explore the fundamentally different phenomena that arise from this bounded clearance.

The exact functional form describing the kinetics of aggregate clearance will determine how the clearance rate approaches this upper bound. For example, there could be a finite fuel component such as ATP that is depleted as aggregates are cleared and limits the clearance rate, the aggregates may cause toxic damage to the cell and affect the efficiency of clearance processes or, as we will assume, the clearance mechanism may have enzyme-like rate kinetics. Consider the ubiquitin (Ub)-proteasome system that tags aggregates with Ub before the aggregates are unfolded and cleaved in the proteasome, or chaperone mediated autophagy where chaperones deliver cargoes to lysosomes to be degraded [142], [143]. Both of these clearance processes can be modelled as the binding of an essential clearance component (E), either Ub or the chaperone, before the bound complex is then removed from the system and the intermediary clearance component is released. For an aggregate A_i, with concentration p_i and an clearance component E with concentration p_e, the clearance reaction can be modelled as

$$\mathrm{A}_i + \mathrm{E} \underset{k_i^d}{\overset{k_i^b}{\rightleftharpoons}} \mathrm{C}_i \xrightarrow{k_i^c} \mathrm{E} + \mathrm{Clearance\,Products} \tag{4.23}$$

where k_i^b and k_i^d are the binding and dissociation rates of the aggregate and intermediary component and k_i^c is the rate constant describing the removal of the aggregate. The intermediate clearance component binds to an aggregate of size A_i to form a complex C_i, with concentration c_i, which can either dissociate or be broken down and cleared.

This setup is similar to the Michaelis–Menten (MM) description for reactions kinetics where the E component is the enzyme. However here we have a series of different sized aggregates that all compete for the same component. We can

calculate the expected rates in the system in the same way as the single substrate analysis: assume that the total E component in the system is constant, $p_e^T = p_e + \sum_i c_i$, and that the aggregate binding is at equilibrium for all lengths, $k_i^b p_e p_i = k_i^d c_i$. These expressions give

$$c_i = p_e^T \frac{k_i^b}{k_i^d} \left(\frac{p_i}{1 + \sum_j p_j \frac{k_j^b}{k_j^d}} \right). \tag{4.24}$$

The clearance of aggregates of size i in the system is $\lambda_i = k_i^c c_i$. In general this will not reduce to a closed form pair of moment equations, however if we assume that the rates are independent of aggregate size, $k_i^c = k^c$, $k_i^b = k^b$ and $k_i^d = k^d$, then this reduces to the typical MM kinetics, as all aggregates act effectively as the same single substrate species. This now gives the moment equations with modified clearance as

$$\frac{\mathrm{d}M}{\mathrm{d}t} = n_\mathrm{c} k_n m_0^{n_\mathrm{c}} + n_2 k_2 m_0^{n_2} M + 2k_\mathrm{on} m_0 P - \frac{\lambda_M M}{K_M + P} \tag{4.25}$$

$$\frac{\mathrm{d}P}{\mathrm{d}t} = k_n m_0^{n_\mathrm{c}} + k_2 m_0^{n_2} M - \frac{\lambda_M P}{K_M + P}. \tag{4.26}$$

where we have defined $\lambda_M = k^c p_e^T$ and $K_M = k^d/k^b$. When $P \ll K_M$, the clearance is proportional to the concentration as before, with an equivalent clearance rate of $\lambda = \lambda_M / K_M$. However for $P \gg K_M$, the clearance saturates with a maximum number clearance rate λ_M and a maximum mass clearance rate mass clearance rate $\lambda_M \bar{l}$.

Solving for the steady state of the system, $\mathrm{d}M/\mathrm{d}t = \mathrm{d}P/\mathrm{d}t = 0$, gives three pairs of solutions for M^* and P^*. For typical system parameters, two pairs of the steady states have real positive solutions for both M^* and P^*. At a critical monomer concentration these two solutions undergo a sub-critical saddle bifurcation and merge, such that for monomer concentrations above this critical value there no longer exists a positive steady state, as can be seen in Figure 4.4. Similarly to the case for proportional clearance, when the monomer concentration is large we expect the mass of aggregates in a system to exhibit unbound growth. When the monomer concentration is less than this critical value, there exists a steady state, however unlike when the clearance is proportional, the system will not necessarily converge

to this equilibrium. Whether the steady state is reached depends on the initial mass and number concentrations, M and P (top row of Figure 4.4). In particular even for low monomer concentrations, if the initial mass of aggregates is very large then the aggregate self-replication will occur at a faster rate than the aggregate clearance, as the clearance rate will plateau. Therefore even for a low monomer concentration a large aggregate mass can result in an exponentially aggregating system.

Again, we can solve for the steady state length distribution when this exists. For the specific case where $n_c = n_2$ we have

$$k_n m_0^{n_c} + k_2 m_0^{n_c} M - 2k_{on} m_0 p_{n_c} - \frac{\lambda_P p_{n_c}}{K_M + P} = 0 \tag{4.27}$$

and detailed balance for all aggregates of other lengths gives the same geometric decay, but with a different decay rate, α,

$$p_i = \alpha^{n_c - i} p_{n_c} \quad \text{with} \quad \alpha = \frac{2k_{on} m_0 (K_M + P)}{2k_{on} m_0 (K_M + P) + \lambda_P}. \tag{4.28}$$

Evaluating the sums to determine M, P and p_{n_c}, gives the same pair of positive real solutions, as expected.

4.4.3 Reduced Models of in vivo Aggregation

When the aggregate clearance and other rates are prescribed, the system and its dynamics are determined by three variables, M, P and m_0, where m_0 is unaffected by the aggregation kinetics. However we keep the monomer concentration as a system variable to explore the role of monomer reducing therapies. The fate of a system determines whether a cell is *healthy* or *diseased* with unbound growth describing the diseased state and a finite steady state for healthy cells. Thus understanding whether specific parameter values lead to unbound or bound aggregation will aid disease understanding and in particular the onset and incidence of the disease.

Constant Clearance

When the clearance is proportional to the aggregate concentration the fate of the system will be entirely determined by the monomer concentration. We can reduce the three variable description (M, P and m_0) to a two parameter description by

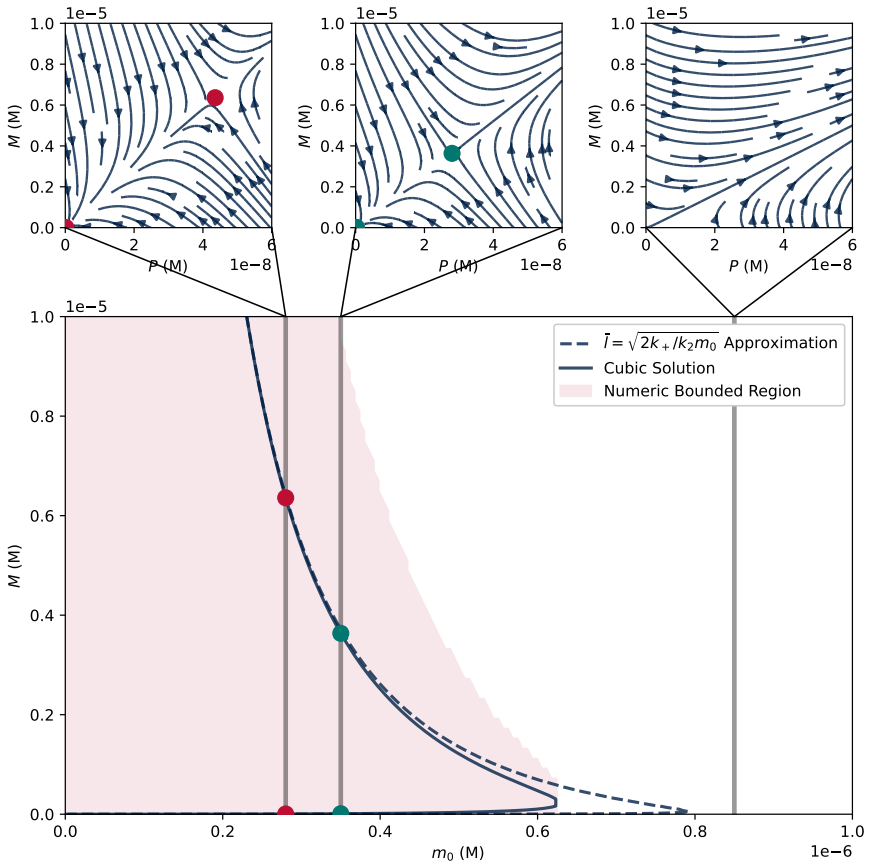

Figure 4.4: Summary of three variable description for the enzyme-like clearance model. The top row shows the flow of M and P, given by (4.25) and (4.26), with $m_0 = 2.8\times10^{-7}$M, 3.5×10^{-7}M and 8.5×10^{-7}M. The main panel shows the steady state aggregate mass for varying monomer concentration, showing the exact (cubic) solution as well as the reduced model. The shaded region corresponds to the phase space of initial conditions that results in a finite aggregate mass after numerically evolving the full master equation for a time T. System parameters: $k_n = 5000.0\text{M}^{-1}\text{hr}^{-1}$, $k_{\text{on}} = 1.2 \times 10^8\text{M}^{-1}\text{hr}^{-1}$, $n_2 = 2$, $n_c = 2$, $\lambda_M = 2.5 \times 10^{-8}\text{Mhr}^{-1}$, $K_M = 1.0 \times 10^{-8}$M, $k_2 = 4.0 \times 10^{10}\text{M}^{-2}\text{hr}^{-1}$. Simulation parameters: $dt = 0.001$hr, $T = 100.0$hr $N = 10000$ and the initial length distribution proportional to a Gaussian with mean of 1000 and standard deviation of 200.

prescribing the average length of the aggregates, $\bar{l}$. In the case of unbounded proportional clearance, the steady state is given by $\mathbf{q} = \mathbf{A}^{-1}\mathbf{b}$ and so an obvious choice for $\bar{l}$ is to choose the steady state value, $\bar{l}^* = M^*/P^*$, given by (4.16), which exactly recovers the same steady state mass (M^*) as the full model. With this assumption, the evolution equation for M becomes

$$\frac{\mathrm{d}M}{\mathrm{d}t} = n_c k_n m_0^{n_c} + n_2 k_2 m_0^{n_2} M + 2k_{\text{on}} m_0 M/\bar{l}^* - \lambda M. \tag{4.29}$$

Along with $\mathrm{d}m_0/\mathrm{d}t = 0$ this defines a reduced model that captures the key features of the aggregation kinetics: the approach to the steady state for $m_0 < m_0^{(\mathrm{crit})}$ and unbounded growth for $m_0 > m_0^{(\mathrm{crit})}$. A phase plane of this model clearly shows the dynamics and the emergence of the stability and this can be seen in Figure 4.5. When the aggregate mass is very low, the mass increases (flows upwards on the plot) until it approaches the steady state line and is balanced by clearance. When the monomer concentration is high ($m_0 > m_0^{(\mathrm{crit})}$) there is no steady state distribution and so the aggregate mass will continue to increase. When the monomer concentration is low ($m_0 < m_0^{(\mathrm{crit})}$) and the mass of aggregates is high, aggregates will be cleared from the system (move down on the phase plane) until the system reaches the steady state mass concentration.

The average length assumption projects the two dimensional $M - P$ plane flows onto a line in $M - P$ space. The top row of Figure 4.3 shows this line and the key features of the dynamics are well captured by the projection onto the line. We assumed a linear relationship between M and P, however a more complex functional relationship may capture the dynamics more accurately as there appears to be an obvious slow manifold in the $M - P$ space, however the linear relationship captures the key features and makes it easy to interpret fixed points and their stability.

When the monomer concentration is high and the linear system grows without bound, the long time behaviour of $\mathbf{q}$ is determined by the eigenvector of $\mathbf{A}$ corresponding to the positive eigenvalue ν_+. The ratio of the components of this eigenvector gives the average length for high aggregate mass, which is

$$\bar{l} = \frac{m_0^{-\frac{n_2}{2}}\sqrt{k_2 n_2^2 m_0^{n_2} + 8k_{\mathrm{on}}m_0} + \sqrt{k_2}n_2}{2\sqrt{k_2}}. \tag{4.30}$$

Typically, we expect $k_2 m_0^{n_2} \ll k_{\mathrm{on}} m_0$ and thus $\bar{l} = m_0^{\frac{1-n_2}{2}}\sqrt{2k_{\mathrm{on}}/k_2}$. In fact, this limit has been used as the as the average aggregate length [144] however it is only a good description for large aggregate masses and specific system parameters. Using this $\bar{l}$ in the reduced dynamics (4.29), does not accurately describe the steady state aggregate distribution and in fact predicts a much lower steady state mass (shown

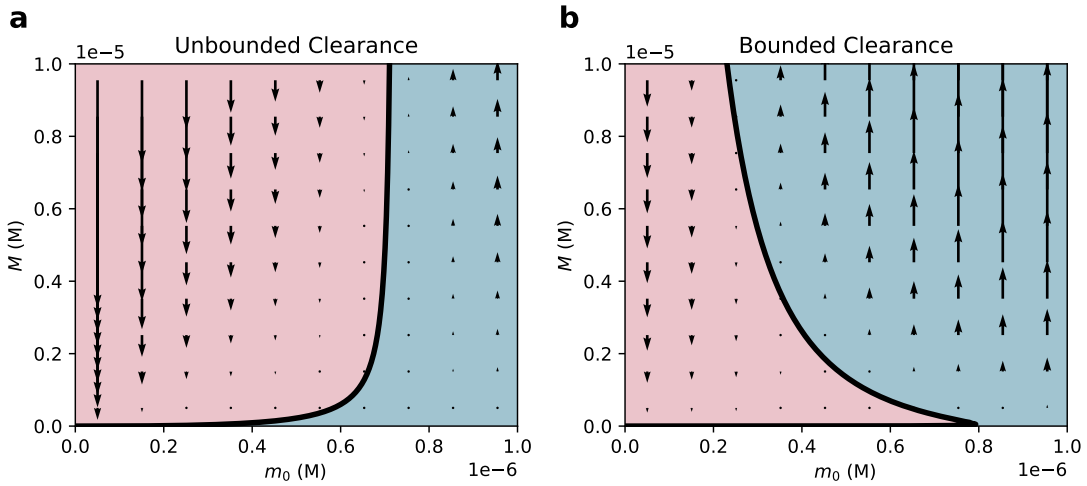

Figure 4.5: Flow in the $M - m_0$ plane from the reduced models for constant and enzyme-like clearance kinetics. The background colour shows the direction of the flow. (a) Reduced model from (4.29) with $k_n = 4800.0\text{M}^{-1}\text{hr}^{-1}$, $\lambda = 1.0\text{hr}^{-1}$, $k_2 = 1.1 \times 10^{10}\text{M}^{-2}\text{hr}^{-1}$ and $\bar{l} = (2k_{\text{on}}m_0 + n_{\text{c}}\lambda)/\lambda$. (b) Reduced model from (4.31) with $k_n = 5000.0\text{M}^{-1}\text{hr}^{-1}$, $\lambda_M = 2.5\times10^{-8}\text{M}$, $K_M = 1.0\times10^{-8}\text{Mhr}^{-1}$, $k_2 = 4.0\times10^{10}\text{M}^{-2}\text{hr}^{-1}$ and $\bar{l} = \sqrt{2k_{\text{on}}/k_2m_0}$. Additional system parameters in (a) and (b) are $n_2 = 2$, $n_{\text{c}} = 2$, $k_{\text{on}} = 1.2 \times 10^{8}\text{M}^{-1}\text{hr}^{-1}$.

in Figure 4.3). However, both length distributions exactly capture the transition from the bounded to unbounded dynamics.

Bounded Clearance

We can similarly reduce the system to a two parameter description when the clearance is bounded to give

$$\frac{\text{d}M}{\text{d}t} = n_{\text{c}}k_n m_0^{n_{\text{c}}} + n_2 k_2 m_0^{n_2} M + 2k_{\text{on}}m_0 M/\bar{l}^* - \frac{\lambda_M M}{K_M + M/\bar{l}^*}. \tag{4.31}$$

However, the effects of the bounded clearance occur at high aggregate mass and so we use the average length for large aggregate mass given by (4.30). For the parameters explored here, this becomes $\bar{l} = \sqrt{2k_{\text{on}}/k_2m_0}$. The fixed points of this reduced system are now quadratic in M and this gives two steady states when m_0 is low and no steady states when m_0 is high. This reduced model captures the key features of the full model, with the existence of a stable and unstable fixed point and a critical monomer concentration. However, the exact value at which this bifurcation occurs is different in the full and reduced models. This is due to

the approximation for $\bar{l}$ being accurate when the aggregate steady state mass is large, which is the upper branch of the stability line at low monomer concentration. Figure 4.4 shows that the two models agree in this region.

The fate of the system now depends on both the monomer concentration and the aggregate mass. The system is only stable, and therefore healthy, if both the monomer concentration and aggregate mass are low. Intuitively this dependence on the aggregate mass makes sense. If there are more aggregates (number and mass) in the system, then the rates of secondary nucleation and elongation will increase. When the aggregate clearance rate is high enough to out compete these effects then the aggregate mass/number is reduced and approaches a steady state value where the production of aggregates and clearance rates are balanced. For very large aggregate mass/number, the production rates of aggregates continue to increase with increasing aggregate mass/number, however for physically realistic models of clearance mechanisms the removal rate of aggregates will begin to saturate and at some point will no longer be able to balance the aggregate production/elongation rates, leading to runaway aggregation.

4.5 Generalising the Dynamics

4.5.1 Generalised Models of Clearance

When developing the model of bounded clearance in Section 4.4.2 we focused on the kinetics of an enzyme-like mediated clearance mechanism with binding rates independent of aggregate size. Crucially, this model predicts an upper unstable branch in the phase plane of the $M - m_0$ dynamics. However, this phenomenon is general to any clearance that increases sub linearly with increasing aggregates. Since the aggregate production rate from secondary nucleation is proportional to the mass of aggregates, any sub linear clearance will not be able to compete at large aggregate mass concentrations. We consider alternative clearance processes and the subsequent kinetics below.

Enzyme-like Kinetics in Aggregate Mass

If the intermediary clearance component (E) can attach to aggregates at any position, then we would expect this binding rate to be proportional to the aggregate length and the dissociation rate to be constant, so that $k_i^b/k_i^d \propto i$. As in (4.23) we keep the assumption that only one intermediary clearance component can bind to an aggregate. It also makes sense that the clearance processes, such as those from the proteasome system, will breakdown aggregates at a rate inversely proportional to the number of monomer-monomer bonds that have have to be broken, $(i-1)$, and so we can approximate $k_i^c \propto i^{-1}$. With these modifications, the clearance rate now saturates in M, rather than P giving clearance for the number and mass concentrations as $\tilde{\lambda}P/(\tilde{K}+M)$ and $\tilde{\lambda}M/(\tilde{K}+M)$ respectively. When the rate constants $\tilde{\lambda}$ and $\tilde{K}$ are scaled by a constant on the order of the average length, the system has identical behaviour to the number saturating clearance, although the exact fixed points are slightly perturbed. The reduced dynamics for this model is shown in the top-left panel of Figure 4.6. The reduced model for the system is

$$\frac{\mathrm{d}M}{\mathrm{d}t} = n_\mathrm{c} k_n m_0^{n_\mathrm{c}} + n_2 k_2 m_0^{n_2} M + 2k_\mathrm{on} m_0 M/\bar{l} - \frac{\tilde{\lambda} M}{\tilde{K}+M}. \tag{4.32}$$

Multiple Clearance Mechanisms

We expect that the complex regulation of living systems will result in multiple mechanism to remove aggregates, with different kinetics and saturation. Again as long as the removal mechanisms are sub-linear in aggregate mass, then the upper unstable branch mass will be unstable and the key features of the model remain. For example, combining a clearance proportional to mass and an MM-like clearance that saturates in aggregate number (the clearance mechanisms in (4.29) and (4.31)) we find that the bifurcation point moves to a higher monomer concentration, but that the bifurcation structure remains almost unchanged, as can be seen in top-right of Figure 4.6. The reduced model for this system is

$$\frac{\mathrm{d}M}{\mathrm{d}t} = n_\mathrm{c} k_n m_0^{n_\mathrm{c}} + n_2 k_2 m_0^{n_2} M + 2k_\mathrm{on} m_0 M/\bar{l} - \lambda M - \frac{\lambda_M M}{K_M + M/\bar{l}}. \tag{4.33}$$

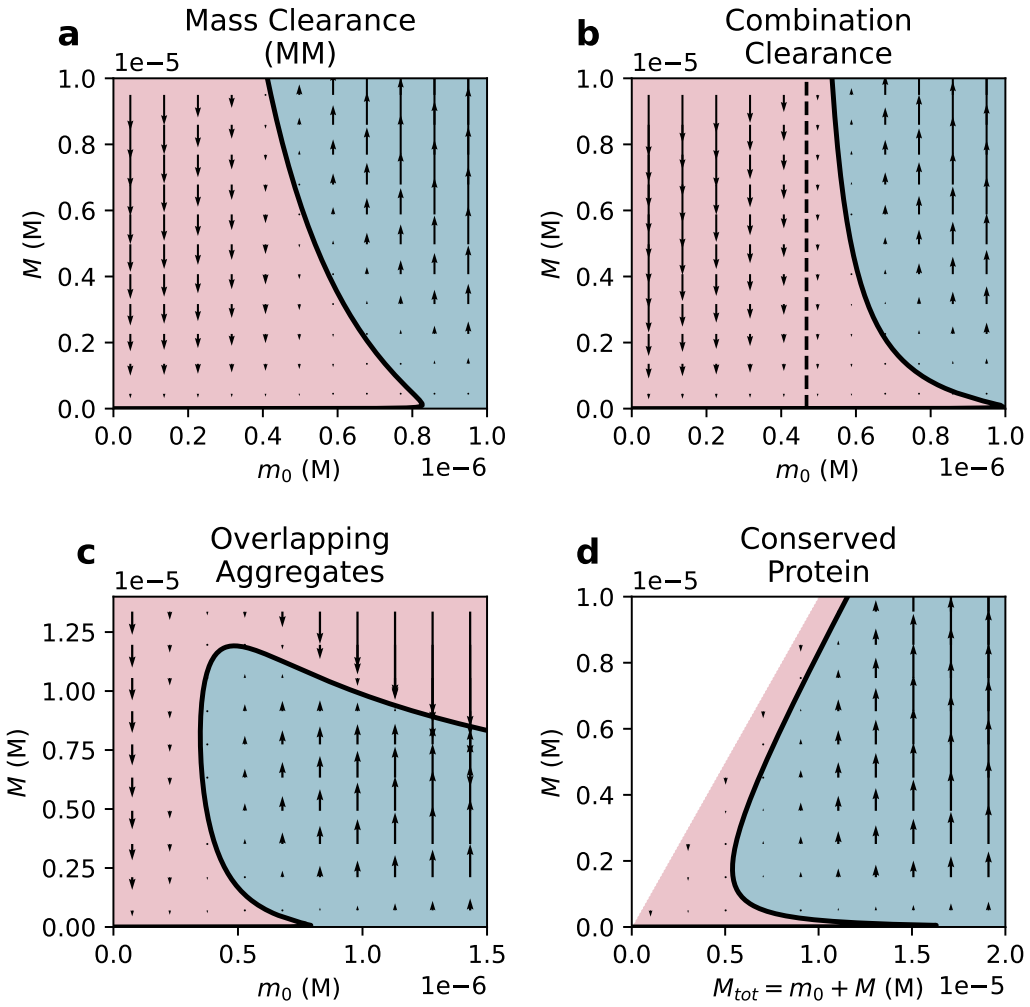

Figure 4.6: Reduced dynamics for the generalised models. The flows in the different plots are given by (a) (4.32) with $\tilde{\lambda} = 1.25 \times 10^{-5}\text{Mhr}^{-1}$, $\tilde{K} = 5.0 \times 10^{-6}\text{M}$ (b) (4.33) with $\lambda_M = 2.5 \times 10^{-8}\text{Mhr}^{-1}$, $K_M = 1.0 \times 10^{-8}\text{M}$, $\lambda = 1$ (c) (4.34) with $\lambda_M = 1.25 \times 10^{-5}\text{Mhr}^{-1}$, $\tilde{K} = 5.0 \times 10^{-6}\text{M}$, $\rho = 3.8 \times 10^{8}\text{M}^{-1}$ (d) (4.35) with $\lambda_M = 1.0 \times 10^{-6}\text{Mhr}^{-1}$, $K_M = 1.0 \times 10^{-9}\text{M}$. Additional system parameters in (a)—(d) are $k_n = 5000.0\text{M}^{-1}\text{hr}^{-1}$, $k_{\text{on}} = 1.2 \times 10^{8}\text{M}^{-1}\text{hr}^{-1}$, $n_{\text{c}} = 2$, $n_2 = 2$, $k_2 = 4.0 \times 10^{10}\text{M}^{-2}\text{hr}^{-1}$, and $\bar{l} = \sqrt{2k_{\text{on}}/k_2 m_0}$.

4.5.2 Exponential Growth is Unphysical

The exponential growth of the aggregate mass is labelled as the disease state. For a cell of finite volume and resources the exponential growth can only occur for finite time before other factors reduce the rate of growth. Autopsy data show that diseased cells are often full of aggregates (for example see coronal and sagittal planes in Iba, Guo, McBride, *et al.* [145]) so that the aggregate mass must be limited at some

stage. To describe this, we can modify the reduced model in (4.31) and introduce a correction to the secondary nucleation term. As the aggregate concentration increases, multiple aggregates may touch or overlap in space and thus prevent this overlapping region of the aggregate surface from acting as a catalyst for secondary nucleation. If we assume that each aggregate is independently distributed within the volume of the tissue/cell, then we expect the probability of two aggregates being separated by a distance less than some threshold to increase like M^2 and so the aggregation kinetics with this corrected aggregate surface becomes

$$\frac{\mathrm{d}M}{\mathrm{d}t} = n_{\mathrm{c}} k_n m_0^{n_{\mathrm{c}}} + n_2 k_2 m_0^{n_2}(M - \rho M^2) + 2k_{\mathrm{on}} m_0 M/\bar{l} - \frac{\lambda_M M}{K_M + M/\bar{l}} \tag{4.34}$$

where ρ is the overlap constant. The bottom-left panel of Figure 4.6 shows the reduced dynamics which appear similar to before, however there is now a hysteresis loop. For very low monomer concentration there is only one steady state as the clearance mechanisms grow faster than the secondary nucleation and the steady state is determined by the balance of primary nucleation and clearance. For intermediate monomer concentrations, there is a region where the secondary nucleation dominates, as before, however additionally for larger aggregate mass the crowding effects prevent further increase in aggregate mass and there is a third steady state that is stable with large aggregate mass. For even larger values of aggregate mass, the system undergoes the same bifurcation as before for low values of the aggregate mass, but this large aggregate mass steady state persists and is attracting everywhere. Phenomenologically, we interpret this exactly as before, however now the aggregate mass in the diseased state is bounded at some very high aggregate mass, which is more consistent with finite sized cells. Despite being bounded, we expect that the aggregate mass will still be significantly toxic and thus associated with the same pathology. The kinetic model in 4.34 includes the reduced aggregate surface due to overlaps, however other mechanisms may reduce the aggregation rate and similarly result in a maximum aggregate mass. As with the clearance, the exact molecular mechanisms do not affect the observed macroscopic phenomena, but might slightly alter the concentrations at which transitions between the system states occur.

4.5.3 Non-Conserved Monomer

The models of aggregation considered so far assume constant monomer concentration in the cell, motivated by cellular homeostasis regulating this concentration. When the aggregate mass is large in the system the rate of aggregation will become increasingly fast and at some point may be on the same timescales as the regulation of monomer. If this regime occurs before the maximum aggregate concentration is reached, we cannot model the monomer concentration as constant. An alternative is to assume the aggregation kinetics are much faster than the expression of the monomer and so the total protein in the system, $M_{tot} = M + m$ is constant. Assuming the MM-like clearance mechanism, the rate of change of aggregate mass is still given by (4.31) and substituting $m_0 = M_{tot} - M$, so that $\dot{M} = -\dot{m}$. This corresponds to clearance mechanisms converting the aggregated mass back into monomer to conserve total protein. The dynamics of the new reduced model can be seen in a phase plane of M and M_{tot}, this is shown in the bottom-right Figure 4.6. The equation describing the system is

$$\frac{\mathrm{d}M}{\mathrm{d}t} = n_{\mathrm{c}}k_n(M_{tot}-M)^{n_{\mathrm{c}}} + n_2k_2(M_{tot}-M)^{n_2}M + 2k_{\mathrm{on}}(M_{tot}-M)M/\bar{l} - \frac{\lambda_M M}{K_M + M/\bar{l}} \tag{4.35}$$

Since $\dot{M} = -\dot{m}$, the effects of the conserved total protein will be seen when the aggregate mass concentration is the same order of magnitude as the monomer concentration. To demonstrate this coupling, the plot shows a wide range of total aggregate mass. There is also a region of the graph that is unfeasible, corresponding to there being more aggregated protein than there is total protein, which is not possible. We therefore chose rate constants that show the effects of the bounded clearance on a similar scale to the aggregate mass. From the plot it can be seen that system dynamics for conserved total protein has similar structure to the model with modified secondary nucleation due to overlapping aggregates, except with an increasing upper branch. The upper branch for large monomer concentration has almost all protein in the aggregated state, however there still exists some monomer so that the nucleation rates balance the clearance rates.

This model and the model in (4.31) represent two distinct regimes: the aggregation kinetics are much faster than the homeostatic mechanisms or the inverse. The full system is likely to couple these timescales, and neither $\dot{m}_0$=0 nor $\dot{M}_{tot}$=0 akin to the arrows in the reduced models being tilted rather than vertical. It is harder to determine the fate of the system from the coupled dynamics, but looking at the two limiting regimes we recover the same macroscopic behaviour and features of the phase plane.

4.5.4 Length Dependent Seeding

In assuming an average aggregate length to reduce the system dynamics to the $m_0 - M$ space we ignored the dependence of the fate of the system on P. Looking at the top row of Figure 4.4, we can see that for a constant initial aggregate mass, the number of aggregates initially can actually determine whether the system evolves to an unbound aggregate mass or the low aggregate mass steady state. In fact, there exists a maximum number of aggregates for which the aggregate mass will remain bounded and if there are initially more aggregates in the system than this, then the flow of the system will result in unbounded aggregation. This result is useful to understand seeding experiments in vivo. An experimental challenge is to control the length distribution of aggregates that will be used to seed a system to investigate the in vivo dynamics. Here we see that a different length distribution, but the same aggregate mass, can in fact alter the fate of identical cells and so conclusions drawn from comparing the aggregation kinetics with uncontrolled length distributions may be misleading.

This may also have consequences in the spreading of pathology within the brain. The seeding hypothesis suggests that pathological aggregates can be transported (either actively or passively) into neighbouring brain regions, seeding these regions and causing the formation of new aggregates, such as the so called *Braak staging* in Parkinson's Disease [146]. The general connectivity between different regions of the brain has been explored as driving the spread of pathology [147], [148]. However, given the length dependent seeding suggested here, the spread of the disease would

be more accurately described with a detailed knowledge of the transport properties of these connections. For example, short aggregates might be expected to diffuse faster and thus be transported between regions more quickly. Given that a set aggregate mass has diffused to a new region, many small aggregates can trigger the transition to disease even when fewer longer aggregates cannot. This can significantly alter the rate at which the disease spreads, or exaggerate the spreading effects of certain transport mechanisms. This is a similar mode of action to dimeric enzymes that can experience enhanced reactivity by dissocaiting into monomers, diffusing at a faster rate, and dimerise again to carry out function [149].

4.5.5 Length Dependent Clearance

Another physically motivated modification to the constant clearance model is to reduce the rate of clearance for longer aggregates. We expect longer aggregates will take longer to clear from living cells and tissue as there are more bonds to break. It is useful to understand if this will reproduce the observed seeding behaviour even with an unbounded clearance; that is, whether a sudden increase in the concentration of aggregates, including longer and more persistent fibrils, would cause a transition to exponential growth. The logic of this argument is that since the longer aggregates take more time to clear, by the time they are removed from the system, the increase in secondary nucleation and subsequent elongation will have already replenished and then increased the concentration of longer aggregates, leading to positive feedback.

As we expect the clearance rate to be inversely proportional to the number of bonds, which goes like aggregate length, we assume $\lambda_i = \lambda i^{\nu} p_i$, where we choose $\nu = -1$. For the non-fragmenting, non-depolymerising ($k_{\text{off}} = 0$) system discussed here, the master equation for this model is

$$\frac{\mathrm{d}p_i}{\mathrm{d}t} = \delta_{i,n_C} k_n m^{n_C} + \delta_{i,n_2} k_2 m^{n_2} \left(\sum_{j=n_c}^{\infty} j p_j \right) + 2k_{\text{on}} m (p_{i-1} - p_i) - \lambda i^{-1} p_i. \quad (4.36)$$

Unlike the previous clearance models, summing over the aggregate population at each length introduces a dependence on the -1^{th} moment, $Q^{-1} = \sum_i i^{-1} p_i$, for the evolution of the aggregate number, P. This does not result in a closed moment

equation that can be used to determine the transition to disease. Instead, we can numerically evolve the system for different initial values of M and m_0 and observe the resulting dynamics. As described in Section 4.4.1 we simulate each aggregate population using the master equation and a fourth order Runge-Kutta method. When the final aggregate mass, M, is greater than a threshold value, we label the system as unstable, corresponding to a diseased state. Panel (a) of Figure 4.7 shows the values of initial M and m_0 that were simulated and the boundary between stable and unstable regions is drawn for different values of λ. Of note, is that this clearance mechanism does not show a seeding-like transition. The stability of a system does not depend on the initial aggregate mass concentration, but exclusively on the monomer concentration, similar to the case of a length independent constant clearance rate (Section 4.4.1).

This can be understood mathematically, since the evolution of all the p_is defines an infinite system of linear coupled equations. Since the system remains linear it only permits one steady state which describes the stationary length distribution. If this steady state is positive then it will be attractive for all positive concentrations. If it is not positive, then the aggregate mass concentration will increase without bound.

For $\nu = -1$ the moment equations are not closed, specifically because the evolution of P depends on Q^{-1}. For a sharply peaked distribution we can approximate the Q^{-1} moment by setting $Q^{-1} = P^2/M$, which would be exact if all aggregates were the same length. The moment equations then become

$$\frac{\mathrm{d}M}{\mathrm{d}t} = n_\mathrm{c} k_n m_0^{n_\mathrm{c}} + n_2 k_2 m_0^{n_2} M + 2k_\mathrm{on} m_0 P - \lambda P \tag{4.37}$$

$$\frac{\mathrm{d}P}{\mathrm{d}t} = k_n m_0^{n_\mathrm{c}} + k_2 m_0^{n_2} M - \lambda \frac{P^2}{M}. \tag{4.38}$$

These equations permit stationary states, M^* and P^*, which are positive and real when the system is stable. For the specific case of $n_\mathrm{c} = n_2 = 2$, we find that the system is only stable when $\lambda > 2k_\mathrm{on} m_0$. Panel (b) of Figure 4.7 demonstrates that this prediction of the transition value compares well to the numerics.

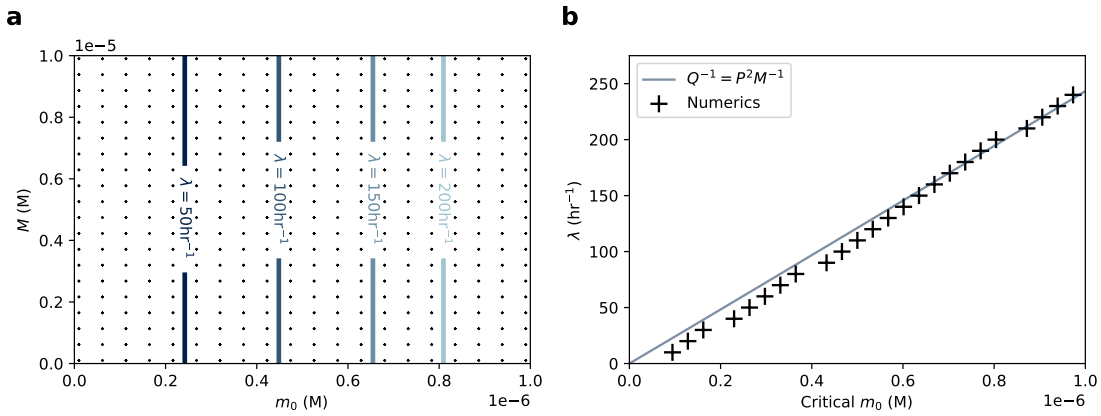

Figure 4.7: Comparison of the stability of aggregating systems with length dependent clearance, given by (4.36). In (a) the points show the values of monomer and initial aggregate mass simulated. The lines show the transition between bounded and unbounded aggregation for different λ. In (b) the monomer concentration at which the aggregation becomes unbound is shown for different λ. The initial aggregate mass simulated is $M = 5\times10^{-5}$M. The other system parameters for both (a) and (b) are $k_n = 4800\text{M}^{-1}\text{hr}^{-1}$, $k_{\text{on}} = 1.2 \times 10^8\text{M}^{-1}\text{hr}^{-1}$, $n_c = 2$, $n_2 = 2$, $k_2 = 1.1 \times 10^{10}\text{M}^{-2}\text{hr}^{-1}$, and $\nu = -1$. The threshold to determine if the aggregation was bounded is 1×10^{-3}M. The simulations used $N = 10000$, $dt = 0.001$hr, and $T = 1000$hr.

4.6 Transitions to Disease and Therapeutic Scenarios

The reduced model of the aggregation kinetics provides a powerful framework to unify experimental observations and to discuss key features of the transition to disease. In both of the reduced models and generalisations (plotted in Figures (4.5) and (4.6)) there exists a boundary in the $M - m_0$ space that separates systems that will undergo unbound aggregation and those that will have a long term finite aggregate mass. In samples from autopsies, diseased tissue contains cells that are saturated with aggregates. In our model the diseased cells correspond to unbounded aggregation and thus the onset of the disease corresponds to crossing this boundary. Each cell in a brain region will likely have different exact physical conditions that may cause slight variations between the exact reaction rates, clearance parameters and monomer concentrations. For example, spatial proximity to blood vessels or the lymphatic system might affect clearance mechanisms, the exact pressure of the internal cellular environment will affect reaction rates and cell-to-cell variability in

gene expression or cell size will cause the monomer concentrations in different cells to vary. This variability means that each cell will have a slightly different stability line in the $M - m_0$ space. If the system parameters change slightly, then some of the cells may cross the stability line and transition into the unbound aggregation state and ultimately trigger the disease.

4.6.1 Ageing reduces Clearance

A cell in the healthy state can transition to a diseased state if the rate of in vivo clearance mechanisms reduces. For example ageing, or other long term stress, might reduce the concentration of the intermediary clearance species corresponding to a reduction in the saturating clearance rate, λ_M in (4.31) [150]. This moves the critical line and in particular the value of the monomer concentration at which the bifurcation occurs, $m_0^{(\mathrm{crit})}$. A previously healthy cell with monomer concentration greater than the new critical value, $m_0 > m_0^{(\mathrm{crit})}$, will have transitioned into the disease state and will accumulate aggregates. The delay before this transition occurs depends on the value of m_0 within a cell or brain region, specifically how close that is to the initial bifurcation point, $m_0^{(\mathrm{crit})}$, as well as the rate of clearance decline.

Another compelling observation surrounds incidence of NDDs following traumatic brain injury (TBI). TBI has been shown to correlate with reduced of activity of the human glymphatic system, a fluid clearance mechanism that can support removal of toxic species in vivo [151]. Furthermore, TBI can increase the risk of developing AD [152], [153] and accelerate the onset of disease [154]. In the model developed here, this is consistent with a clearance reducing TBI event that could result in increased incidence and accelerated onset of NDDs. Understanding how these events and similar lifestyle factors could affect the onset of disease could help develop more effective treatment strategies for individuals and at the population level. For example, international rugby players' risk of developing NDDs was 2.5 times higher that the comparative population [155] and so preventative treatments could present a major opportunity in this at risk population.

4.6.2 Explaining Genetic Susceptibility

AD has a high heritability, suggesting there is a genetic component that can cause predisposition to development of the disease in a wide range of adults [156]. Genome-wide association studies correlate AD with a variety of gene sets, with the main implications being associations with amyloid/tau and microglia [157]. As discussed, changes in the quantity and quality of monomer protein expression can increase susceptibility to disease. The microglia are cells that support immune function and endocytosis with the brain, directly affecting the clearance mechanisms. These genetic studies do not provide mechanistic insight into the causes of disease, but rather suggest where to look. It is encouraging that two major features that determined the transition to disease in the model developed here, the monomer concentration and clearance mechanisms, were also identified as risk factors in human populations. Despite this currently being a very broad association, quantifying the rate parameters and the effects of mutations will hopefully make major strides towards understand and preventing the onset of the disease in humans.

AD has a reported higher prevalence in individuals with Down Syndrome (DS) [158], [159]. Although harder to diagnose due to other features of DS, upto 55% of DS adults aged 40-49 years may be clinically demented and almost all adults with DS over the age of 40 years have neuropatholigcal changes, for example amyloid plaques and neurofibrillary tangles, that would lead to a diagnosis of AD [159]. AD is more prevalent and has an earlier onset in adults with DS (for comparison see Section 4.3.1). Alongside affecting immune responses, the additional copy of chromosome 21 (which is the genetic basis of DS) increases the expression of amyloid precursor protein [158], [160]. The gene coding for amyloid precursor protein is on the long arm of chromosome 21 and so the trisomy can lead to overexpression of this gene and an increased concentration of the aggregating monomer. The mechanistic cause of this correlation has not been understood previously, and this work gives a mechanistic grounding that explains the early age of AD onset in adults with DS. The increased protein expression moves the cells and tissues closer to the critical

point in Figure 4.5. As such, a smaller reduction in the clearance rate can trigger the transition to disease, resulting in an earlier age of onset.

4.6.3 Rational Therapeutic Design

In addition to explaining the onset of disease, understanding the mechanisms governing neurodegenerative diseases is essential in the rational design of therapeutics. In the kinetic framework discussed here, an effective therapy will transition cells or tissues from the unstable to stable regions and ensure the stability of the aggregate mass in the future. In fact understanding the role of therapies is particularly pressing given recent progress in the development of new drugs to combat dementia. For the first time, a treatment for AD has been licensed for use in Great Britain[1]. The drug, called lecanemab, is a monoclonal antibody therapy that aims to support the clearance of aggregates in the brain [127] and other monoclonal antibody therapies, such as donanemab, are currently in trials with the hope of being approved for use soon [128]. However the development of these treatments is not without setbacks. Most notably, aducanumab was approved by the United States Food and Drug Administration in June 2021, however the drug showed only limited effectiveness by partially slowing the disease, and also increased the risk of cerebral microhemorrhages [129]. In January 2024, it was announced that aducanumab would be discontinued by the manufacturer[2]. It is necessary to determine how various treatments fit into the broader landscape of disease to make decisions around risk and to devise treatment strategies.

Monoclonal antibody therapies are immunotherapy treatments that focus on increasing the clearance mechanisms in the brain. This will shift the balance of aggregation and removal, moving the transition boundary and increasing the area of the stable region. However, since the system will begin proliferating aggregates as soon as it becomes unstable, then the efficacy of the response will depend on how soon any intervention is made after the system becomes unstable. At early times

[1] https://www.gov.uk/government/news/lecanemab-licensed-for-adult-patients-in-the-early-stages-of-alzheimers-disease

[2] https://www.alz.org/alzheimers-dementia/treatments/aducanumab

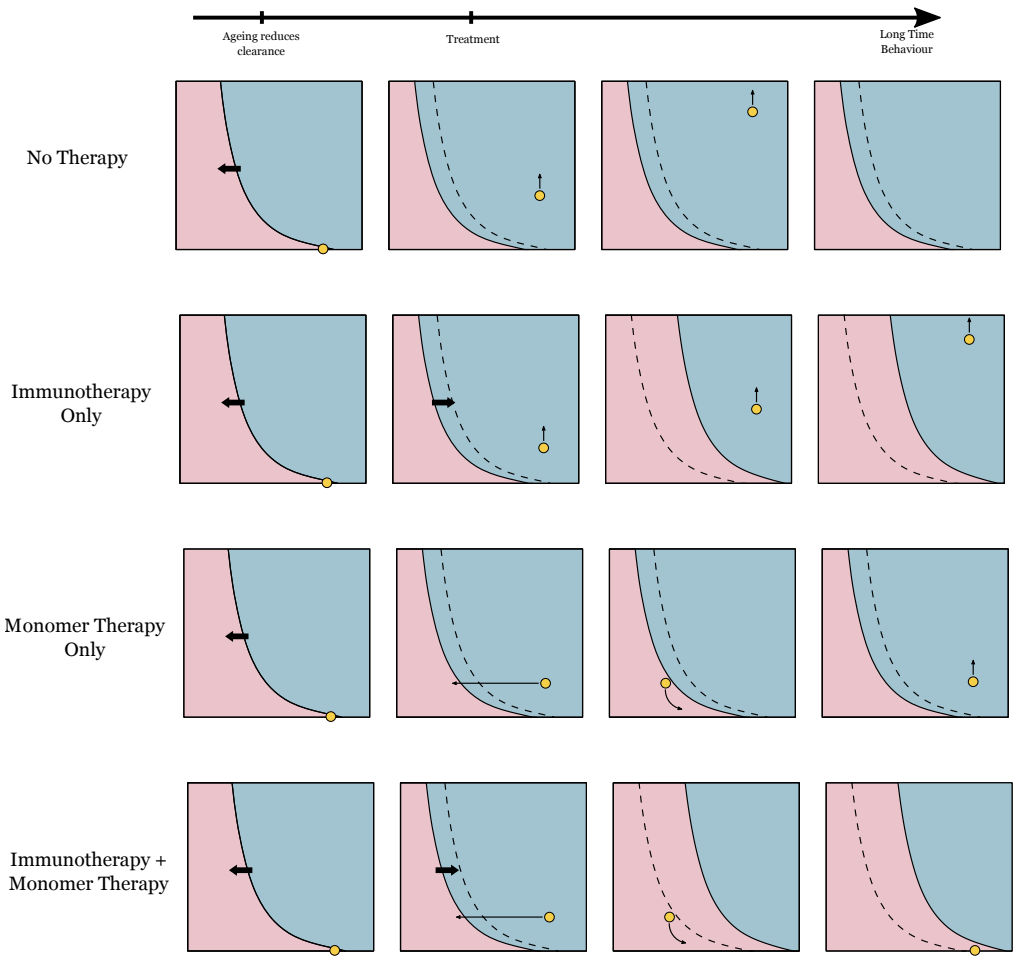

Figure 4.8: Examples showing the effects of different therapeutic schemes and combinations of therapies. The system's 'state' is given by the yellow dot that moves around the phase space.

after the transition, the system will still be close to the stable region, however at later times after more aggregation it will be further from the transition boundary so that even increasing the clearance upon drug administration may not return the system to being stable. This situation is shown in the second row of Figure 4.8. The best time to take immunotherapy treatments would be before the transition to the unstable region, however it is hard to identify exactly when individuals would become at risk and so hard to design a resource effective treatment strategy at the population level. Furthermore, increasing the population taking medication that may not be as susceptible to the onset of disease will also alter the calculation of risks associated with side effects of the treatment.

An alternative therapeutic strategy is to develop monomer-reducing therapies,

such as ASOs and epigenetic editors (see Section 4.3.1) [131], [135]. Reducing the monomer concentration can cause an unstable system to cross the transition boundary and return to being stable. The aggregate population and replication rate will therefore be lower, so that aggregates will be cleared more quickly than they are produced and the aggregate mass will return to the low stable concentration. However, after some time, the effects of the monomer therapy will wane and the monomer concentration will return to its original value, once again transitioning into the unstable region so that the aggregates proliferate. This situation is shown in the third row of Figure 4.8. Repeated monomer therapies that act to keep the monomer concentration at some reduced value could keep the system stable, however repeated exposure to ASOs can induce off target toxic effects and if the protein monomer is functional then significantly reducing its concentration over a prolonged period of time could affect the healthy function of the cell [131].

An alternative therapeutic strategy that this theory encourages could be a combination therapy of both immunotherapy and monomer reducing therapy. Reducing the monomer ensures an initial transition to the stable region and the subsequent immunotherapy ensures that the system remains in this stable region in the longer term. The final row of Figure 4.8 demonstrates how this process will lead to longer term stability and how this type of combination therapy could overcome the challenges associated with the separate treatments. However, this is still only a schematic description and quantifying the various rate parameters in the model is necessary to determine if this is a realistic disease relevant parameter regime. The values used here are based on in vitro measurements but these could be significantly affected by the different biophysical environment in vivo. Moving these theoretical results to prescribed medication would additionally require extensive clinical trials, determining exact dosages and dose frequencies as well as confirming efficacy and testing for side effects. Despite all of these limitations, the ability of this model to reproduce the currently observed phenomena of NDDs remains compelling.

4.7 Summary and Conclusions

This chapter reviewed the mathematics of the kinetics of aggregation which provide accurate descriptions of in vitro aggregation experiments. However, this theory alone cannot explain in vivo observations and the clearance mechanisms, that remove aggregates, need to be included in the models of living systems. Combining existing theories of aggregation with bounded rate clearance mechanisms gives a description of the disease with all key behaviours. These experimental observations are uniquely captured by a bounded clearance rate. Even with complex clearance kinetics (e.g. length dependent clearance) experimental observations cannot be reproduced if the clearance rate is unbounded.

This model presents a unified theory that can describe different disease phenomena with different parameter values. However, a major milestone in the continued development of this theory will be to experimentally determine the different parameter values and disease relevant regimes. I am optimistic that ongoing experimental work will soon quantify these rates. For example, the Distributed Amphifluoric Fluorescence Resonance Energy Transfer (DAmFRET) developed by the group of Dr Randal Halfman [161] can simultaneously measure relative monomer and aggregate concentration. This data would populate the $m_0 - M$ phase planes such as those drawn in Figures (4.5) and (4.6). Time course DAmFRET data will identify the stability boundary in the phase plane and can be used to determine rate parameters via fitting.

5
Concluding Remarks

Contents

5.1 The Investigated Protein Organisation 129
5.1.1 Active Phase Separation of Dense Mixtures 129
5.1.2 Membrane Mediated Elastic Interactions 130
5.1.3 Protein Aggregation in Disease 131
5.2 The Interplay of Protein Organisation 132
5.2.1 Membranes and Condensates in Aggregation 132
5.2.2 Phase-Separated Curved Domains 134
5.3 The Importance of Protein Organisation 135

5.1 The Investigated Protein Organisation

In this thesis, we have explored a variety of physical forces and processes that act to organise proteins. The spirit of these models was not to develop extremely high fidelity simulations, but to construct minimal models that can predict or explain phenomena of protein organisation. A brief summary of the distinct chapters and suggestions for future work are outlined below.

5.1.1 Active Phase Separation of Dense Mixtures

Summary

Historically, the physics of liquid-liquid phase separation is built around the equilibrium interactions between different components. However, in this chapter we showed that purely non-equilibrium chemical reactions can drive the formation of two distinct phases in a fluid mixture. We developed a thermodynamically consistent, minimal model of an active mixture comprised of an enzyme, a substrate and a product component. When the enzyme permits a driven reaction that acts to convert substrate to product it can generate a locally increased product concentration compared to regions with no enzyme. This generates a gradient in the composition of the mixture and subsequently concentration fluxes. When the enzyme responds differently to gradients in the substrate versus the product, the gradients can cause net enzyme fluxes towards regions of increased enzyme concentration and generate effective enzyme-enzyme interactions that induce phase separation. We call this mechanism *catalysis-induced phase separation*. The formation of these phases reduces the overall reaction rate due to the enzyme and so automatically provides a feedback on the reaction rate that we call *autoregulation*.

Future Work

The model developed in this chapter was deliberately minimal to explore the onset of the phase separation. Immediate next steps are therefore to generalise the model and identify the situations in which this mechanism of phase separation is relevant. For example, adding equilibrium interactions back into the model and understanding

how the non-equilibrium effects interplay with the equilibrium interactions presents interesting and biologically relevant research. Another generalisation is to consider a model with additional reaction components, building up to catalysed reaction networks. This will likely increase the complexity of the emergent phenomena and potentially give rise to new feedback mechanisms between the reactions. We argued in this chapter that catalysis-induced phase separation will be relevant for many biological systems, however, it would be exciting to prove this with experimental observations, or build a synthetic system that undergoes this instability. Since experimental systems often have more complexity than the theoretical minimal models, it will likely be useful to understand the generalisations of the effect before searching for experimental validation.

5.1.2 Membrane Mediated Elastic Interactions

Summary

The focus of this chapter was the investigation of how curvature-inducing inclusions organise, through an interaction mediated by an elastic biological membrane. We derived that for well-separated, small inclusions, the many-body interaction between multiple inclusions is the sum of the two-body potential and we derived the form of this interaction potential. This interaction fundamentally changes when the curvature-inducing inclusions are not radially symmetric by the emergence of a well defined minimum separation compared to strong repulsion at all separations. However, in addition to altering the direction of the force, the anisotropy affects the formation of aggregates of many inclusions, as the pair interaction can be frustrated by other inclusions. As such the equilibrium arrangements of groups of inclusions are polygonal lattices.

Future Work

In this chapter, we broke the symmetry in the system by including a quadrupole mode on the contact angle imposed on the edge of the inclusion. An additional symmetry breaking could be to consider the interaction of curvature inducing

inclusions on some background curved membrane, potentially caused by bilayer asymmetry or other cellular structures such as microtubules or synthetic supports. It makes sense in a system with both global membrane asymmetry and local inclusion anisotropy that the axis of maximum curvature of the inclusions would align with the maximum curvature on the membrane to minimise energy. When multiple inclusions interact the system would have to trade off the mismatch between the inclusion-inclusion alignment and the membrane-inclusion alignment. Additionally, using the interaction potential derived we could investigate the different structures formed by inclusions with different anisotropy, for example considering two distinct inclusion species.

5.1.3 Protein Aggregation in Disease

Summary

Understanding the onset and development of neurodegenerative diseases is necessary to design rational therapeutics and treatment plans. In this chapter, we developed a kinetic model of the aggregation process that unifies different diseases of aggregating proteins and can explain and predict all existing experimental observations (seeding, recovery and incidence). My innovation was to introduce a bounding effect on the clearance of aggregates from a system, which is a physically realistic constraint. The model predicts that the relevant factors describing the disease are the protein monomer concentration, the aggregate mass concentration and the clearance rate. Current therapies work by increasing the clearance rate, but in fact combination therapies that include a transient reduction in the monomer concentration may be significantly more effective in returning the system to a steady state. We comprehensively explored different molecular mechanisms that could result in a bound clearance and crucially the key features of this model are robust even when the exact functional form of the clearance or aggregation kinetics are varied.

Future Work

The major focus on future work in this area should be to experimentally determine rates of the different aggregation processes. The desired rates are in vivo rates which are harder to probe experimentally compared to test tube reactions, as so there are additional constraints to keep cells and tissues alive, or connected to other organs. However, these rates can be constrained by indirect observations, such as studying the length distributions of the aggregates in cell lysate. As clinical trials continue to progress, more data regarding the onset of disease and the effect of interventions will become available which again can help to provide bounds on the different rate parameters in vivo. From a theoretical perspective, this model should be connected to multi-scale models of aggregation processes across different cells, such as models describing the spread of aggregates in tissues and ultimately to include this model in larger network models that describe the spread of the disease through different regions of the brain.

5.2 The Interplay of Protein Organisation

Proteins interact in a myriad of different ways and during my thesis research I have studied some specific examples of protein organisation. Of course there are other ways that proteins can interact, leading to function, for example, hydrodynamic coupling between enzymes can cause enhanced activity [162], [163] or the binding between discorded proteins can be modulated by depletion effects [164], [165]. In addition to these distinct different mechanisms of protein organisation, the different modes of organisation can also interplay. Even within the subset of systems studied in this thesis, there is emerging work looking at the intersection and overlap of these modes of organisation. Examples of these are listed below.

5.2.1 Membranes and Condensates in Aggregation

In Chapter 4, we outlined the basic processes of protein aggregation relevant to the onset and development of neurodegenerative diseases. However, the rates and

functional form of these mechanisms are affected by the cellular environments. One particular example is the interplay between lipid membranes and aggregation. Lipid vesicles were reported to enhance primary nucleation by three orders of magnitude [166], however, recent work that explored the molecular mechanisms describing this enhancement found that lipids were increasing the elongation rates of aggregates [167]. Additionally, this work identifies that air-water or plate-water interfaces, interfaces that are common in all in vitro experiments, can alter the kinetics of aggregation and, thus, care should be taken in drawing conclusions from these assays. Beyond simply affecting aggregation rates, tau aggregates have also been observed tethered to membranes in vesicles [168]. This could be linked to the formation of the aggregates, but could also be connected to how they are localised to extracellular vesicles. Extracellular vesicles are believed to be involved with aggregate clearance, or transmission to other neurons. Understanding this aggregate-membrane tethering interaction could provide more insight on these process.

Droplets, formed by liquid-liquid phase separation, have been implicated in the formation of pathological aggregates. The formation of aggregates is enhanced in protein-rich droplets [169]. Tau proteins (a candidate monomer protein in Alzheimer's Disease) can form small condensates via liquid-liquid phase separation that subsequently mature into pathological aggregates that can act as seeds and further proliferate disease [170]. The pathway to the formation of aggregates in disease-relevant proteins demonstrates the importance of understanding how the liquid condensates can affect the kinetics of aggregation and theoretical studies have started to explore this phenomena. Liquid droplets that sequester aggregates can affect aggregation processes in broadly two ways. Firstly, the different environment and rheology of droplets can affect the rate constants of aggregation [171] and secondly, partitioning the aggregates/monomers to have an enhanced concentration inside/outside the droplet can alter the net aggregate growth rate [172]. Furthermore, interactions between other aggregates of different lengths could themselves support the formation of liquid droplets [173]. In addition to affecting the aggregation, droplets could also affect the efficacy of therapeutics which would also be affected

by the different droplet environment and by partitioning. These mechanisms will all affect the kinetics of aggregation, however, it will be useful to understand if this will simply alter the rates in existing models of aggregation or if this interplay could lead to fundamentally different phenomena.

5.2.2 Phase-Separated Curved Domains

The role of membranes and their interplay with phase-separated droplets has also been an exciting area of research, for example wetting and remodelling of vesicle membranes by liquid droplets [174]. Furthermore, phase separation in biological membranes has been observed, even in membrane models with as little as two phospholipids and a cholesterol component [175]. Lipid-lipid and lipid-cholesterol interactions can drive the well-mixed system to form these separate domains [104] and models of phase separating systems can predict the phase behaviour [44]. However, in these model systems the amount of lipid is conserved and, in vivo, local lipid composition actually changes due to membrane recycling and as a result of the activity of enzymes which catalyse lipid synthesis and breakdown [104]. The catalysis-induced phase separation in Chapter 2 may also be relevant in the plane of membranes.

Exploring the phase behaviour of elastic membranes also provides an exciting system that couples curvature and phase. Large scale deformations in elastic membranes can be mechanically induced by varying the tension or internal pressure of a membrane, giving rise to ballooning, bulging, and necking [176]. Patterns can also occur on smaller length scales giving rise to stripes or spots when the curvature of different components and the interactions between these components are considered [177]. However, local energy consumption within a membrane might also lead to tunable shape change. Flipases and flopases are enzymes that move lipids across the bilayer [2] and driving their action with a fuel could generate gradients in curvature in the membrane, akin to the concentration gradients in Chapter 2. I predict that this could generate an instability similar to catalysis-induced phase separation that also alters the membrane shape. An alternative idea could be

Figure 5.1: DALL-E interpretation of *A realistic and photorealistic panoramic view of a futuristic world where protein organization has been harnessed to develop effective medicines and innovative synthetic biology.*

to harness embedded components in the membrane that can undergo significant conformational changes, such as switchable lipids [178]. An enzyme that changes the conformation of these components could then generate effective interactions between the conformations via the curvature mismatch and elastic effects. Again this could present a new avenue to pursue functional pattern formation on membranes.

5.3 The Importance of Protein Organisation

It is essential to understand protein organisation to design medicines for diseases caused by pathological protein organisation, and these therapies can take advantage of the relationship between emergent protein structures and the broader in vivo environment. The different ways in which these processes interplay do not only have medicinal potential, but also potential in engineering smart synthetic biological systems (perhaps moving us closer to the imagined utopia in Figure 5.1. Proteins can react and interact to carry out basic computation, or to regulate expressions of other proteins. However, the majority of work to date is limited to assuming well-mixed systems, or if there is patterning and spatial heterogeneity it is at

the level of membrane bound droplets [179]. Spatial organisation at the level of proteins presents a design space that can couple structure and function much more directly and develop tight feedback and control. The autoregulation presented in Chapter 2 is a good example of this automatic control. Active droplets have also been predicted to buffer noise in fluctuating concentrations [180], generate oscillatory metabolic cycles [181], or even act as a reaction crucible to speed up reactions [182]. These phenomena are already quite diverse, even for just this one mechanism of protein organisation where the different functional effects depend on the biophysical regime. Unifying these different interactions into a framework, such as the language of control, might help to support more system level design and ultimately the manufacture of controllable protein systems.

References

[1] R. A. L. Jones, *Soft condensed matter*. Oxford University Press, 2002. DOI: 10.1093/oso/9780198505907.001.0001.

[2] B. Alberts, A. Johnson, J. Lewis, M. Raff, K. Roberts, and P. Walter, *Molecular biology of the cell*, 5th ed. Garland Science, 2008. DOI: 10.1201/9780203833445.

[3] J. M. Berg, J. L. Tymoczko, and L. Stryer, *Biochemistry*, 5th ed. W.H. Freeman, 2002.

[4] A. M. Turing, "The chemical basis of morphogenesis", *Philosophical Transactions of the Royal Society of London. Series B, Biological Sciences*, 1952. DOI: 10.1098/rstb.1952.0012.

[5] A. Wegner and J. Engel, "Kinetics of the cooperative association of actin to actin filament", *Biophysical Chemistry*, 1975. DOI: 10.1016/0301-4622(75)80013-5.

[6] J. Agudo-Canalejo and R. Golestanian, "Pattern formation by curvature-inducing proteins on spherical membranes", *New Journal of Physics*, 2017. DOI: 10.1088/1367-2630/aa983c.

[7] D. S. Garrett, Y.-J. Seok, D.-I. Liao, A. Peterkofsky, A. M. Gronenborn, and G. M. Clore, "Solution structure of the 30 kDa n-terminal domain of enzyme i of the escherichia coli phosphoenolpyruvate:sugar phosphotransferase system by multidimensional NMR", *Biochemistry*, 1997. DOI: 10.1021/bi962924y.

[8] J. Jumper, R. Evans, A. Pritzel, *et al.*, "Highly accurate protein structure prediction with AlphaFold", *Nature*, 2021. DOI: 10.1038/s41586-021-03819-2.

[9] N. Hirokawa, S. Niwa, and Y. Tanaka, "Molecular motors in neurons: Transport mechanisms and roles in brain function, development, and disease", *Neuron*, 2010. DOI: 10.1016/j.neuron.2010.09.039.

[10] O. Keskin, A. Gursoy, B. Ma, and R. Nussinov, "Principles of proteinprotein interactions: What are the preferred ways for proteins to interact?", *Chemical Reviews*, 2008. DOI: 10.1021/cr040409x.

[11] Y. Shin and C. P. Brangwynne, "Liquid phase condensation in cell physiology and disease", *Science*, 2017. DOI: 10.1126/science.aaf4382.

[12] S. F. Banani, H. O. Lee, A. A. Hyman, and M. K. Rosen, "Biomolecular condensates: Organizers of cellular biochemistry", *Nature Reviews Molecular Cell Biology*, 2017. DOI: 10.1038/nrm.2017.7.

[13] L. M. Luheshi, D. C. Crowther, and C. M. Dobson, "Protein misfolding and disease: From the test tube to the organism", *Current Opinion in Chemical Biology*, 2008. DOI: 10.1016/j.cbpa.2008.02.011.

[14] C. M. Dobson, "Protein folding and misfolding", *Nature*, 2003. DOI: 10.1038/nature02261.

[15] F. Chiti and C. M. Dobson, "Protein misfolding, functional amyloid, and human disease", *Annual Review of Biochemistry*, 2006. DOI: 10.1146/annurev.biochem.75.101304.123901.

[16] F. Chiti and C. M. Dobson, "Protein misfolding, amyloid formation, and human disease: A summary of progress over the last decade", *Annual Review of Biochemistry*, 2017. DOI: 10.1146/annurev-biochem-061516-045115.

[17] S. Sharma, A. Gupta, and A. Kumar, "Keratin: An introduction", in *Keratin as a Protein Biopolymer*, Springer International Publishing, 2019. DOI: 10.1007/978-3-030-02901-2_1.

[18] S. Feroz, N. Muhammad, J. Ratnayake, and G. Dias, "Keratin - based materials for biomedical applications", *Bioactive Materials*, 2020. DOI: 10.1016/j.bioactmat.2020.04.007.

[19] M. Garni, S. Thamboo, C.-A. Schoenenberger, and C. G. Palivan, "Biopores/membrane proteins in synthetic polymer membranes", *Biochimica et Biophysica Acta (BBA) - Biomembranes*, 2017. DOI: 10.1016/j.bbamem.2016.10.015.

[20] B. Ramm, A. Goychuk, A. Khmelinskaia, P. Blumhardt, H. Eto, K. A. Ganzinger, E. Frey, and P. Schwille, "A diffusiophoretic mechanism for ATP-driven transport without motor proteins", *Nature Physics*, 2021. DOI: 10.1038/s41567-021-01213-3.

[21] D. E. Cameron, C. J. Bashor, and J. J. Collins, "A brief history of synthetic biology", *Nature Reviews Microbiology*, 2014. DOI: 10.1038/nrmicro3239.

[22] C. P. Brangwynne, C. R. Eckmann, D. S. Courson, A. Rybarska, C. Hoege, J. Gharakhani, F. Jülicher, and A. A. Hyman, "Germline P granules are liquid droplets that localize by controlled dissolution/condensation", *Science*, 2009. DOI: 10.1126/science.1172046.

[23] C. P. Brangwynne, P. Tompa, and R. V. Pappu, "Polymer physics of intracellular phase transitions", *Nature Physics*, 2015. DOI: 10.1038/nphys3532.

[24] M. E. Cates and J. Tailleur, "Motility-induced phase separation", *Annual Review of Condensed Matter Physics*, 2015. DOI: 10.1146/annurev-conmatphys-031214-014710.

[25] J. Agudo-Canalejo and R. Golestanian, "Active phase separation in mixtures of chemically interacting particles", *Physical Review Letters*, 2019. DOI: 10.1103/PhysRevLett.123.018101.

[26] C. A. Weber and C. Zechner, "Drops in cells", *Physics Today*, 2021. DOI: 10.1063/PT.3.4771.

[27] Y. I. Li and M. E. Cates, "Non-equilibrium phase separation with reactions: A canonical model and its behaviour", *Journal of Statistical Mechanics: Theory and Experiment*, 2020. DOI: 10.1088/1742-5468/ab7e2d.

[28] B. G. O'Flynn and T. Mittag, "The role of liquid–liquid phase separation in regulating enzyme activity", *Current Opinion in Cell Biology*, 2021. DOI: 10.1016/j.ceb.2020.12.012.

[29] L. J. Sweetlove and A. R. Fernie, "The role of dynamic enzyme assemblies and substrate channelling in metabolic regulation", *Nature Communications*, 2018. DOI: 10.1038/s41467-018-04543-8.

[30] M. W. Cotton, R. Golestanian, and J. Agudo-Canalejo, "Catalysis-induced phase separation and autoregulation of enzymatic activity", *Physical Review Letters*, 2022. DOI: 10.1103/PhysRevLett.129.158101.

[31] M. Doi, *Soft matter physics*. Oxford University Press, 2013. DOI: 10.1093/acprof:oso/9780199652952.001.0001.

[32] C. A. Weber, D. Zwicker, F. Jülicher, and C. F. Lee, "Physics of active emulsions", *Reports on Progress in Physics*, 2019. DOI: 10.1088/1361-6633/ab052b.

[33] M. Kardar, *Statistical Physics of Particles*. Cambridge University Press, 2007. DOI: https://doi.org/10.1017/CBO9780511815898.

[34] S. Mao, D. Kuldinow, M. P. Haataja, and A. Košmrlj, "Phase behavior and morphology of multicomponent liquid mixtures", *Soft Matter*, 2019. DOI: 10.1039/C8SM02045K.

[35] S. R. d. Groot and P. Mazur, *Non-equilibrium thermodynamics*. North-Holland Publishing Co., 1963.

[36] P. C. Hohenberg and B. I. Halperin, "Theory of dynamic critical phenomena", *Rev. Mod. Phys.*, 1977. DOI: https://doi.org/10.1103/RevModPhys.49.435.

[37] K. W. Kehr, K. Binder, and S. M. Reulein, "Mobility, interdiffusion, and tracer diffusion in lattice-gas models of two-component alloys", *Physical Review B*, 1989. DOI: 10.1103/PhysRevB.39.4891.

[38] J. D. Murray, *Mathematical Biology*. Springer, 1993. DOI: 10.1007/978-3-662-08542-4.

[39] E. J. Kramer, P. Green, and C. J. Palmstrøm, "Interdiffusion and marker movements in concentrated polymer-polymer diffusion couples", *Polymer*, 1984. DOI: https://doi.org/10.1016/0032-3861(84)90205-2.

[40] S. Mao, M. S. Chakraverti-Wuerthwein, H. Gaudio, and A. Košmrlj, "Designing the morphology of separated phases in multicomponent liquid mixtures", *Physical Review Letters*, 2020. DOI: 10.1103/PhysRevLett.125.218003.

[41] S. Bo, L. Hubatsch, J. Bauermann, C. A. Weber, and F. Jülicher, "Stochastic dynamics of single molecules across phase boundaries", *Physical Review Research*, 2021. DOI: 10.1103/PhysRevResearch.3.043150.

[42] F. Brauns, J. Halatek, and E. Frey, "Phase-space geometry of mass-conserving reaction-diffusion dynamics", *Physical Review X*, 2020. DOI: 10.1103/PhysRevX.10.041036.

[43] F. Brauns, H. Weyer, J. Halatek, J. Yoon, and E. Frey, "Wavelength selection by interrupted coarsening in reaction-diffusion systems", *Physical Review Letters*, 2021. DOI: 10.1103/PhysRevLett.126.104101.

[44] J. Wolff, C. M. Marques, and F. Thalmann, "Thermodynamic approach to phase coexistence in ternary phospholipid-cholesterol mixtures", *Physical Review Letters*, 2011. DOI: 10.1103/PhysRevLett.106.128104.

[45] R. Wittkowski, A. Tiribocchi, J. Stenhammar, R. J. Allen, D. Marenduzzo, and M. E. Cates, "Scalar $\varphi 4$ field theory for active-particle phase separation", *Nature Communications*, 2014. DOI: 10.1038/ncomms5351.

[46] J. Agudo-Canalejo, P. Illien, and R. Golestanian, "Phoresis and enhanced diffusion compete in enzyme chemotaxis", *Nano Letters*, 2018. DOI: 10.1021/acs.nanolett.8b00717.

[47] Y. Zhang and H. Hess, "Chemically-powered swimming and diffusion in the microscopic world", *Nature Reviews Chemistry*, 2021. DOI: 10.1038/s41570-021-00281-6.

[48] V. K. Vanag and I. R. Epstein, "Cross-diffusion and pattern formation in reaction–diffusion systems", *Phys. Chem. Chem. Phys.*, 2009. DOI: 10.1039/B813825G.

[49] R. Taylor and R. Krishna, *Multicomponent Mass Transfer*. John Wiley & Sons, 1993.

[50] G. Guevara-Carrion, T. Janzen, Y. M. Muñoz-Muñoz, and J. Vrabec, "Mutual diffusion of binary liquid mixtures containing methanol, ethanol, acetone, benzene, cyclohexane, toluene, and carbon tetrachloride", *The Journal of Chemical Physics*, 2016. DOI: 10.1063/1.4943395.

[51] G. Guevara-Carrion, Y. Gaponenko, A. Mialdun, T. Janzen, V. Shevtsova, and J. Vrabec, "Interplay of structure and diffusion in ternary liquid mixtures of benzene + acetone + varying alcohols", *The Journal of Chemical Physics*, 2018. DOI: 10.1063/1.5044431.

[52] E. F. Keller and L. A. Segel, "Initiation of slime mold aggregation viewed as an instability", *Journal of Theoretical Biology*, 1970. DOI: 10.1016/0022-5193(70)90092-5.

[53] R. Golestanian, "Phoretic active matter", *arXiv:1909.03747 [cond-mat, physics:physics]*, 2019. arXiv: 1909.03747.

[54] S. Saha, R. Golestanian, and S. Ramaswamy, "Clusters, asters, and collective oscillations in chemotactic colloids", *Physical Review E*, 2014. DOI: 10.1103/PhysRevE.89.062316.

[55] D. Frenkel and A. A. Louis, "Phase separation in binary hard-core mixtures: An exact result", *Physical Review Letters*, 1992. DOI: 10.1103/PhysRevLett.68.3363.

[56] J. D. O'Connell, A. Zhao, A. D. Ellington, and E. M. Marcotte, "Dynamic reorganization of metabolic enzymes into intracellular bodies", *Annual Review of Cell and Developmental Biology*, 2012. DOI: 10.1146/annurev-cellbio-101011-155841.

[57] M. T. Alam, V. Olin-Sandoval, A. Stincone, M. A. Keller, A. Zelezniak, B. F. Luisi, and M. Ralser, "The self-inhibitory nature of metabolic networks and its alleviation through compartmentalization", *Nature Communications*, 2017. DOI: 10.1038/ncomms16018.

[58] L. Poshyvailo, E. von Lieres, and S. Kondrat, "Does metabolite channeling accelerate enzyme-catalyzed cascade reactions?", *PLOS ONE*, 2017. DOI: 10.1371/journal.pone.0172673.

[59] M. Simunovic, G. A. Voth, A. Callan-Jones, and P. Bassereau, "When physics takes over: BAR proteins and membrane curvature", *Trends in Cell Biology*, 2015. DOI: 10.1016/j.tcb.2015.09.005.

[60] J. Zimmerberg and M. M. Kozlov, "How proteins produce cellular membrane curvature", *Nature Reviews Molecular Cell Biology*, 2006. DOI: 10.1038/nrm1784.

[61] H. Watson, "Biological membranes", *Essays in Biochemistry*, 2015. DOI: 10.1042/bse0590043.

[62] D. Lasic, "Novel applications of liposomes", *Trends in Biotechnology*, 1998. DOI: 10.1016/S0167-7799(98)01220-7.

[63] P. W. K. Rothemund, "Folding DNA to create nanoscale shapes and patterns", *Nature*, 2006. DOI: 10.1038/nature04586.

[64] A. Seifert, K. Göpfrich, J. R. Burns, N. Fertig, U. F. Keyser, and S. Howorka, "Bilayer-spanning DNA nanopores with voltage-switching between open and closed state", *ACS Nano*, 2015. DOI: 10.1021/nn5039433.

[65] A. R. Studart, "Biologically inspired dynamic material systems", *Angewandte Chemie International Edition*, 2015. DOI: 10.1002/anie.201410139.

[66] A. Czogalla, H. G. Franquelim, and P. Schwille, "DNA nanostructures on membranes as tools for synthetic biology", *Biophysical Journal*, 2016. DOI: 10.1016/j.bpj.2016.03.015.

[67] A. Czogalla, D. J. Kauert, H. G. Franquelim, V. Uzunova, Y. Zhang, R. Seidel, and P. Schwille, "Amphipathic DNA origami nanoparticles to scaffold and deform lipid membrane vesicles", *Angewandte Chemie International Edition*, 2015. DOI: 10.1002/anie.201501173.

[68] E. Boucrot, A. P. A. Ferreira, L. Almeida-Souza, *et al.*, "Endophilin marks and controls a clathrin-independent endocytic pathway", *Nature*, 2015. DOI: 10.1038/nature14067.

[69] S. Ghosh, S. Gutti, and D. Chaudhuri, "Pattern formation, localized and running pulsation on active spherical membranes", *Soft Matter*, 2021. DOI: 10.1039/D1SM00937K.

[70] D. Argudo, N. P. Bethel, F. V. Marcoline, and M. Grabe, "Continuum descriptions of membranes and their interaction with proteins: Towards chemically accurate models", *Biochimica et Biophysica Acta (BBA) - Biomembranes*, 2016. DOI: 10.1016/j.bbamem.2016.02.003.

[71] B. J. Peter, H. M. Kent, I. G. Mills, Y. Vallis, P. J. G. Butler, P. R. Evans, and H. T. McMahon, "BAR domains as sensors of membrane curvature: The amphiphysin BAR structure", *Science*, 2004. DOI: 10.1126/science.1092586.

[72] W. Helfrich, "Elastic properties of lipid bilayers: Theory and possible experiments", *Zeitschrift für Naturforschung C*, 1973. DOI: 10.1515/znc-1973-11-1209.

[73] K. S. Kim, J. Neu, and G. Oster, "Curvature-mediated interactions between membrane proteins.", *Biophysical Journal*, 1998. DOI: 10.1016/S0006-3495(98)77672-6.

[74] F. L. Brown, "Elastic modeling of biomembranes and lipid bilayers", *Annual Review of Physical Chemistry*, 2008. DOI: 10.1146/annurev.physchem.59.032607.093550.

[75] C. Tozzi, N. Walani, and M. Arroyo, "Out-of-equilibrium mechanochemistry and self-organization of fluid membranes interacting with curved proteins", *New Journal of Physics*, 2019. DOI: 10.1088/1367-2630/ab3ad6.

[76] J. García-Lara, F. Weihs, X. Ma, *et al.*, "Supramolecular structure in the membrane of *Staphylococcus aureus*", *Proceedings of the National Academy of Sciences*, 2015. DOI: 10.1073/pnas.1509557112.

[77] C. Tozzi, N. Walani, A.-L. Le Roux, P. Roca-Cusachs, and M. Arroyo, "A theory of ordering of elongated and curved proteins on membranes driven by density and curvature", *Soft Matter*, 2021. DOI: 10.1039/D0SM01733G.

[78] M. Deserno, *Fluid lipid membranes – a primer*, URL: https://www.cmu.edu/biolphys/deserno/pdf/membrane_theory.pdf, notes, 2007.

[79] O.-Y. Zhong-can and W. Helfrich, "Instability and deformation of a spherical vesicle by pressure", *Physical Review Letters*, 1987. DOI: 10.1103/PhysRevLett.59.2486.

[80] J. A. Kwiecinski, A. Goriely, and S. J. Chapman, "Interactions of anisotropic inclusions on a fluid membrane", *SIAM Journal on Applied Mathematics*, 2020. DOI: 10.1137/20M1332694.

[81] S. Ramaswamy, J. Toner, and J. Prost, "Nonequilibrium fluctuations, traveling waves, and instabilities in active membranes", *Physical Review Letters*, 2000. DOI: 10.1103/PhysRevLett.84.3494.

[82] T. R. Weikl, M. M. Kozlov, and W. Helfrich, "Interaction of conical membrane inclusions: Effect of lateral tension", *Physical Review E*, 1998. DOI: 10.1103/PhysRevE.57.6988.

[83] T. Chou, K. S. Kim, and G. Oster, "Statistical thermodynamics of membrane bending-mediated protein-protein attractions.", *Biophysical Journal*, 2001. DOI: 10.1016/S0006-3495(01)76086-9.

[84] P. Galatola and J.-B. Fournier, "Many-body interactions between curvature-inducing membrane inclusions with arbitrary cross-sections", *Soft Matter*, 2023. DOI: 10.1039/D3SM00851G.

[85] J.-B. Fournier, "Membrane protein clustering from tension and multibody interactions", *Europhysics Letters*, 2024. DOI: 10.1209/0295-5075/ad4ac2.

[86] P. G. Saffman and M. Delbrück, "Brownian motion in biological membranes", *Proceedings of the National Academy of Sciences*, 1975. DOI: 10.1073/pnas.72.8.3111.

[87] E. P. Petrov and P. Schwille, "Translational diffusion in lipid membranes beyond the Saffman-Delbrück approximation", *Biophysical Journal*, 2008. DOI: 10.1529/biophysj.107.126565.

[88] P. G. Saffman, "Brownian motion in thin sheets of viscous fluid", *Journal of Fluid Mechanics*, 1976. DOI: 10.1017/S0022112076001511.

[89] E. Süli and D. F. Mayers, *An Introduction to Numerical Analysis*. Cambridge University Press, 2003. DOI: 10.1017/CBO9780511801181.

[90] M. Simunovic, A. Šarić, J. M. Henderson, K. Y. C. Lee, and G. A. Voth, "Long-range organization of membrane-curving proteins", *ACS Central Science*, 2017. DOI: 10.1021/acscentsci.7b00392.

[91] M. Simunovic, A. Srivastava, and G. A. Voth, "Linear aggregation of proteins on the membrane as a prelude to membrane remodeling", *Proceedings of the National Academy of Sciences*, 2013. DOI: 10.1073/pnas.1309819110.

[92] T. Itoh and K. Tsujita, "Exploring membrane mechanics: The role of membrane-cortex attachment in cell dynamics", *Current Opinion in Cell Biology*, 2023. DOI: 10.1016/j.ceb.2023.102173.

[93] H. Noguchi, "Membrane tubule formation by banana-shaped proteins with or without transient network structure", *Scientific Reports*, 2016. DOI: 10.1038/srep20935.

[94] H. Noguchi, "Acceleration and suppression of banana-shaped-protein-induced tubulation by addition of small membrane inclusions of isotropic spontaneous curvatures", *Soft Matter*, 2017. DOI: 10.1039/C7SM01375B.

[95] P. Dommersnes and J.-B. Fournier, "N-body study of anisotropic membrane inclusions: Membrane mediated interactions and ordered aggregation", *The European Physical Journal B*, 1999. DOI: 10.1007/s100510050968.

[96] P. G. Dommersnes and J.-B. Fournier, "The many-body problem for anisotropic membrane inclusions and the self-assembly of "saddle" defects into an "egg carton"", *Biophysical Journal*, 2002. DOI: 10.1016/S0006-3495(02)75299-5.

[97] J. C. Loudet, A. M. Alsayed, J. Zhang, and A. G. Yodh, "Capillary interactions between anisotropic colloidal particles", *Physical Review Letters*, 2005. DOI: 10.1103/PhysRevLett.94.018301.

[98] D. Ershov, J. Sprakel, J. Appel, M. A. Cohen Stuart, and J. Van Der Gucht, "Capillarity-induced ordering of spherical colloids on an interface with anisotropic curvature", *Proceedings of the National Academy of Sciences*, 2013. DOI: 10.1073/pnas.1222196110.

[99] B. Nepal, A. Sepehri, and T. Lazaridis, "Mechanism of negative membrane curvature generation by I-BAR domains", *Structure*, 2021. DOI: 10.1016/j.str.2021.07.010.

[100] F. Quemeneur, J. K. Sigurdsson, M. Renner, P. J. Atzberger, P. Bassereau, and D. Lacoste, "Shape matters in protein mobility within membranes", *Proceedings of the National Academy of Sciences*, 2014. DOI: 10.1073/pnas.1321054111.

[101] S. Chakraborty, M. Doktorova, T. R. Molugu, *et al.*, "How cholesterol stiffens unsaturated lipid membranes", *Proceedings of the National Academy of Sciences*, 2020. DOI: 10.1073/pnas.2004807117.

[102] E. Evans and D. Needham, "Physical properties of surfactant bilayer membranes: Thermal transitions, elasticity, rigidity, cohesion and colloidal interactions", *The Journal of Physical Chemistry*, 1987. DOI: 10.1021/j100300a003.

[103] A. Hossein and M. Deserno, "Stiffening transition in asymmetric lipid bilayers: The role of highly ordered domains and the effect of temperature and size", *The Journal of Chemical Physics*, 2021. DOI: 10.1063/5.0028255.

[104] G. W. Feigenson, "Phase diagrams and lipid domains in multicomponent lipid bilayer mixtures", *Biochimica et Biophysica Acta (BBA) - Biomembranes*, 2009. DOI: 10.1016/j.bbamem.2008.08.014.

[105] H. De Belly, S. Yan, H. Borja Da Rocha, *et al.*, "Cell protrusions and contractions generate long-range membrane tension propagation", *Cell*, 2023. DOI: 10.1016/j.cell.2023.05.014.

[106] C. Mim and V. M. Unger, "Membrane curvature and its generation by BAR proteins", *Trends in Biochemical Sciences*, 2012. DOI: 10.1016/j.tibs.2012.09.001.

[107] Z. Shi and T. Baumgart, "Membrane tension and peripheral protein density mediate membrane shape transitions", *Nature Communications*, 2015. DOI: 10.1038/ncomms6974.

[108] C. van der Wel, D. Heinrich, and D. J. Kraft, "Microparticle assembly pathways on lipid membranes", *Biophysical Journal*, 2017. DOI: 10.1016/j.bpj.2017.07.019.

[109] S. Tzlil, M. Deserno, W. M. Gelbart, and A. Ben-Shaul, "A statistical-thermodynamic model of viral budding", *Biophysical Journal*, 2004. DOI: 10.1016/S0006-3495(04)74265-4.

[110] R. Golestanian, M. Goulian, and M. Kardar, "Fluctuation-induced interactions between rods on membranes and interfaces", *Europhysics Letters*, 1996. DOI: 10.1209/epl/i1996-00327-4.

[111] N. Dan, A. Berman, P. Pincus, and S. A. Safran, "Membrane-induced interactions between inclusions", *Journal de Physique II*, 1994. DOI: 10.1051/jp2:1994227.

[112] R. Regmi, T. Gressier, B. Chauvin, A. Damm, J. Manzi, M. Dezi, D. Levy, and P. M. Bassereau, "Conformation-dependent diffusion properties of a transmembrane protein", *Biophysical Journal*, 2023. DOI: 10.1016/j.bpj.2022.11.1029.

[113] H. Noguchi, C. Tozzi, and M. Arroyo, "Binding of anisotropic curvature-inducing proteins onto membrane tubes", *Soft Matter*, 2022. DOI: 10.1039/D2SM00274D.

[114] G. Fusco, S. W. Chen, P. T. F. Williamson, *et al.*, "Structural basis of membrane disruption and cellular toxicity by -synuclein oligomers", *Science*, 2017. DOI: 10.1126/science.aan6160.

[115] M. G. Erkkinen, M.-O. Kim, and M. D. Geschwind, "Clinical neurology and epidemiology of the major neurodegenerative diseases", *Cold Spring Harbor Perspectives in Biology*, 2018. DOI: 10.1101/cshperspect.a033118.

[116] C. Reitz, C. Brayne, and R. Mayeux, "Epidemiology of alzheimer disease", *Nature Reviews Neurology*, 2011. DOI: 10.1038/nrneurol.2011.2.

[117] G. Meisl, "The thermodynamics of neurodegenerative disease", *Biophysics Reviews*, 2024. DOI: 10.1063/5.0180899.

[118] S. I. A. Cohen, M. Vendruscolo, C. M. Dobson, and T. P. J. Knowles, "Nucleated polymerization with secondary pathways. III. equilibrium behavior and oligomer populations", *The Journal of Chemical Physics*, 2011. DOI: 10.1063/1.3608918.

[119] G. Meisl, J. B. Kirkegaard, P. Arosio, T. C. T. Michaels, M. Vendruscolo, C. M. Dobson, S. Linse, and T. P. J. Knowles, "Molecular mechanisms of protein aggregation from global fitting of kinetic models", *Nature Protocols*, 2016. DOI: 10.1038/nprot.2016.010.

[120] H. Naiki, K. Higuchi, M. Hosokawa, and T. Takeda, "Fluorometric determination of amyloid fibrils in vitro using the fluorescent dye, thioflavine T", *Analytical Biochemistry*, 1989. DOI: 10.1016/0003-2697(89)90046-8.

[121] K. Gade Malmos, L. M. Blancas-Mejia, B. Weber, J. Buchner, M. Ramirez-Alvarado, H. Naiki, and D. Otzen, "ThT 101: A primer on the use of thioflavin T to investigate amyloid formation", *Amyloid*, 2017. DOI: 10.1080/13506129.2017.1304905.

[122] S. I. A. Cohen, S. Linse, L. M. Luheshi, *et al.*, "Proliferation of amyloid-42 aggregates occurs through a secondary nucleation mechanism", *Proceedings of the National Academy of Sciences*, 2013. DOI: 10.1073/pnas.1218402110.

[123] L. V. C. Miller, A. S. Mukadam, C. S. Durrant, *et al.*, "Tau assemblies do not behave like independently acting prion-like particles in mouse neural tissue", *Acta Neuropathologica Communications*, 2021. DOI: 10.1186/s40478-021-01141-6.

[124] B. J. Tuck, L. V. Miller, T. Katsinelos, *et al.*, "Cholesterol determines the cytosolic entry and seeded aggregation of tau", *Cell Reports*, 2022. DOI: 10.1016/j.celrep.2022.110776.

[125] M. Jucker and L. C. Walker, "Propagation and spread of pathogenic protein assemblies in neurodegenerative diseases", *Nature Neuroscience*, 2018. DOI: 10.1038/s41593-018-0238-6.

[126] B. B. Holmes, J. L. Furman, T. E. Mahan, *et al.*, "Proteopathic tau seeding predicts tauopathy in vivo", *Proceedings of the National Academy of Sciences*, 2014. DOI: 10.1073/pnas.1411649111.

[127] C. H. Van Dyck, C. J. Swanson, P. Aisen, *et al.*, "Lecanemab in early Alzheimer's disease", *New England Journal of Medicine*, 2023. DOI: 10.1056/NEJMoa2212948.

[128] J. R. Sims, J. A. Zimmer, C. D. Evans, *et al.*, "Donanemab in early symptomatic Alzheimer disease: The TRAILBLAZER-ALZ 2 randomized clinical trial", *JAMA*, 2023. DOI: 10.1001/jama.2023.13239.

[129] M. Vaz, V. Silva, C. Monteiro, and S. Silvestre, "Role of aducanumab in the treatment of Alzheimer's disease: Challenges and opportunities", *Clinical Interventions in Aging*, 2022. DOI: 10.2147/CIA.S325026.

[130] T. Wisniewski and F. Goñi, "Immunotherapeutic approaches for Alzheimer's disease", *Neuron*, 2015. DOI: 10.1016/j.neuron.2014.12.064.

[131] C. Rinaldi and M. J. A. Wood, "Antisense oligonucleotides: The next frontier for treatment of neurological disorders", *Nature Reviews Neurology*, 2018. DOI: 10.1038/nrneurol.2017.148.

[132] T. A. Cole, H. Zhao, T. J. Collier, *et al.*, "α-synuclein antisense oligonucleotides as a disease-modifying therapy for Parkinson's disease", *JCI Insight*, 2021. DOI: 10.1172/jci.insight.135633.

[133] S. L. DeVos, R. L. Miller, K. M. Schoch, *et al.*, "Tau reduction prevents neuronal loss and reverses pathological tau deposition and seeding in mice with tauopathy", *Science Translational Medicine*, 2017. DOI: 10.1126/scitranslmed.aag0481.

[134] C. J. Mummery, A. Börjesson-Hanson, D. J. Blackburn, *et al.*, "Tau-targeting antisense oligonucleotide MAPTRx in mild Alzheimer's disease: A phase 1b, randomized, placebo-controlled trial", *Nature Medicine*, 2023. DOI: 10.1038/s41591-023-02326-3.

[135] E. N. Neumann, T. M. Bertozzi, E. Wu, *et al.*, "Brainwide silencing of prion protein by AAV-mediated delivery of an engineered compact epigenetic editor", *Science*, 2024. DOI: 10.1126/science.ado7082.

[136] G. Meisl, T. P. J. Knowles, and D. Klenerman, "Mechanistic models of protein aggregation across length-scales and time-scales: From the test tube to neurodegenerative disease", *Frontiers in Neuroscience*, 2022. DOI: 10.3389/fnins.2022.909861.

[137] Y. Hou, X. Dan, M. Babbar, Y. Wei, S. G. Hasselbalch, D. L. Croteau, and V. A. Bohr, "Ageing as a risk factor for neurodegenerative disease", *Nature Reviews Neurology*, 2019. DOI: 10.1038/s41582-019-0244-7.

[138] G. Meisl, E. Hidari, K. Allinson, *et al.*, "In vivo rate-determining steps of tau seed accumulation in Alzheimer's disease", *Science Advances*, 2021. DOI: 10.1126/sciadv.abh1448.

[139] S. K. Van Den Eeden, "Incidence of Parkinson's disease: Variation by age, gender, and race/ethnicity", *American Journal of Epidemiology*, >11 2003. DOI: 10.1093/aje/kwg068.

[140] W. Poewe, K. Seppi, C. M. Tanner, G. M. Halliday, P. Brundin, J. Volkmann, A.-E. Schrag, and A. E. Lang, "Parkinson disease", *Nature Reviews Disease Primers*, 2017. DOI: 10.1038/nrdp.2017.13.

[141] T. B. Thompson, G. Meisl, T. P. J. Knowles, and A. Goriely, "The role of clearance mechanisms in the kinetics of pathological protein aggregation involved in neurodegenerative diseases", *The Journal of Chemical Physics*, 2021. DOI: 10.1063/5.0031650.

[142] A. Ciechanover and Y. T. Kwon, "Degradation of misfolded proteins in neurodegenerative diseases: Therapeutic targets and strategies", *Experimental & Molecular Medicine*, 2015. DOI: 10.1038/emm.2014.117.

[143] J. M. Barral, S. A. Broadley, G. Schaffar, and F. Hartl, "Roles of molecular chaperones in protein misfolding diseases", *Seminars in Cell & Developmental Biology*, 2004. DOI: 10.1016/j.semcdb.2003.12.010.

[144] S. I. A. Cohen, M. Vendruscolo, C. M. Dobson, and T. P. J. Knowles, "Nucleated polymerization with secondary pathways. II. determination of self-consistent solutions to growth processes described by non-linear master equations", *The Journal of Chemical Physics*, 2011. DOI: 10.1063/1.3608917.

[145] M. Iba, J. L. Guo, J. D. McBride, B. Zhang, J. Q. Trojanowski, and V. M.-Y. Lee, "Synthetic tau fibrils mediate transmission of neurofibrillary tangles in a transgenic mouse model of Alzheimer's-like tauopathy", *The Journal of Neuroscience*, 2013. DOI: 10.1523/JNEUROSCI.2642-12.2013.

[146] H. Braak, K. D. Tredici, U. Rüb, R. A. De Vos, E. N. Jansen Steur, and E. Braak, "Staging of brain pathology related to sporadic Parkinson's disease", *Neurobiology of Aging*, 2003. DOI: 10.1016/S0197-4580(02)00065-9.

[147] P. Putra, T. B. Thompson, P. Chaggar, and A. Goriely, "Braiding braak and braak: Staging patterns and model selection in network neurodegeneration", *Network Neuroscience*, 2021. DOI: 10.1162/netn_a_00208.

[148] G. S. Brennan, T. B. Thompson, H. Oliveri, M. E. Rognes, and A. Goriely, "The role of clearance in neurodegenerative diseases", *SIAM Journal on Applied Mathematics*, 2023. DOI: 10.1137/22M1487801.

[149] J. Agudo-Canalejo, P. Illien, and R. Golestanian, "Cooperatively enhanced reactivity and "stabilitaxis" of dissociating oligomeric proteins", *Proceedings of the National Academy of Sciences*, 2020. DOI: 10.1073/pnas.1919635117.

[150] J. Keller, F. Huang, and W. Markesbery, "Decreased levels of proteasome activity and proteasome expression in aging spinal cord", *Neuroscience*, 2000. DOI: 10.1016/S0306-4522(00)00067-1.

[151] J. H. Park, Y. J. Bae, J. S. Kim, *et al.*, "Glymphatic system evaluation using diffusion tensor imaging in patients with traumatic brain injury", *Neuroradiology*, 2023. DOI: 10.1007/s00234-022-03073-x.

[152] P. W. Schofield, M. Tang, K. Marder, *et al.*, "Alzheimer's disease after remote head injury: An incidence study.", *Journal of Neurology, Neurosurgery & Psychiatry*, 1997. DOI: 10.1136/jnnp.62.2.119.

[153] A. B. Graves, E. White, T. D. Koepsell, B. V. Reifler, G. Van Belle, E. B. Larson, and M. Raskind, "The association between head trauma and Alzheimer's disease", *American Journal of Epidemiology*, 1990. DOI: 10.1093/oxfordjournals.aje.a115523.

[154] V. E. Johnson, W. Stewart, and D. H. Smith, "Traumatic brain injury and amyloid-β pathology: A link to Alzheimer's disease?", *Nature Reviews Neuroscience*, 2010. DOI: 10.1038/nrn2808.

[155] E. R. Russell, D. F. Mackay, D. Lyall, K. Stewart, J. A. MacLean, J. Robson, J. P. Pell, and W. Stewart, "Neurodegenerative disease risk among former international rugby union players", *Journal of Neurology, Neurosurgery & Psychiatry*, 2022. DOI: 10.1136/jnnp-2022-329675.

[156] C. Bellenguez, B. Grenier-Boley, and J.-C. Lambert, "Genetics of Alzheimer's disease: Where we are, and where we are going", *Current Opinion in Neurobiology*, 2020. DOI: 10.1016/j.conb.2019.11.024.

[157] C. Bellenguez, F. Küçükali, I. E. Jansen, *et al.*, "New insights into the genetic etiology of Alzheimer's disease and related dementias", *Nature Genetics*, 2022. DOI: 10.1038/s41588-022-01024-z.

[158] E. Head, W. Silverman, D. Patterson, and I. T. Lott, "Aging and Down syndrome", *Current Gerontology and Geriatrics Research*, 2012. DOI: 10.1155/2012/412536.

[159] W. B. Zigman and I. T. Lott, "Alzheimer's disease in down syndrome: Neurobiology and risk", *Mental Retardation and Developmental Disabilities Research Reviews*, 2007. DOI: 10.1002/mrdd.20163.

[160] B. Rumble, R. Retallack, C. Hilbich, *et al.*, "Amyloid A4 protein and its precursor in Down's syndrome and Alzheimer's disease", *New England Journal of Medicine*, 1989. DOI: 10.1056/NEJM198906013202203.

[161] T. Khan, T. S. Kandola, J. Wu, *et al.*, "Quantifying nucleation in vivo reveals the physical basis of prion-like phase behavior", *Molecular Cell*, 2018. DOI: 10.1016/j.molcel.2018.06.016.

[162] J. Agudo-Canalejo, T. Adeleke-Larodo, P. Illien, and R. Golestanian, "Synchronization and enhanced catalysis of mechanically coupled enzymes", *Physical Review Letters*, 2021. DOI: 10.1103/PhysRevLett.127.208103.

[163] M. Chatzittofi, R. Golestanian, and J. Agudo-Canalejo, *Topological phase locking in molecular oscillators*, 2024. arXiv: 2310.11788[cond-mat,physics:nlin].

[164] F. Zosel, A. Soranno, K. J. Buholzer, D. Nettels, and B. Schuler, "Depletion interactions modulate the binding between disordered proteins in crowded environments", *Proceedings of the National Academy of Sciences*, 2020. DOI: 10.1073/pnas.1921617117.

[165] S. Asakura and F. Oosawa, "On interaction between two bodies immersed in a solution of macromolecules", *The Journal of Chemical Physics*, 1954. DOI: 10.1063/1.1740347.

[166] C. Galvagnion, A. K. Buell, G. Meisl, T. C. T. Michaels, M. Vendruscolo, T. P. J. Knowles, and C. M. Dobson, "Lipid vesicles trigger α-synuclein aggregation by stimulating primary nucleation", *Nature Chemical Biology*, 2015. DOI: 10.1038/nchembio.1750.

[167] A. J. Dear, X. Teng, S. R. Ball, *et al.*, "Molecular mechanism of α-synuclein aggregation on lipid membranes revealed", *Chemical Science*, 2024. DOI: 10.1039/D3SC05661A.

[168] S. L. Fowler, T. S. Behr, E. Turkes, *et al.*, *Tau filaments are tethered within brain extracellular vesicles in Alzheimer's disease*, preprint, 2023. DOI: 10.1101/2023.04.30.537820.

[169] A. Molliex, J. Temirov, J. Lee, M. Coughlin, A. P. Kanagaraj, H. J. Kim, T. Mittag, and J. P. Taylor, "Phase separation by low complexity domains promotes stress granule assembly and drives pathological fibrillization", *Cell*, 2015. DOI: 10.1016/j.cell.2015.09.015.

[170] Y. Soeda, H. Yoshimura, H. Bannai, R. Koike, I. Shiiba, and A. Takashima, "Intracellular tau fragment droplets serve as seeds for tau fibrils", *Structure*, 2024. DOI: 10.1016/j.str.2024.06.018.

[171] W. Pönisch, T. C. T. Michaels, and C. A. Weber, "Aggregation controlled by condensate rheology", *Biophysical Journal*, 2023. DOI: 10.1016/j.bpj.2022.11.009.

[172] C. Weber, T. Michaels, and L. Mahadevan, "Spatial control of irreversible protein aggregation", *eLife*, 2019. DOI: 10.7554/eLife.42315.

[173] G. Bartolucci, T. C. Michaels, and C. A. Weber, "The interplay between molecular assembly and phase separation", preprint, 2023. DOI: 10.1101/2023.04.18.537072.

[174] A. Mangiarotti, N. Chen, Z. Zhao, R. Lipowsky, and R. Dimova, "Wetting and complex remodeling of membranes by biomolecular condensates", *Nature Communications*, 2023. DOI: 10.1038/s41467-023-37955-2.

[175] E. L. Elson, E. Fried, J. E. Dolbow, and G. M. Genin, "Phase separation in biological membranes: Integration of theory and experiment", *Annual Review of Biophysics*, 2010. DOI: 10.1146/annurev.biophys.093008.131238.

[176] A. Giudici and J. S. Biggins, "Ballooning, bulging, and necking: An exact solution for longitudinal phase separation in elastic systems near a critical point", *Physical Review E*, 2020. DOI: 10.1103/PhysRevE.102.033007.

[177] Q. Yu and A. Košmrlj, *Pattern formation of phase-separated lipid domains in bilayer membranes*, 2023. arXiv: 2309.05160[cond-mat,physics:physics].

[178] H. T. Phan, V. Passos Gibson, A. Guédin, *et al.*, "Switchable lipids: From conformational switch to macroscopic changes in lipid vesicles", *Langmuir*, 2023. DOI: 10.1021/acs.langmuir.2c03149.

[179] G. Villar, A. D. Graham, and H. Bayley, "A tissue-like printed material", *Science*, 2013. DOI: 10.1126/science.1229495.

[180] J. Kirschbaum and D. Zwicker, "Controlling biomolecular condensates via chemical reactions", *Journal of The Royal Society Interface*, 2021. DOI: 10.1098/rsif.2021.0255.

[181] V. Ouazan-Reboul, J. Agudo-Canalejo, and R. Golestanian, "Self-organization of primitive metabolic cycles due to non-reciprocal interactions", *Nature Communications*, 2023. DOI: 10.1038/s41467-023-40241-w.

[182] B. Wang, L. Zhang, T. Dai, Z. Qin, H. Lu, L. Zhang, and F. Zhou, "Liquid–liquid phase separation in human health and diseases", *Signal Transduction and Targeted Therapy*, 2021. DOI: 10.1038/s41392-021-00678-1.